Forschungszentrum Jülich
in der Helmholtz-Gemeinschaft

Institut für Festkörperforschung

Nanocrystalline Alkaline Earth Titanates and their Electrical Conductivity Characteristics under Changing Oxygen Ambients

Christian Andreas Ohly

Jül-4070

Nanocrystalline Alkaline Earth Titanates and their Electrical Conductivity Characteristics under Changing Oxygen Ambients

Christian Andreas Ohly

Berichte des Forschungszentrums Jülich ; 4070
ISSN 0944-2952
Institut für Festkörperforschung Jül-4070
D 82 (Diss., Aachen, RWTH, 2003)

Zu beziehen durch: Forschungszentrum Jülich GmbH · Zentralbibliothek
D-52425 Jülich · Bundesrepublik Deutschland
☎ 02461/61-5220 · Telefax: 02461/61-6103 · e-mail: zb-publikation@fz-juelich.de

Abstract

Electroceramic materials, especially the perovskite-type titanates, have been subject of intense research in recent years aiming for their integration into state-of-the-art electronic devices like memories or sensors. Due to continuous miniaturization, typical feature dimensions range down to several nanometers. Today, the discussion of thin film electrical behavior (like leakage currents or degradation effects) is still based on the established model of bulk defect chemistry. However, the observed electrical properties of thin films are often inconsistent with this model.

Against the background of single crystals, the present work represents the first systematic study of the conductivity characteristics of alkaline earth titanates in the form of polycrystalline and heteroepitaxial thin films as well as nanocrystalline ceramics as a function of temperature and the ambient oxygen partial pressure. This was made possible by using a specially designed measurement setup that allowed the reliable determination of resistances of up to several gigaohms at temperatures between 600 °C and 1000 °C under continuously adjustable oxygen partial pressures ranging from 10^{-20} bar to 1 bar.

In contrast to the well-known 'v-shaped' $\log \sigma$ - $\log pO_2$ profile of single crystals, due to n-type and p-type conduction, the conductivity behavior of CSD-prepared, polycrystalline $SrTiO_3$ thin films with a grain size of ~ 50 nm differs radically. Besides markedly shifted absolute values, the most prominent characteristics are a sharp drop under reducing conditions followed by a broad plateau region. Furthermore, the p-type regime does not appear under oxidizing conditions.

Tailored investigations on heteroepitaxial as well as polycrystalline thin films grown by PLD and especially by studies on nanocrystalline $BaTiO_3$-ceramics with a mean grain size of ≤ 100 nm allowed an unambiguous assignment of these effects to morphological properties. Besides the surface-to-volume ratio in particular the high grain boundary density is a decisive measure for the different conductivity profiles of nanocrystalline titanates.

This work shows for the first time that nanocrystalline titanates reveal special conductivity characteristics which cannot be explained by the classical model alone. Additionally, important aspects for a model description were developed taking into account the strongly inhomogeneous habit of nanocrystalline materials.

Kurzfassung

Elektrokeramische Werkstoffe sind aufgrund ihrer vielfältigen Einsatzmöglichkeiten Gegenstand intensiver Forschungsaktivitäten. Insbesondere Titanate mit Perowskitstruktur werden verstärkt in Form dünner Schichten in modernste elektronische Bauelemente wie Speicher oder Sensoren integriert. Als Folge stetiger Miniaturisierung reichen die Strukturgrößen hinab bis zu einigen Nanometern. Zur Erklärung des elektrischen Verhaltens von Dünnschichten (wie Leckströme oder Degradationseffekte) wird heute immer noch das etablierte Modell der Bulk-Defektchemie herangezogen. Die beobachteten Eigenschaften sind mit diesem Modell jedoch oft inkonsistent.

Vor dem Hintergrund des Einkristalls gibt diese Arbeit erstmals eine systematische Studie des Leitfähigkeitsverhalten von Erdalkalititanaten sowohl in Form polykristalliner und heteroepitaktischer Dünnschichten als auch nanokristalliner Keramiken in Abhängigkeit von der Temperatur und des Sauerstoffpartialdruckes. Dafür wurde ein spezieller Hochtemperatur-Leitfähigkeits-Messplatz entwickelt, der die verlässliche Bestimmung der Widerstandswerte von Dünnschichten im Giga-Ohm-Bereich bei Temperaturen zwischen 600°C und 1000°C und einem von 10^{-20} bar bis 1 bar kontrolliert einstellbaren Sauerstoffatmosphäre ermöglicht.

Gegenüber dem bekannten, aufgrund von n- sowie p-Leitung 'v-artigen' $\log \sigma$ - $\log pO_2$-Profil von Einkristallen unterscheidet sich das Leitfähigkeitsverhalten polykristalliner $SrTiO_3$-Dünnschichten (CSD) mit einer Korngröße von ~ 50 nm drastisch. Neben deutlich verschobenen Absolutwerten sind die wesentlichen Charakteristiken ein Sprung unter reduzierenden Bedingungen, gefolgt von einem breiten Plateaubereich. Der Bereich der p-Leitung tritt nicht auf.

Gezielte Untersuchungen an heteroepitaktischen sowie polykristallinen PLD-Schichten und insbesondere an nanokristallinen $BaTiO_3$-Keramiken mit einer mittleren Korngröße ≤ 100 nm erlaubten eine eindeutige Zuordnung dieser Effekte zu morphologischen Eigenschaften. Neben dem Verhältnis von Oberfläche zum Volumen ist vornehmlich die hohe Korngrenzdichte ein entscheidendes Maß für die veränderten Leitfähigkeitsprofile nanokristalliner Titanate.

Diese Arbeit zeigt erstmals, dass nanokristalline Titanate eine spezielle Leitfähigkeitscharakteristik aufweisen, für deren Interpretation das klassische Modell alleine nicht ausreicht. Weiterhin werden wichtige Aspekte für eine modellhafte Beschreibung herausgearbeitet, die dem stark inhomogenen Charakter der nanokristallinen Materialien Rechnung trägt.

Contents

1 Introduction

1.1 Motivation

Electroceramic oxides of the perovskite type and related structures exhibit a lot of very interesting properties for electronic devices as well as for novel applications and have gained great attention in worldwide research activities in recent years [1]-[3]. Their outstanding spectrum encompasses electrical, dielectric, ferroelectric, piezoelectric, pyroelectric, electrooptical and magnetooptical properties and every one of them can be changed with regard to the intended application over a wide range by compositional, stoichiometric, structural or morphological variation. As an example, the electrical conduction behavior ranges from superconducting through metallic and semiconducting to highly insulating [4]-[6].

In the fast growing field of information storage and processing, state-of-the-art integrated devices combine the classical semiconductors with electroceramic materials in order to further increase the degree of miniaturization. Here, current research comprises the integration of high-κ thin films in dynamic random access memories (DRAMs) [7]-[9] or the replacement of silicon oxide as the gate dielectric in field effect transistors (FETs) [10]-[12]. Further investigations draw their attention to the development and integration of ferroelectric thin films into new functional devices like non-volatile memories (FeRAMs) [13]-[15] or ferroelectric field effect transistors (FeFETs) [16].

Titanate-based thin films are also used for applications in mobile communications like decoupling capacitors in monolithic microwave integrated circuits (MMICs) [17] or tunable devices [18], for optical switches, and they can be found in microelectromechanical devices (MEMs) [19].

Sensor applications are another profitable area of the utilization of perovskite thick and thin films. As an important example, the correlation between electrical conductivity and the oxygen stoichiometry of the material is exploited to fabricate selective gas sensors [19]-[21].

Among the most promising and widely investigated material systems are the titanate-based solid solution series $Ba_{1-x}Sr_xTiO_3$ as a high-κ dielectric and $PbZr_{1-y}Ti_yO_3$ as a ferroelectric material.

As a consequence of the ongoing reduction of feature sizes, the dimensions of the integrated thin films have decreased to several ten nanometers on the lateral scale and down to a few nanometers in thickness. Also, the particle sizes of ultrafine titanate powders as base materials for LTCC components are now entering the region of 10 nm and less, offering the possibility of synthesizing nanocrystalline ceramics of similar proportions [22].

1.2 State of the Art

With respect to functional requirements and integration issues, a lot of versatile methods have been developed in the last two decades into sophisticated techniques for the deposition of titanate thin films [23]. Chemical processes like chemical solution deposition (CSD) [24] or metal organic chemical vapor deposition (MOCVD) [25][26] make use of metal organic precursors, either dissolved in proper organic liquids or provided in the solid or gaseous state. The MOCVD process is the state-of-the-art technique for homogeneous and conformal deposition of primarily perovskite oxide electroceramic thin films on 3-dimensional structures [27]. A second class of well-established techniques are physical processes, where the major examples are sputtering [28] and pulsed laser deposition (PLD) [29]. These methods, which need elementary or oxide targets of the desired stoichiometry, are primarily used to grow epitaxial films of complex systems, like high-temperature superconductors (HTSCs) or Aurivillius type structures [30]. As a third method, molecular beam epitaxy (MBE) is used mainly for fundamental research on ultrathin films or specially designed layered structures [31][32]. Typical crystallization temperatures of chemical deposition processes range roughly between 500 – 600 °C for $PbZr_{1-y}Ti_yO_3$ (PZT) composites and 600 – 800 °C for the alkaline earth titanates like the solid solution series $Ba_{1-x}Sr_xTiO_3$ (BST). For the growth of epitaxial BST thin films sometimes temperatures of about 1000 °C are reached. The oxygen partial pressures during deposition or subsequent annealing steps vary from extremely low values of about 10^{-10} bar for MBE through 10^{-6} bar to some 10^{-3} bar for PLD or MOCVD processes up to a pure oxygen atmosphere of 1 bar for CSD procedures.

For the description of the electrical properties that change as a function of the oxygen partial pressure during sintering, the defect chemistry of single crystal and bulk ceramic titanates has been extensively studied since the late 1960s [33]-[41]. To describe the electrical conductivity

characteristics and their relation to parameters like temperature, oxygen atmosphere or dopant incorporation by acceptor- or donor-type elements, the model of point defect chemistry has been formulated (e.g. [39]-[41]). The interaction of the parameters can be explained successfully on the basis of defect chemical reactions, exchange processes with the atmosphere and changes of the valence state regarding their individual thermal activation and the thermodynamical equilibrium.

Recent investigations focusing on the highly resistive grain boundaries have extended the understanding of titanate ceramics. Their drastically different electrical characteristics are responsible for several effects like the positive temperature coefficient (PTC) effect [42]. The theoretical description attributes the highly insulating barrier character to immobile interface states at the grain boundaries, which lead to compensating space charge layers, whose electrical influence is usually of the order of 30 to 200 nm. Theoretically as well as experimentally investigated systems have mostly been singular interfaces of bicrystals or coarse-grained ceramics, with dimensions much larger than the space charge layer width [43]-[48].

For integrated titanate thin films the numerous combinations of materials and the very different processing conditions, compared to conventional bulk ceramic processing, are reflected in a variety of structural and morphological habits extending from single crystalline through columnar with a more or less prominent texture and fine-grained to polycrystalline. The correlation between the morphology and structure of thin films and their electrical properties is of central importance. However, the physical description of the films, which is necessary for a precise tailoring of device characteristics, is still difficult because properties are often drastically different with decreasing dimensions.

Today, the discussion of thin film electrical behavior (like leakage currents or degradation effects) is still based on bulk defect chemistry, because no systematic and comprehensive study on the defect chemistry of nanocrystalline titanates, where grain sizes or feature sizes are of the same order as the electrical extension of the grain boundary or even below, has been reported yet.

1.3 Objectives

The aim of this work is to obtain for the first time a comprehensive insight into the defect chemical behavior of titanate-based thin films and nanocrystalline ceramics. This is addressed by means of systematic and detailed investigations on the high temperature conductivity

characteristics under changing oxygen atmospheres. On the one hand, the studies comprise a widespread range of stoichiometric modification by iso- or heterovalent cation substitution. On the other side, morphological variations, i.e. a distinct alteration of the grain boundary density, are the essential aspect of this work. The investigations focus primarily on $SrTiO_3$-based thin films. This material is often used as a model perovskite system thus permitting a thorough comparison with the bulk characteristics.

In detail, the individual tasks are as follows:

- An indispensable prerequisite is a well-designed measuring setup. This includes precise and continuous control of the oxygen partial pressure as well as a reliable measuring technique to avoid disturbing influences.

- Against the background of distinct differences between bulk materials and thin films regarding electrical properties, the first task will be to examine the high-temperature conductivity behavior of an undoped $SrTiO_3$ thin film with a high interface density to reveal general differences compared to the well-known behavior of single crystals and bulk ceramics (see Figure 1.1).

- The important influence of doping, i.e. the heterovalent cation substitution, on the electrical properties of titanate thin films will be studied by incorporating acceptor-type dopants like manganese or iron and donor-type elements like lanthanum.

- Another aim is to investigate the extent to which an isovalent cation substitution affects the conductivity behavior. For this purpose, in particular the solid solution series $Ba_{1-x}Sr_xTiO_3$ and $BaTi_{1-y}Zr_yO_3$ will be examined for selected stoichiometries.

- One of the key questions of this work addresses the interplay between the micro-/nanostructure of the films and the conduction characteristics. To establish a clear correlation, thin films with different morphological and structural habits from single crystalline with different film thicknesses to polycrystalline with varying interface densities will be prepared and investigated.

- To link thin films with bulk materials and to exclude any substrate influence, ceramic samples with a comparable grain size will also be investigated. Due to the fact that common preparation techniques do not permit such fine-grained ceramics to be made, a new method has to be established.

Figure 1.1

Different morphologies of titanates.

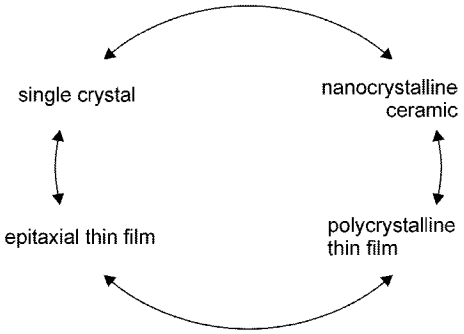

- Based on existing results and considering the fact that thin films often exhibit an unprecedentedly high density of grain boundaries, the question will be answered of the extent to which the existing model of point defect chemistry is still applicable.

- On the other hand, the possibility of alternative approaches to a description of charge transport in titanate thin films will be investigated.

References

[1] R. Waser, ed., "Nanoelectronics and Information Technology", ISBN 3-52740-363-9, Wiley-VCH, Weinheim, 2003.

[2] N. Setter, "Electroceramics: looking ahead", *J. Eur. Ceram. Soc.* **21**, 1279 (2001).

[3] H.L. Tuller, J. Schoonman and I. Riess, eds., "Oxygen Ion and Mixed Conductors and their Technological Applications", Proceedings of NATO Adv. Study Inst., Erice, Italy, 1997. Kluwer Academic Publishers, Dordrecht, The Netherlands, 2000.

[4] H. Schaumburg, *Keramik*, Vol. 5, Werkstoffe und Bauelemente der Elektrotrechnik, Teubner Verlag, Stuttgart 1994.

[5] A.J. Moulsen and J. Herbert, *Electroceramics*, John Wiley and Sons, Hoboken, 2003.

[6] Lecture *Elektrokeramische Materialien*, 26. IFF-Ferienkurs, ISBN 3-89336-146-4, Forschungszentrum Jülich, 1995.

[7] M. Yoshida, H. Yabuta, S. Yamagouchi, H. Yamaguchi, K. Sone, T. Arita, T. Iizuka, S. Nichimoto and Y. Kato, "Plasma CVD of (Ba,Sr)TiO_3 dielectrics for Gigabit DRAM capacitors", *J. Electroceramics* **3**, 123 (1999).

[8] B.M. Melnick, "Development Challenges of Gigabit Scale 1T-1C DRAMs", 11th International Symposium on Integrated Ferroelectrics, Colorado Springs, 1999.

[9] D.E. Kotecki, J.D. Baniecki, H. Shen, R.B. Laibowitz, K.L. Saenger, J.J. Lian, T.M. Shaw, S.D. Athavale, C. Cabral Jr., P.R. Duncombe, M. Gutsche, G. Kunkel, Y.-J. Park, Y.-Y. Wang and R. Wise, "(Ba,Sr)TiO_3 Dielectrics for Future Stacked Capacitor DRAMs", *IBM J. Res. Develop.* **43-3**, 367 (1999).

[10] A. I. Kingon, J.-P. Maria and S. K. Streiffer, "Alternative dielectrics to silicon dioxide for memory and logic devices", *Nature* **406**, 1032 (2000).

[11] C.A. Billman, P.H. Tan, K.J. Hubbard, and D.G. Schlom, "Alternate Gate Oxides for Silicon MOSFETs using High-K Dielectrics" in: *Ultrathin SiO_2 and High-K Materials for ULSI Gate Dielectrics*, edited by H.R. Huff, C.A. Richter, M.L. Green, G. Lucovsky, and T. Hattori, **567**, 409 Materials Research Society, Warrendale, 1999.

[12] R.A. McKee, F.J. Walker and M.F. Chisholm, "Crystalline Oxides on Silicon: The First Five Monolayers" *Phys. Rev. Lett.* **81**, 3014 (1998).

[13] J. Scott and C.P. de Araujo, "Ferroelectric Memories", *Science* **246**, 1400 (1989).

[14] P. Zurcher, R. Jones, P. Chu, D. Taylor, B. White, S. Zafar, J. Bo, T.L. Yeong-Jyh and S. Gillespie, "Ferroelectric Nonvolatile Memory Technology: Application and Integration Challenges", *IEEE Transactions on Components Packaging, and Manufacturing Technology* **A 20**, 175 (1997).

[15] S. Summerfelt, "Ferroelectric Nonvolatile Memories", 12th International Symposium on the Applications of Ferroelectrics, Hawaii, 2000.

[16] H Ishiwara, "Current Status of Fabrication and Integration of Feroelectric-Gate FET's", *Mat. Res. Soc. Symp. Proc.* **596**, 427 (2000).

[17] A. Noma and D. Ueda, "Reliability study on BST Capacitors for GaAs MMIC", *Integr. Ferroelectr.* **15**, 69 (1997).

[18] B. Acikel, T.R. Taylor, P.J. Hansen, J.S. Speck and R.A. York, "A new high performance phase shifter using $Ba_xSr_{1-x}TiO_3$ thin films", *IEEE Microwave and Wireless Components Letters* **12**, 237 (2002).

[19] H.L. Tuller and R. Mlcak, "Advanced Sensor Technology Based on Oxides Thin Films – MEMS Integration", *J. Electroceramics* **4**, 415 (2000).

[20] J. Gerblinger and H. Meixner, "$SrTiO_3$ Thin Films for Oxygen Sensors", in: NATO ASI Series E, Applied Sciences **284**, 439. O. Auciello and R. Waser, eds., Kluwer Academic Publishers, Dordrecht, 1995.

[21] W. Menesklou, H.-J. Schreiner, K.H. Härdtl and E. Ivers-Tiffée, "High Temperature Oxygen Sensors Based on Doped $SrTiO_3$", *Sensors and Actuators B* **59**, 184 (1999).

[22] Ch. Beck, W. Härtl and R. Hempelmann, "Size-controlled synthesis of nanocrystalline $BaTiO_3$ by a sol-gel type hydrolysis in microemulsion-provided nanoreactors", *J. Mat. Res.* **13**, 3174 (1998).

[23] O. Auciello, R. Ramesh and Guest Editors, "Electroceramic Thin Films, Part I: Processing", *Mat. Res. Soc. Bull.* **21**, No. 6 (1996).

[24] S. Hoffmann, "Modifizierte Erdalkalititanat-Dünnschichten für integrierte Bauelemente: Morphologie, dielektrische Eigenschaften und Ladungstransportmechanismen", PhD thesis, RWTH Aachen, Fortschrittberichte VDI, Reihe 9, Nr. 288, Düsseldorf, 1998.

[25] H. Funakubo, Y. Takeshima, D. Nagano, K. Shinozaki and N. Mizutani, "Crystal Structure and Dielectric Property of Epitaxially Grown $(Ba,Sr)TiO_3$ Thin Film Prepared by MOCVD", *J. Mat. Res.* **13**, 3512 (1998).

[26] M. Aratani, K. Nagashimja and H. Funakubo, "Preparation of $Pb(Zr_xTi_{1-x})O_3$ Film by Source Gas Pulse-Induced MOCVD", *Jpn. J. Appl. Phys.* **40** (6A), 4126 (2001).

[27] C.S. Hwang, J. Park, D.S. Hwang and C.Y. Yoo, "Compositional Variation of Metallorganic Chemically Vapor Deposited $SrTiO_3$ Thin Films along the Capacitor Hole Having a Diameter of 0.15 μm", *J. Electrochem. Soc.* **148**, G636 (2001).

[28] Y. Imanaka, T. Shioga and J.D. Baniecki, "Decoupling capacitor with low inductance for high-frequency digital applications", *Fujitsu Scientific and Technical Journal* **38**, 22 (2002).

[29] D.B. Chrisey and G.K. Hubler, editors, *Pulsed Laser Deposition of Thin Films*, Wiley, New York, 1994.

[30] A. Pignolet, K.M. Satyalakshmi, M. Alexe, N. Zakharova, C. Harnagea, S. Senz. D. Hesse and U. Gösele, "Epitaxial bismuth-layer-structured perovskite ferroelectric thin films grown by pulsed laser deposition", *Integr. Ferroelectr.* **26**, 21 (1999).

[31] D.G. Schlom, C.D. Theis and M.E. Hawley, "The Controlled Growth of Perovskite Thin Films: Opportunities, Challenges, and Synthesis" in: *Integrated Thin Films and Applications*, edited by R.K. Pandey, D.E. Witter, and U. Varshney, **86**, 41, American Ceramic Society, Westerville, 1998.

[32] J.H. Haeni, C.D. Theis, D.G. Schlom, W. Tian, X.Q. Pan, H. Chang, I. Takeuchi and X.-D. Xiang, "Epitaxial growth of the first five members of the $Sr_{n+1}Ti_nO_{3n+1}$ Ruddlesden-Popper homologous series", *Appl. Phys. Lett.* **78**, 3292 (2001).

[33] L.C. Walters and R.E. Grace, "Formation of Point Defects in Strontium Titanate", *J. Phys. Chem. Solids* **28**, 239 (1967).

[34] S.A. Long and R.N. Blumenthal, "Ti-rich Nonstoichiometric $BaTiO_3$: I, High-Temperature Electrical Conductivity Measurements", *J. Am. Ceram. Soc.* **54**, 515 (1971).

[35] N.G. Eror and U. Balachandran, "High-Temperature Defect Structure of Acceptor-Doped Strontium Titanate", *J. Am. Ceram. Soc.* **65**, 426 (1982).

[36] N.H. Chan, R.K. Sharma and D.M. Smyth, "Nonstoichiometry in $SrTiO_3$", *J. Electrochem. Soc.* **128**, 1762 (1981).

[37] U. Balachandran and N.G. Eror, "Electrical Conductivity of Lanthanum-Doped Strontium Titanate", *J. Electrochem. Soc.* **129**, 1021 (1982).

[38] G.M. Choi, H.L. Tuller and D. Goldschmidt, "Electronic-transport behavior in single-crystalline $Ba_{0.03}Sr_{0.97}TiO_3$", *Phys. Rev. B* **34**, 6972 (1986).

[39] J. Maier, Festkörper - Fehler und Funktion - Prinzipien der Physikalischen Festkörperchemie, B.G. Teubner Verlag, Wiesbaden, 2000.

[40] R. Waser, D. M. Smyth, "Defect Chemistry, Conduction and Breakdown Mechanism of Perovskite-Structure Titanates", in: *Ferroelectric Thin Films: Synthesis and Basic Properties,* J.F. Scott, ed., Gordon & Breach, 1994.

[41] R. Moos, "Donatordotierung in Strontiumtitanat: Elektrische Eigenschaften und modellhafte Beschreibung", PhD thesis, Universität Karlsruhe, Fortschrittberichte VDI, Reihe 5, Nr. 362, Düsseldorf, 1994.

[42] W. Heywang, "Bariumtitanat als Sperrschichthalbleiter", *Solid State Electron.* **3**, 51 (1961).

[43] M. Vollmann, "Elektronische Korngrenzeigenschaften akzeptordotierter $SrTiO_3$-Dielektrika", PhD thesis, RWTH Aachen, Fortschrittberichte VDI, Reihe 9, Nr. 246, Düsseldorf, 1997.

[44] R. Hagenbeck, "Simulation der elektrischen Korngrenzeigenschaften akzeptordotierter $SrTiO_3$-Keramiken", PhD thesis, RWTH Aachen, Fortschrittberichte VDI, Reihe 9, Nr. 284, Düsseldorf, 1998.

[45] Y.-M. Chiang and T. Takagi, "Grain-Boundary Chemistry of Barium Titanate and Strontium Titanate: I, High-Temperature Equilibrium Space Charge", *J. Am. Ceram. Soc.* **73**, 3278 (1990).

[46] Y.-M. Chiang and T. Takagi, "Grain-Boundary Chemistry of Barium Titanate and Strontium Titanate: II, Origin of Electrical Barriers in Positive-Temperature-Coefficient Thermistors", *J. Am. Ceram. Soc.* **73**, 3286 (1990).

[47] Th. Hölbling, "A Simulation Model for Large-Signal dc Charge Transport Phenomena in p-type $SrTiO_3$", PhD thesis, RWTH Aachen, Shaker, Aachen, 2003.

[48] R.A. De Souza, O. Kienzle, J. Fleig, J. Maier and M. Rühle, "Electrical and Structural Characterization of a Low Angle Tilt Grain Boundary in Fe-doped $SrTiO_3$", in: *Ionic and Mixed Conducting Ceramics IV*, T.A. Ramanarayanan, W.L. Worrell, and M. Mogensen, eds., 226, Vol. **PV 2001-28**, The Electrochemical Society, Pennington, 2001.

2 Basics

In this chapter some basic characteristics of strontium titanate and related perovskite structures are described. $SrTiO_3$ is often referred to as a model material for the group of ABO_3-type titanates due to its simple cubic structure at room temperature. Single crystalline and bulk ceramic $SrTiO_3$ has been extensively investigated and therefore provides a good reference. Strontium titanate is especially suited for electrical investigations on intrinsic charge transport mechanisms because it is not ferroelectric and therefore does not show disturbing polarization effects.

2.1 Crystal Structure

'Perovskite' originally designated the mineral $CaTiO_3$ and today stands for a whole class of ternary oxides that exhibit the same or a related crystallographic structure. The cubic elementary cell, which is the simplest form of the perovskite structure and which $SrTiO_3$ takes at temperatures above 104 K, is pictured in Figure 2.1. The lattice constant of $SrTiO_3$ amounts to 3.905 Å at room temperature.

Figure 2.1

Cubic perovskite elementary cell of $SrTiO_3$. The ionic radii are not drawn to scale.

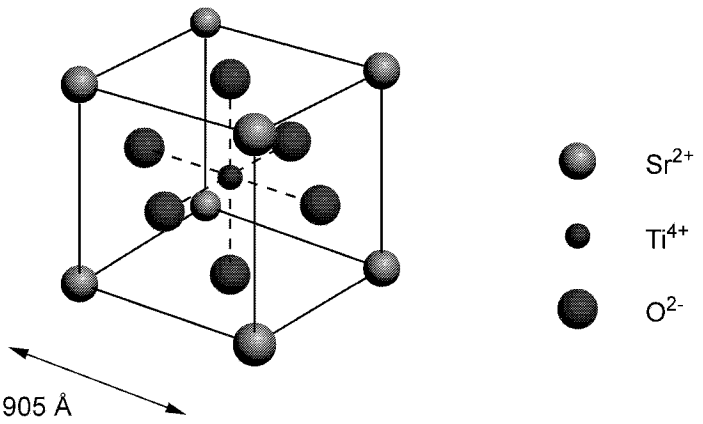

The general formula of the perovskite type oxides is ABO_3, where A and B represent metal cations that may have different valence states and different sizes. The larger A cations, like barium or strontium as considered in this work, form the edges of the cube and the smaller B cation, zirconium or especially titanium, is located in the center of it. The Ti-ion is surrounded by the octahedron of the oxygen anions and has therefore a 6-fold coordination while the strontium cation (or barium) shows a 12-fold coordination. Besides the mere ternary compounds, also the quaternary solid solutions, like $Ba_{1-x}Sr_xTiO_3$ and $BaTi_{1-y}Zr_yO_3$, form perovskite structures [1][2].

The stability of the structure and a possible distortion that modifies the cubic elementary cell into tetragonal, rhombohedral or orthorhombic structures, which are responsible for the manifold properties of the perovskite materials, depend on the individual ionic radii of the constituents. A measure is the tolerance factor t:

$$t = \frac{R_A + R_B}{\sqrt{2}\left(R_B + R_O\right)}, \tag{2.1}$$

where R_A, R_B and R_O denote the ionic radii of the constituents of the ABO_3 compound. The perovskite structure is stable for $0.7 \leq t \leq 1$, and it takes the cubic modification for $0.89 < t \leq 1$ and becomes distorted for $0.7 < t \leq 0.89$. (A concise treatment of these relationships can be found in [1][3][4].) Certainly, the modification is also a function of temperature. For $SrTiO_3$, three modifications are known: up to 65 K it is orthorhombic, then it becomes tetragonal and changes again at 104 K into the cubic structure [5]. This structure is maintained up to the melting point, which is at approximately 2000 °C [6][7]. The theoretical density of $SrTiO_3$ is 5.11 g/cm^3.

In Figure 2.1, the cation radii are not drawn to scale. The ionic radii of the basic matrix elements (Sr, Ba, Ti, Zr and O) and common doping elements for cation substitution are listed in Table 2.2. The alkaline earth titanates like $SrTiO_3$ and $BaTiO_3$ reveal a rather closed packaging of the lattice, what does not allow for interstitial site occupation (Frenkel disorder). Which lattice site is occupied by an impurity cation depends on its size and its valence state. Great differences of the diameters or impurity centers with high resulting defect charges are very unlikely to occur. For the possible dopants given in the table, the preferential site of occupation is quite clear.

Table 2.2

Ionic radii and valence states of the basic constituents and of various impurity elements that are commonly used as dopants. Values given here were taken from [8].

element (valence state)	lattice site	ionic radius [pm]	type of doping
Ba^{2+}	A	175	
Sr^{2+}	"	158	
La^{3+}	"	150	donor
Ti^{4+}	B	74.5	
Zr^{4+}	"	86	
Nb^{5+}	"	78	donor
Fe^{2+}	"	75	acceptor
Fe^{3+}	"	69	"
Mn^{2+}	"	81	"
Mn^{3+}	"	72	"
Mn^{4+}	"	67	"
O^{2-}	O	126	

The large trivalent lanthanum cation is a typical donor replacing barium or strontium [9], which are both divalent elements. On the other hand, iron and manganese, which are usually incorporated into the material as a trivalent compound (see Chapter 4), are frequently chosen as acceptor elements on the Ti site, as is also evident when looking at the similar radii of these cations. It should be kept in mind that these acceptor type impurities can change their valence state and thus act as traps for electron hole carriers (which will be discussed in more detail in the next chapter). For further information on the phase diagram of SrO - TiO_2, the reader is referred to [10]-[12].

2.2 Dielectric Properties

Titanates are high-κ materials and this property makes them so interesting for electronic applications. Above the phase transition temperature of 40 K, the dielectric behavior of $SrTiO_3$ is described by the empirical Curie-Weiss law:

$$\varepsilon_r(T) \approx \chi(T) = \frac{C}{T - \Theta}, \tag{2.2}$$

where the Curie constant C amounts to $7.83 \cdot 10^4$ K and the Curie temperature Θ is 28 K [16].

The dielectric properties are closely related to morphological and compositional variations. As an illustration, here the grain size dependence of ε_r observed in $BaTiO_3$ is shown in Figure 2.3. This is a prominent example of how down-scaling of characteristic material sizes influences the electrical properties [1][17][18].

Figure 2.3

Dielectric constant of $BaTiO_3$ as a function of the mean grain size [17][18].

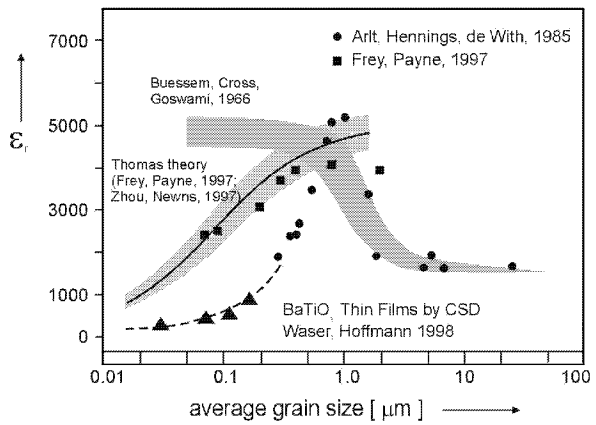

Especially for electronic applications the solid solution series $Ba_{1-x}Sr_xTiO_3$ and $BaTi_{1-y}Zr_yO_3$ play an important role. By changing the material's composition, the value of ε_r at room temperature and the phase transition temperature can be controlled [19]-[21]. Furthermore, in the case of $BaTi_{1-y}Zr_yO_3$ the shape of this maximum can be altered due to a mixing of first and second order phase transitions of $BaTiO_3$ and $BaZrO_3$ [22]. Figure 2.3 shows the behavior of ε_r as a function of temperature for selected compositions for the material systems $Ba_{1-x}Sr_xTiO_3$ and $BaTi_{1-y}Zr_yO_3$, respectively.

By mixing ferroelectric ($BaTiO_3$) and paraelectric materials ($SrTiO_3$ and $BaZrO_3$), the dielectric properties of the material can therefore be tailored to the specific demands of the individual application.

Figure 2.4a.

Temperature dependence of ε_r for selected compositions of the solid solution series $Ba_{1-x}Sr_xTiO_3$ [23]

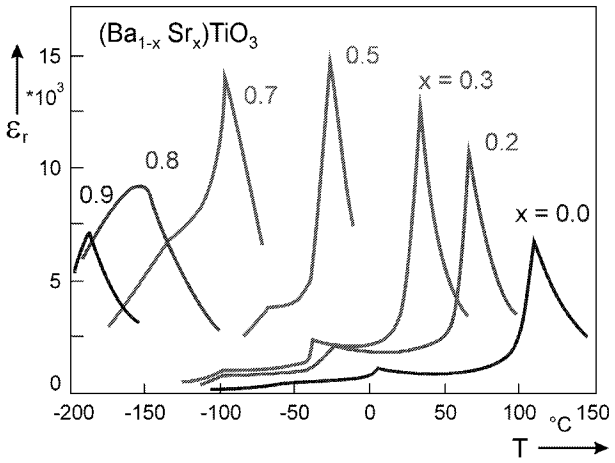

Figure 2.4b.

Permittivity as a function of composition and temperature for $BaTi_{1-y}Zr_yO_3$ [21].

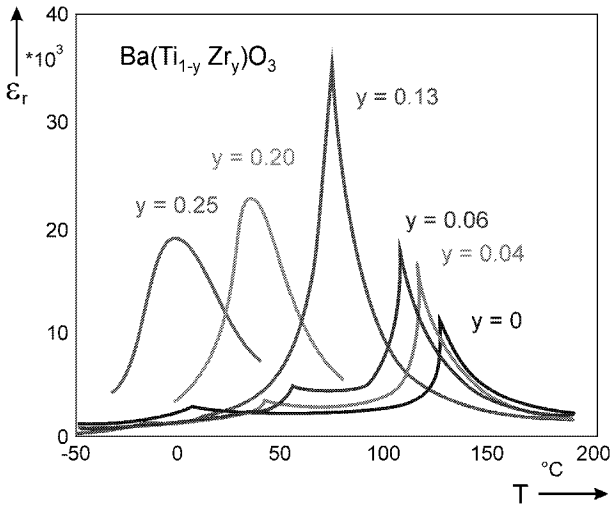

2.3 Band Scheme

Pure $SrTiO_3$ is an insulator due to its large bandgap energy of ~ 3.2 eV at 0 K. At temperatures above 0 K, the bandgap energy decreases according to the rubber-band model and can be expressed as

$$E_G(T) = E_G(0K) - \beta_G \cdot T\,, \tag{2.3}$$

where β_G denotes the temperature coefficient and T the absolute temperature. β_G can be determined from electrical (see also Chapter 6) or optical measurements and is reported to be $\beta_G = 5.66 \cdot 10^{-4} eV/K$ [13] and $\beta_G = 6 \cdot 10^{-4} eV/K$ [14], respectively.

A detailed description of the band structure of $BaTiO_3$, which is similar to $SrTiO_3$, can be found in [15]. The bandgap energy of $BaTiO_3$ is 3.15 eV [24]. For comparison, $BaZrO_3$ exhibits an even larger bandgap of ~ 5 eV [25].

Figure 2.5 sketches the band scheme for $SrTiO_3$ (the Kröger-Vink notation used here will be explained in the following chapter). The valence band is basically built up by the oxygen 2p-states, whereas the conduction band is composed of the 3d-states of titanium. The density of states in the valence or conduction band, respectively, was determined by Moss by electrical measurements [13] as

$$N_C(T) = 4.1 \cdot 10^{16}\ cm^{-3}(T/K)^{3/2} \tag{2.4}$$

$$N_V(T) = 2.5 \cdot 10^{16}\ cm^{-3}(T/K)^{3/2}\ . \tag{2.5}$$

In Figure 2.5 also the energy levels of acceptor dopants (Mn, Ni and Fe), a virtual shallow donor and vacancies of the matrix constituents Sr and O are given. In the case that such a 'defect' can change its valence state, these levels are also stated.

Figure 2.5

Band scheme with energy levels of various 'defects' and different valence states (to scale) for $SrTiO_3$ at $T = 0$ K. Taken from [26].

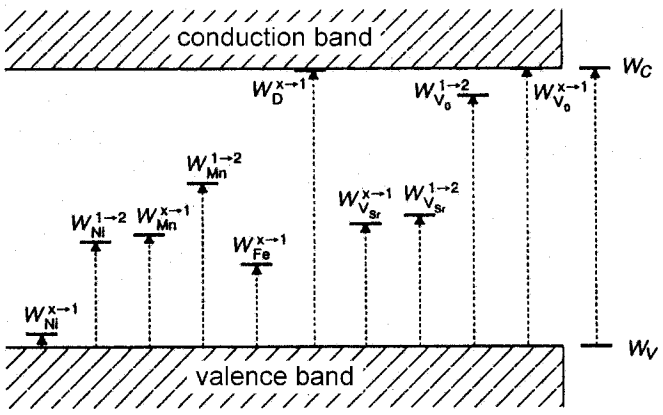

It is apparent from this figure that donors and especially oxygen vacancies are easily ionized even at low temperatures. These circumstance become very important for the conductivity behavior of mixed ionic and electronic conducting materials, which is described in detail in the following chapter.

References

[1] S. Hoffmann, "Modifizierte Erdalkalititanat-Dünnschichten für integrierte Bauelemente: Morphologie, dielektrische Eigenschaften und Ladungstransportmechanismen", PhD thesis, RWTH Aachen, Fortschrittberichte VDI, Reihe 9, Nr. 288, Düsseldorf, 1998.

[2] G.M. Choi, H.L. Tuller and D. Goldschmidt, "Electronic transport in single crystalline $Ba_{0.03}Sr_{0.97}TiO_3$", *Phys. Rev. B* **34**, 6972 (1986).

[3] P. Erhart, "Kristallstrukturen in Oxiden", in: *Elektrokeramische Materialien*, 26. IFF-Ferienkurs, ISBN 3-89336-146-4, Forschungszentrum Jülich, 1995.

[4] F.S. Galasso, *Perovskites and High-T_C - Superconductors*, Gordon and Breach, 1990.

[5] F.W. Lyttle, "X-ray diffractometry of low-temperature phase transformation in strontium titanate", *J. Appl. Phys.* **35**, 2212 (1964).

[6] R. Meyer, "Modellierung transienter Vorgänge in donatordotiertem Strontiumtitanat", PhD thesis, RWTH Aachen, Fortschrittberichte VDI, Reihe 21, Nr. 328, Düsseldorf, 2002.

[7] J. Gerblinger, "Sauerstoffsensoren auf der Basis gesputterter Strontiumtitanat-Schichten", PhD thesis, Universität Karlsruhe, 1991.

[8] R.D. Shannon, "Revised Effective Ionic Radii and Systematic Studies of Interatomic Distances in Halides and Chalcogenides", Acta Crystallogr. **A32**, 923 (1998).

[9] R. Moos and K.H. Härdtl, "Defect Chemistry of Donor-Doped and Undoped Strontium Titanate Ceramics between 1000 °C and 1400 °C", *J. Am. Ceram. Soc.* **80**, 235 (1997).

[10] A. Cocco and F. Massazza, "Esame microscopico del sistema SrO-TiO_2", *Ann. Chim.* **53**, 883 (1963).

[11] E.M. Levin, C.R. Robbins and H.F. McMurdie, *Phase Diagrams for Ceramists*, M.K. Reser, ed., American Ceramic Society, Columbus, Fig. 555, 1969.

[12] G.J. McCarthy, W.B. White and R. Roy, "Phase Equilibria in the 1375 °C Isotherm of the System Sr-Ti-O", *J. Am. Ceram. Soc.* 52, 463 (1969).

[13] R. Moos, "Donatordotierung in Strontiumtitanat: Elektrische Eigenschaften und modellhafte Beschreibung", PhD thesis, Universität Karlsruhe, Fortschrittberichte VDI, Reihe 5, Nr. 362, Düsseldorf, 1994.

[14] T. Bieger, J. Maier and R. Waser, "Optical Investigations of Oxygen Incorporation in $SrTiO_3$", *Solid State Ionics* **53-56**, 578 (1992).

[15] Ch. Hagendorf, "Oberflächenphysikalische Untersuchungen an ein- und polykristallinen $BaTiO_3$", PhD thesis, Universität Halle-Wittenberg, 2000.

[16] R.C. Neville, B. Hoeneisen and C.A. Mead, "Permittivity of strontium titanate", *J. Appl. Phys.* **43**, 2124 (1972).

[17] N. Setter and R. Waser, "Electroceramic Materials", *Acta Mater.* **48**, 151 (2000).

[18] G. Arlt, D. Hennings and G. de With, "Dielectric properties of fine-grained barium titanate ceramics", *J. Appl. Phys.* **58**, 1619 (1985).

[19] Landolt-Börnstein, "Numerical Data and Functional Relationships in Science and Technology: Ferroelectric Oxides", III, 16a, New Series, Springer, Berlin, 1981.

[20] A.D. Hilton and B.W. Ricketts, "Dielectric Properties of $Ba_{1-x}Sr_xTiO_3$ Ceramics", *J. Phys. D* **29**, 1321 (1996).

[21] D. Hennings, A. Schnell and G. Simon, "Diffuse ferroelectric phase transitions in $Ba(Ti_{1-y}Zr_y)O_3$ ceramics" *J. Am. Ceram. Soc.* **65**, 539 (1982).

[22] R. Waser, D. Hennings and T. Baiatu, "Dielektrische Keramiken", in: H. Schaumburg, *Keramik*, Vol. 5, Werkstoffe und Bauelemente der Elektrotrechnik, Teubner Verlag, Stuttgart, 1994.

[23] G.A. Smolenskii and K.I. Rozgachev, "Segnetoelektricheskie Svoistva Tverdykh Rastvorov v Sisteme Titanat Bariya Titanat Strontsiya", *Zh. Tekh. Fiz.* **24**, 1751 (1954).

[24] A.J.M.H. Seuter, "Defect Chemistry and Electrical Transport Properties of Barium Titanate", *Philips Res. Repts. Suppl.* **3**, 1974.

[25] O.I. Prokopalo, I.P. Raevskii, M.A. Malitskaya, Y.M. Popov, A.A. Bokov and V.G. Smotrakov, "Peculiar Electric and Photoelectric Behaviour of Lead-Containing Perovskite Type Oxides", *Ferroelectrics* **45**, 89 (1982).

[26] R. Hagenbeck, "Simulation der elektrischen Korngrenzeigenschaften akzeptordotierter $SrTiO_3$-Keramiken", PhD thesis, RWTH Aachen, Fortschrittberichte VDI, Reihe 9, Nr. 284, Düsseldorf, 1998.

3 Defect Chemistry of Titanates

As already indicated in the last chapter, the electrical conduction characteristics of $SrTiO_3$ and other titanates are closely related to the defect structure of the material. Besides the intrinsic generation of electrons and holes by thermal activation over the bandgap, the extrinsic generation of charge carriers due to compensation reactions for lattice defects is of major significance.

Point defects are amongst the most important defects in crystalline solids. Intrinsic point defects are electrons and holes, interstitials (Frenkel disorder), which are less significant here, and vacancies in the Sr-, Ti- and especially O-sublattices (Schottky disorder). These defects occur for thermodynamical reasons or due to impurity accommodation. Extrinsic point defects are doping elements, i.e. the substitution on regular lattice sites as described briefly in the last chapter.

After some general considerations, the important model of point defect chemistry will be illustrated in the first part of this chapter [1][2]. This concept describes the correlation between the stoichiometry, the equilibrium concentrations of defects and charge carriers as well as their variation with respect to changes of thermal, chemical or electrical parameters by means of solid state thermodynamics. Special attention will be given to the interplay between the electrical conductivity and the surrounding oxygen partial pressure.

Besides the large field of point defect chemistry, also studies on defects of higher dimension should be briefly mentioned. Few investigations have addressed the effects of one-dimensional defects like dislocations on the conduction properties [3]. Two-dimensional defects are, for instance, twin boundaries or stacking faults, as occur in the layered structures of the Ruddlesden-Popper phases [4][5]. Interfaces, like grain boundaries and surfaces, also have a significant impact on the electrical characteristics of the material. They therefore have been subject of detailed research and will be briefly described here [6]-[11].

The last section briefly outlines the fundamental aspects for this work.

3.1 Classical Point Defect Chemistry of Bulk Materials

A general formalism for defect notation and handling of excess charges, introduced by Kröger and Vink [12], is illustrated in Figure 3.1.

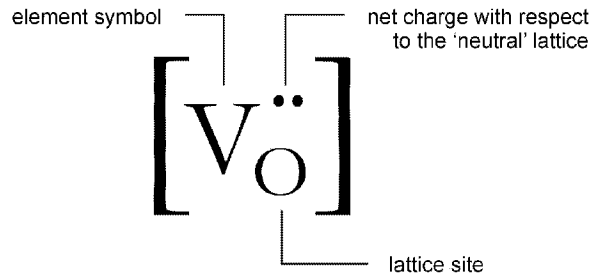

Figure 3.1

Kröger-Vink notation for the example of a doubly ionized oxygen vacancy. See text.

This notation denotes the individual deviation from the undisturbed, ideal crystal lattice. The prevailing defect is assigned by the main index. This is the element symbol or 'V', which represents a vacancy. The subscript refers to the occupied lattice site, which is also marked by the element symbol or 'i' for an interstitial site. The superscript indicates the net excess charge of the defect with respect to the initial lattice charge, which is defined as neutral. A point ($^{\bullet}$) accounts for one positive charge and a prime ($'$) for a negative one. A neutral (or isovalent) situation is indicated by an x (^{x}).

3.1.1 Fundamental Defect Equilibria

In this section, the prevailing defect reactions in $SrTiO_3$ will be elucidated. The temperature range is divided into three regimes, which are characterized by different dominating exchange reactions. These will be discussed in the following starting from low temperatures and going to higher temperatures adding the relevant reactions stepwise.

- **T < ~ 500 °C**

In this regime, only electronic ionization reactions are active and have to be taken into account. The diffusion processes of cations can be considered as frozen in. The temperature limit is somehow indefinite, because the diffusion of the individual species, primarily oxygen vacancies, is an exponentially activated process and depends furthermore on the morphology of the material.

One of the most important defect reaction is the intrinsic generation/recombination of electron/hole pairs by the thermal activation of electrons from the valence band (VB) over the bandgap into the conduction band (CB), according to the following equation:

$$\text{nil} \rightleftarrows e' + h^{\bullet} \tag{3.1}$$

e' denotes a (free) electron and $h^{\bullet}$ an electron hole. The associated law of mass action in thermodynamical equilibrium reads:

$$\begin{aligned} n \cdot p &= K_i(T) \\ &= N_C(T) \cdot N_V(T) \cdot e^{-(E_G(0K) - \beta_G T)/k_B T} \end{aligned} \tag{3.2}$$

n and p are the concentrations of electrons and holes, respectively, K_i denotes the reaction constant, N_C and N_V are the densities of states of the conduction and valence band, respectively, E_G the bandgap energy, β_G the temperature coefficient, k_B Boltzmann's constant and T the absolute temperature.

As a reference, the following set of values was taken from Moos [13], who performed a concise quantitative analysis of the exact values for the bandgap parameters, the densities of states as well as for other defect chemical constants.

$$E_G(0K) = 3.25\,\text{eV} \tag{3.3}$$

$$\beta_G = 5.85 \cdot 10^{-4}\ \text{eV/K} \tag{3.4}$$

$$N_C(T) = 4.1 \cdot 10^{16}\ \text{cm}^{-3}(T/K)^{3/2} \tag{3.5}$$

$$N_V(T) = 2.5 \cdot 10^{16}\ \text{cm}^{-3}(T/K)^{3/2} \tag{3.6}$$

Another reaction, which is especially relevant for the trapping of electron holes, is the change of the valence state of acceptor-type doping impurities (here written for a monovalent element):

$$A^x \rightleftarrows A' + h^{\bullet} \tag{3.7}$$

which leads to the mass action expression

$$\frac{[A']}{[A^x]} \cdot p = K_{A'} \cdot e^{-E_A/k_B T} . \tag{3.8}$$

If the acceptor element has more than one valence state, additional ionization levels have to be considered. Mostly, only a second ionization is taken into account:

$$A' \rightleftarrows A'' + h^{\bullet} \tag{3.9}$$

As pointed out in the previous chapter, Fe and Mn, for instance, do show valence states between 2+ and 4+. Values for the energy levels are around 1 eV, e.g. $E_A(Fe^{3+}) = 0.94$ eV [14][15].

- **$500\,°C \leq T \leq \sim 1000\,°C$**

Due to the appreciable diffusion of oxygen vacancies in the lattice within this temperature regime, the oxygen exchange reaction becomes the dominating mechanism with respect to the defect chemistry. That means, the oxygen sublattice and the ambient atmosphere (i.e. the oxygen partial pressure) strive for equilibration. The loss of oxygen from the lattice is given by the following 'reduction reaction':

$$O_O^x \rightleftarrows V_O^{\bullet\bullet} + 2e' + \tfrac{1}{2} O_2 \uparrow . \tag{3.10}$$

If an oxygen atom is taken away from the lattice, it leaves behind an unoccupied lattice site with two bound electrons. Because the ionization energies are very small, the oxygen vacancy acts like an intrinsic donor. Although the information found in literature varies, it can be assumed that in this temperature regime the vacancy is doubly ionized. The ionization energies are quoted as [13]

$$E_{V_O^{\bullet\bullet}} \approx 3\,\text{meV} \tag{3.11}$$

$$E_{V_O^{\bullet}} = 0.3\,\text{eV} . \tag{3.12}$$

The law of mass action yields for Equation (3.10):

$$[V_O^{\bullet\bullet}] \cdot n^2 \cdot (pO_2)^{1/2} = K_{red}(T) = K_{red}^0 \cdot e^{-(\Delta H_{red}/k_B T)} \tag{3.13}$$

with the reduction enthalpy ΔH_{red}. Values from the literature vary between 5.18 eV [16], 5.7 eV [17] and 6.09 eV [13] (see also references herein).

As oxygen vacancies are always present due to compensating effects, oxygen can also be incorporated into the material. The analogous expressions for the 'oxidation reaction' reads:

$$\tfrac{1}{2}O_2 + V_O^{\bullet\bullet} \rightleftarrows O_O^x + 2h^{\bullet} \tag{3.14}$$

$$\frac{p^2}{\left[V_O^{\bullet\bullet}\right]\cdot pO_2^{1/2}} = K_{ox}(T) = K_{ox}^0 \cdot e^{-(\Delta H_{ox}/k_B T)} \tag{3.15}$$

Here, ΔH_{ox} analogously denotes the oxidation enthalpy, which has been reported to be approximately 1.29 eV [16]. It can be shown that [18]

$$\Delta H_{ox} + \Delta H_{red} = 2\cdot E_G(T = 0K)\,. \tag{3.16}$$

- **$T > \sim 1000\,°C$**

At these high temperatures, also the Schottky equilibrium is activated. This means that all the constituents of the lattice become mobile and can be removed from their lattice sites. The vacancy concentrations are related according to the stoichiometric reaction

$$\text{nil} \rightleftarrows V_{Sr}'' + V_{Ti}'''' + 3V_O^{\bullet\bullet}\,. \tag{3.17}$$

The law of mass action reads:

$$\left[V_{Sr}''\right]\cdot\left[V_{Ti}''''\right]\cdot\left[V_O^{\bullet\bullet}\right]^3 = K_s(T) = K_s^0 \cdot e^{-(\Delta H_S/k_B T)} \tag{3.18}$$

ΔH_S denotes the reaction enthalpy and K_S the mass action constant. A concise experimental determination of these values was carried out by Moos [13].

In the last sections, the major defect chemical reactions and the associated mass actions relations have been introduced. In a thermodynamical equilibrium, the overall concentration of the individual species has to be calculated.

In addition, because charged species are dealt with, the condition of electrical neutrality has to be fulfilled. This requires

$$n + 2\left[V_{Sr}''\right] + 4\left[V_{Ti}''''\right] + \left[A'\right] + \left[A''\right] = p + 2\left[V_O^{\bullet\bullet}\right] + \left[D^{\bullet}\right], \tag{3.19}$$

when fully ionized vacancies, an ionized monovalent donor and a divalent acceptor are considered. Equation (3.19) is more a formal equation to illustrate the individual contributions. In practice, in the regimes regarded here, a lot of simplifications can be made, which will be explained later.

3.1.2 Dominant Charge Carriers

Because in this work the relationship between the conductivity of these films and the oxygen partial pressure is the main aspect of interest, in the following only the temperature regime from 500 to 1000 °C will be considered. For the further discussion of the correlation between the conductivity behavior and defect concentrations, only electrons, holes and oxygen vacancies will be included.

On these assumptions, the conductivity is given by the following relation:

$$\sigma_{total} = 2e_0 \cdot \mu_{V_O^{\bullet\bullet}} \cdot [V_O^{\bullet\bullet}] + e_0 \cdot \mu_n \cdot n + e_0 \cdot \mu_p \cdot p\,, \tag{3.20}$$

where σ_{total} denotes the total conductivity, e_0 the unit charge of $1.602 \cdot 10^{-19}$ C and $\mu_{V\ddot{o}}$, μ_p and μ_n the mobilities of oxygen vacancies, electrons and holes, respectively. The associated concentrations of the individual charge carriers are represented by $[V_O^{\bullet\bullet}]$, n and p, respectively. Equation (3.20) is an integral expression for the conductivity in the bulk region as formulated by the point defect chemistry. This model does not account for any inhomogeneities in the material.

The mobilities of the particular charge carrier species show different characteristics. The moving of electrons and holes is explained by band conduction, as long as the mobility is sufficiently high ($\mu \geq 0.1$ cm^2/Vs [19]). If the conducting electrons or holes are localized for a short period at a certain lattice site, the mobility can be described by a hopping mechanism. If the electrons or holes are slowed down by an interaction with the lattice, they are treated as polarons [16][20]. In the regarded temperature regime from 500 to 1000 °C, the mobilities amount to [13]

$$\mu_n(T) = \mu_{n,0} \cdot (T/K)^{-m} = 3.95 \cdot 10^4 \cdot (T/K)^{-1.62}\ \mathrm{cm^2/Vs} \tag{3.21}$$

$$\mu_p(T) = \mu_{p,0} \cdot (T/K)^{-n} = 1.1 \cdot 10^6 \cdot (T/K)^{-2.36}\ \mathrm{cm^2/Vs} \tag{3.22}$$

The movement of oxygen vacancies is controlled by diffusion and is therefore a thermally activated process. It is expressed by the Nernst-Einstein relation for ionic conduction:

$$\mu(T) = \frac{z \cdot e_0}{k_B T} \cdot D_0 \cdot e^{-E_A/k_B T}, \tag{3.23}$$

where z denotes the charge of the ionic defect and D_0 represents the diffusion constant. For oxygen vacancy diffusion in $SrTiO_3$, the following values have been found [21]:

$$\mu_{V_O^{\bullet\bullet}}(T) = 1.0 \cdot 10^4 \cdot (K/T) \cdot e^{-0.86 eV/k_B T}\ cm^2/Vs \tag{3.24}$$

Paladino reported values of 0.98 eV and 1.13 eV, depending on the temperature range of the measurement [22]. The temperature dependence of the oxygen vacancy diffusion will be discussed in more detail in Chapter 6.

It has to be pointed out here that bulk point defect chemistry assumes the mobilities to depend only on the temperature. A dependence on the oxygen partial pressure has not been reported.

To describe the behavior of the conductivity and its dependence on the oxygen partial pressure, the concentrations of the individual charge carriers have to be determined before calculating σ by Equation (3.20).

3.1.3 Acceptor Doped $SrTiO_3$

Due to an inevitable impurity incorporation during processing, also a nominally undoped material shows a slight doping. The nature of the elements that are commonly found primarily show an acceptor-type behavior so that nominally undoped samples can at the same time be treated like deliberately acceptor-doped samples.

The incorporation of an acceptor and the accompanying formation of oxygen vacancies during the preparation of acceptor-doped $SrTiO_3$ from the binary oxides (as usual by the mixed oxide route) can be described by the following, simplified reaction equation [20]. Here, Fe_2O_3 or Mn_2O_3 virtually replace $2TiO_2$.

$$2SrO + A_2O_3 \rightarrow 2Sr_{Sr} + 2A'_{Ti} + 5O_O + V_O^{\bullet\bullet} \tag{3.25}$$

As a direct consequence of this, any acceptor-doped $SrTiO_3$ sample exhibits a specific concentration of oxygen vacancies which is independent of the reduction reaction of Equation (3.10).

Figure 3.2

Equilibrium conductivity characteristics of a $Sr_{0.97}Ba_{0.03}TiO_3$ single crystal. Taken from [18].

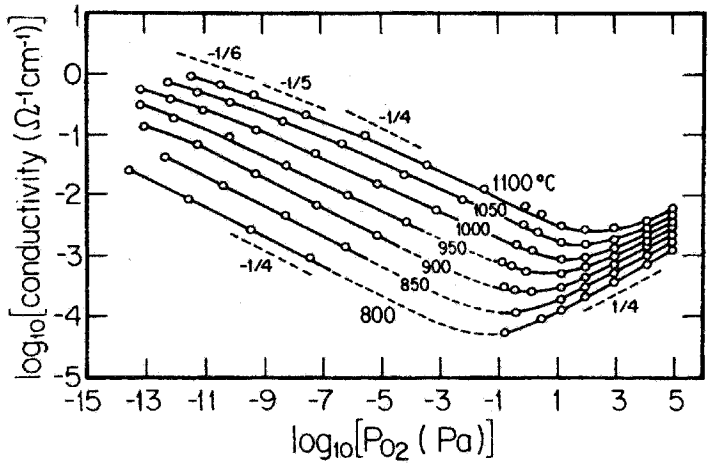

The conduction behavior of nominally undoped titanates, both single crystals as well as coarse grained bulk ceramics, have been studied widely in the past and show a remarkably uniform similarity. Reference measurements on single crystalline $SrTiO_3$ can be found in [13][23], on polycrystalline $SrTiO_3$ in [24], where the influences of a nonstoichiometry in the cation sublattice is also investigated, and the effects of different acceptor-type doping are reported in [25]. As a representative example, Figure 3.2 shows the conduction behavior of a nominally undoped $Sr_{0.97}Ba_{0.03}TiO_3$ single crystal as a function of the oxygen partial pressure in the temperature range from 800 to 1100 °C. Schematically, the characteristics are illustrated in Figure 3.3.

The curves can be divided into four major regimes:

The 'extrinsic' n-type region

In this region, the behavior of σ is dominated by the loss of oxygen to the atmosphere and Equations (3.10) and (3.13) apply. The condition of electroneutrality (Equation (3.19) can be simplified to:

$$n \approx 2\left[V_O^{\bullet\bullet}\right]. \tag{3.26}$$

With this, Equation (3.13) becomes

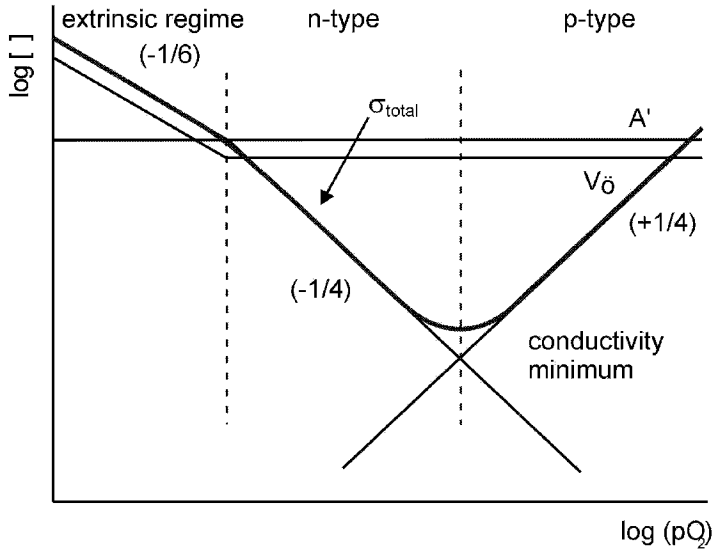

Figure 3.3

Formal illustration of major defect concentrations in acceptor-type doped titanates by means of point defect chemistry. The resulting total conductivity σ_{total} is also drawn.

$$n \approx (2K_{red}(T))^{1/3} \cdot (pO_2)^{-1/6} \tag{3.27}$$

In the log(σ) - log(pO_2) - plot in Figure 3.2, this $(pO_2)^{-1/6}$ - behavior can be identified at the highest temperatures and extremely low oxygen partial pressures. The transition to this region with respect to the oxygen partial pressure depends on the acceptor concentration, i.e. the intrinsic concentration of oxygen vacancies. Because of the extreme conditions with respect to pO_2 and temperature, this regime is often not measured.

The 'intrinsic' n-type region

Towards higher pO_2 values, the oxygen vacancy concentration is virtually unchanged and fixed by the acceptor concentration according to

$$2\left[V_O^{\bullet\bullet}\right] \approx \left[A'_{Ti}\right], \tag{3.28}$$

by which the equation of electroneutrality can be approximated. Then Equation (3.13) reads

$$\begin{aligned} n &\approx \left(\frac{2K_n}{[A']}\right)^{1/2} \cdot e^{-\Delta H_n/2k_B T} \cdot (pO_2)^{-1/4} \\ &\sim (pO_2)^{-1/4}. \end{aligned} \tag{3.29}$$

This relation is valid over a broad pO_2-region and is often called the 'reducing regime', because the sample is reduced by the loss of oxygen to the atmosphere. Apparently, the conductivity changes over several orders of magnitude, which demonstrates the unique properties of titanates. Since electrons are the predominant charge carriers as in the extrinsic region, this regime is (also) assigned 'n-type', see Figure 3.3.

The conductivity minimum

A special characteristic of the conduction behavior is the presence of an intrinsic conductivity minimum. At this point, the sum of the electronic charge carrier concentrations is at minimum and both are nearly equal, so this point is sometimes also called the 'isoelectric' point. The position with respect to the oxygen partial pressure reflects the stoichiometric composition of the material. As will be demonstrated in more detail in Chapter 6, in this minimum region, the contribution by oxygen vacancy diffusion to the total conductivity becomes apparent and quantitative data can be deduced.

The p-type region

Moving to even higher oxygen partial pressures, the intrinsically present oxygen vacancies can be filled successively and the reaction described by Equation (3.14) becomes effective. As a result, holes develop into the dominating charge carriers and therefore this region is called the 'p-type' regime.

$$p \approx \left(\frac{K_p[A']}{2[O_O]}\right)^{1/2} \cdot e^{-\Delta H_p/2k_BT} \cdot (pO_2)^{1/4} \sim (pO_2)^{1/4} . \tag{3.30}$$

Due to a change of the acceptor's valence state, given by Equation (3.7), holes can be trapped when the sample is quenched from a high equilibration temperature down to a low temperature where the oxygen diffusion is frozen in [15]. In contrast to the n-type behavior, which is maintained by quenching to room temperature resulting in a highly conductive material, a p-type equivalent does not exist. This hole-trapping is the reason why acceptor-doped materials are highly insulating and why no semiconducting p-type perovskite is known in the literature in contrast to the n-type semiconducting donor-doped titanates.

The conductivity characteristics portrayed in Figure 3.2 can be described satisfactorily by the model of point defect chemistry which is schematically illustrated in Figure 3.3. An increasing acceptor concentration shifts the curve towards lower pO_2 values, because of the shifted intercept of [A'] and $[V_O^{\bullet\bullet}]$. Higher temperatures cause higher charge carrier concentrations and the curve shifts upward. Due to the larger reduction enthalpy, which is about 5 – 6 eV in contrast to the oxidation enthalpy of 1 – 1.3 eV, the curve is also shifted slightly to higher partial pressures.

Thermopower

If a sample, like strontium titanate, is exposed to a thermal gradient, the redistribution of charge carriers due to the temperature dependence of their mobilities generates a voltage (which has its origin in the Seebeck effect), by means of which the so-called thermopower $\eta = \Delta V/\Delta T$ can be determined. If one charge carrier species dominates the conduction behavior, its sign is reflected by the sign of η. So the determination of the thermopower gives evidence for the predominating charge carrier species.

Figure 3.4 shows the thermopower of a nominally undoped $Sr_{0.97}Ba_{0.03}TiO_3$ single crystal and its dependence on the oxygen partial pressure and temperature [18]. The picture refers to the same sample as was taken for determination of the conductivity characteristics shown in Figure 3.2. As can be seen in this picture, η is negative in the n-type region of the conductivity curve and becomes positive when σ is dominated by electron holes ($h^{\bullet}$). In between, the change of the sign is directly related to the intrinsic minimum of the $\log(\sigma)$ - $\log(pO_2)$ - plot.

Figure 3.4

Thermopower of single crystalline $Sr_{0.97}Ba_{0.03}TiO_3$. Taken from [18].

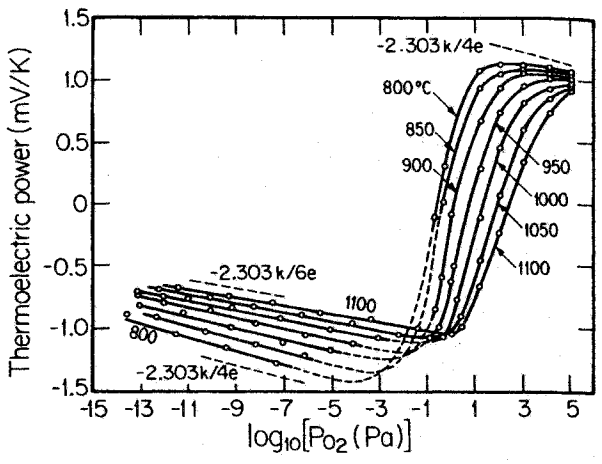

According to [16][27][28] (and references therein), the thermopower of a broad-band semiconductor can be expressed by

$$\eta = \frac{-k_B}{e_0} \cdot \left(\ln \frac{N_C(T)}{n} + A_e \right), \tag{3.31}$$

where n is the charge carrier concentration and A_e a transport factor. Besides the attribution of the sign of the thermopower to the sign of the charge carrier, Equation (3.31) gives the functional correlation between η and n, which by itself is a function of the pO_2. In this way, the slope of the thermopower in the η - $\log(pO_2)$ plot can be calculated from the pO_2 - dependence of the charge carrier concentration.

3.1.4 Donor-Doped $SrTiO_3$

The situation becomes considerably different when the material is doped by a donor-type element, as for example lanthanum [13][25][29]-[32]. Donors have very shallow energy levels and are therefore fully ionized down to temperatures of several K [13][33].

$$D \rightarrow D^{\bullet} + e'. \tag{3.32}$$

Donor-doped strontium titanate may therefore exhibit semiconducting properties with a high conductivity even at room temperature, which is the case when the donors are compensated by electrons. This special behavior is mirrored schematic picture in Figure 3.5 [13].

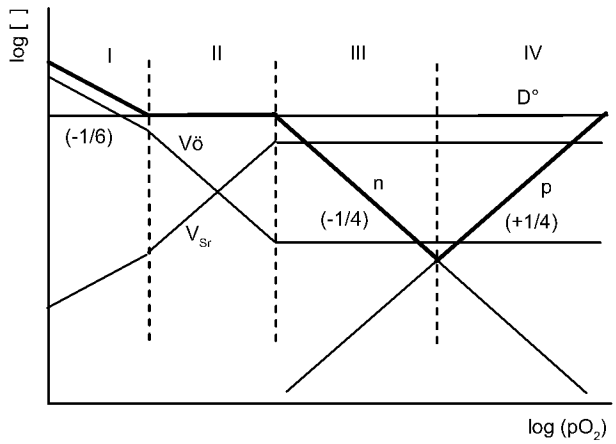

Figure 3.5
Formal description of the defect concentrations as a function of pO_2 for donor-doped titanates.

In region I, the generation of electrons is governed by the reduction reaction of Equation (3.10), and as in the case of acceptor doping, Equations (3.26) and (3.27) are valid. The dependence of the electron concentration n again shows the characteristic slope of - $^1/_6$.

In the subsequent regime II, the compensation of the donors by electrons described above is dominant and the condition of electroneutrality, Equation (3.19), can be simplified to

$$n \approx [D^{\bullet}]. \tag{3.33}$$

The concentration of electrons, and thus also the dominant n-type conductivity, does not change with the oxygen partial pressure. Because σ has the appearance of a plateau, this regime is also called the 'plateau region'. As mentioned above, the excess electron goes into the conduction band, which is built of the Ti 3d-orbitals, and chemically the stoichiometry can be expressed as:

$$Sr_{1-x}^{2+}La_x^{3+}Ti_{1-x}^{4+}Ti_x^{3+}O_3^{2-}. \tag{3.34}$$

By a further increase of the pO_2 to oxidizing conditions, the compensation for the donor impurities is attributed to acceptor-type strontium vacancies [13][30], according to

$$La_{Sr}^{\bullet} + \tfrac{1}{2}Sr_{Sr}^{x} + Ti_{Ti}' + \tfrac{1}{4}O_2 \rightleftarrows \tfrac{1}{2}SrO + \tfrac{1}{2}V_{Sr}'' + Ti_{Ti}^{x} + La_{Sr}^{\bullet}. \tag{3.35}$$

The associated mass action relation is

$$K_{SrO}(T) = \frac{[V_{Sr}'']^{1/2}}{(pO_2)^{1/4}\cdot[Ti_{Ti}']}, \tag{3.36}$$

which is an equivalent expression to Equation (3.29), because [Ti'$_{Ti}$] represents the electron concentration. Therefore, the conduction behavior for donor doped titanates also shows the characteristic slopes of ± ¼ in the regions denoted III and IV in Figure 3.5. To create additional strontium vacancies, the Schottky equation (3.17) has to be active. Titanium vacancies are usually neglected [20].

The conductivity characteristics for $SrTiO_3$ ceramics, which are differently doped with varying amounts of both acceptors and donors, is shown in Figure 3.6. As can be seen, the donor-doped samples clearly show the plateau region with insignificant pO_2 dependence of σ. This plateau

shifts the ±¼ slope-regimes towards higher oxygen partial pressures so that the increasing p-type conductivity is usually not visible. Calculations (lines) applying the considerations of the point defect chemistry presented above show a very good agreement with the measurements and support the assumptions of the model.

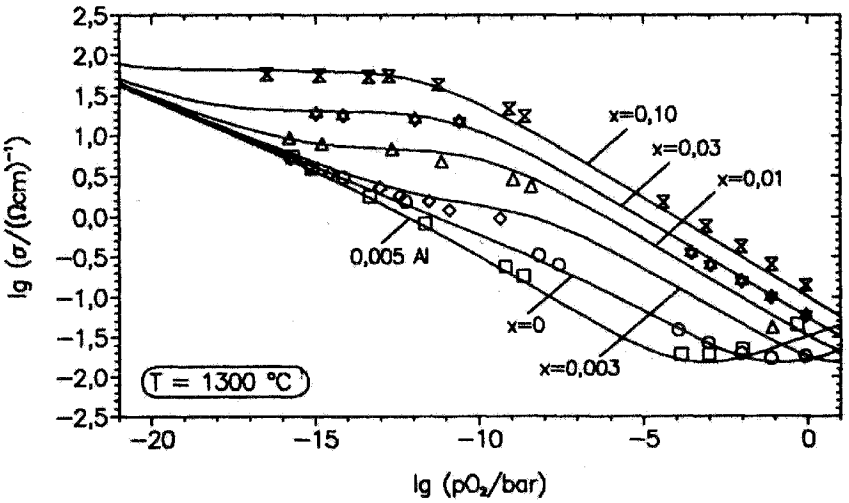

Figure 3.6

Equilibrium conductivity characteristics of polycrystalline lanthanum donor-doped $SrTiO_3$ with variable dopant concentrations [13].

With increasing donor concentration, the plateau region becomes more and more pronounced. This is accompanied by an increased conductivity, as derived from Equation (3.33). A direct consequence of Equation (3.32) is the fact that the donors are usually fully ionized. This means that the concentration of the compensating electrons remains constant in that regime and the conductivity follows the very slight temperature dependence of the electron mobility given in Equation (3.21).

For homogeneous, single-phase perovskite titanates, the point defect chemical model provides a powerful tool for the determination of charge carrier concentration and resulting conductivity profiles.

3.2 Grain Boundaries

The discussion so far has considered only the case of a homogeneous, isotropic system with a diluted concentration of defects, typically a single crystal. As briefly mentioned in the introduction, grain boundaries in polycrystalline ceramics distinctly affect the overall electrical behavior of the material. As in other oxide ceramics, grain boundaries in strontium and barium titanate are highly

resistive [6]-[11][39][40]. They act as barriers and are described by depletion layers at the interface, which is then formally treated as a back-to-back Schottky barrier [6][7][41]-[44].

In p-type $SrTiO_3$ these effects are attributed to a high concentration of positively charged donor states at the grain boundary. Due to this interface charge, positive charge carriers like oxygen vacancies and holes are repelled from the vicinity of the grain boundary while electrons are accumulated. This redistribution of charges leads to the formation of a space charge layer. The increasing resistivity is then explained by the fact that the major charge carriers (in this case oxygen vacancies and holes) have to overcome this positively charged barrier. The situation is schematically shown in Figure 3.7.

Figure 3.7

Simulated space charge profile at a grain boundary in 0.2 at. % Ni-doped $SrTiO_3$ at 250 °C. The surface density of the donor states is $D_{GB} = 1.75 \cdot 10^{14}/cm^2$. Taken from [7].

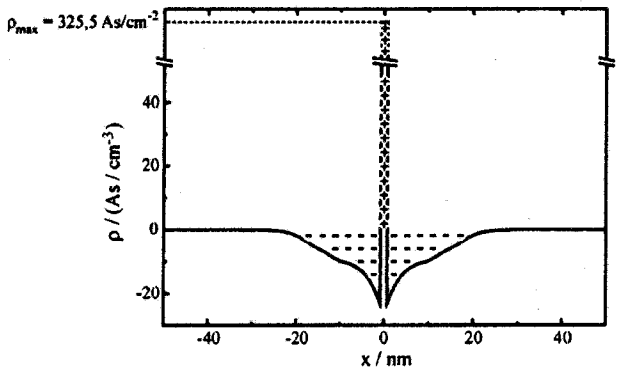

By the combination of experimentally derived material parameters with simulations, the properties of the grain boundary in acceptor-doped $SrTiO_3$ can be well described [6][7][41]-[44]. Due to the depletion of majority charge carriers in this region, the partial conductivities differ radically from these in the bulk, as is exemplarily illustrated in Figure 3.8 for Ni-doped $SrTiO_3$. (A constant mobility of the individual species is commonly assumed). In the grain boundary region, the partial conductivities of the charge carriers dominating the bulk behavior are reduced by many orders of magnitude and are exceeded by the increased contribution of electrons. Depending on the concentrations of the donor-type grain boundary charges, the partial conductivities of electrons in the grain boundary region may be so large that a so-called n-type inversion layer is formed.

The conductivity across the space charge layer is smaller than the bulk conductivity by 1 – 4 orders of magnitude, although there might be an increased electron conductivity along the grain boundary. The width of this space charge layer, which means its electrical influence, extends about 30 – 200 nm into the grain interior. The interface charge density of Ni-doped $SrTiO_3$ ceramics was determined by Vollmann [6] as:

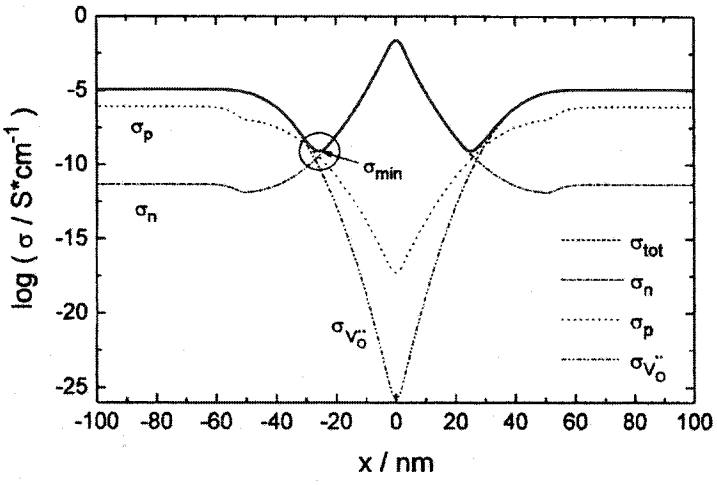

Figure 3.8

Partial conductivities at the grain boundary for 0.2 at.% Ni-doped $SrTiO_3$ at 716 K. Taken from [42]. *For high concentrations of donor-type surface charges the partial electron conductivity can increase by orders of magnitude, thus forming an n-type inversion layer and a W-shaped characteristic of the conductivity.*

$$Q_{GB} \approx 0.13\ C/m^2 \tag{3.37}$$

Despite the success of this model description, the physical nature of the interface and the origin of the donor states is still a matter of discussion and the results that can be found in the literature are sometimes contradictory.

Numerous HRTEM studies revealed that the grain boundary is free of any amorphous phase and that the structural accommodation between two grains stretches approximately over only a few nanometers [6]. Compositional investigations of the grain boundary region in $BaTiO_3$ and $SrTiO_3$ by Chiang and Takagi revealed a strong segregation of acceptor impurities to the grain boundary [9][10]. Typically, their concentration rises by a factor of 4 – 8 compared to the background concentration due to intentional doping. In contrast, a segregation of donors was not observed. In addition, they also found an excess concentration of Ti, which amounted to 20 – 80 % of a monolayer. The accumulation of Ti at interfaces was also found by Hagendorf [46]. Structural investigations in combination with theoretical modeling also confirm this picture of Ti-rich layers at grain boundaries [45][47][48]. Interestingly, these investigations also revealed an oxygen deficiency at the interface due to unoccupied lattice sites and an oxygen vacancy segregation to the boundary. These vacancies, which are assumed to be immobile and unable to diffuse due to a lack of space, are compensated by electrons, which form an n-type layer at the interface [47]. Because the height of Schottky barriers is temperature-dependent, it is expected that the barrier character diminishes for increasing temperatures.

3.3 Surfaces

It is evident that for reduced sample thicknesses, i.e. a decreasing surface-to-volume ratio, the influence of the surface may become important. In comparison to a grain boundary, the surface represents a fundamentally different situation, because it does not separate two regions of the same material but the solid from an ambient atmosphere. In recent years, the surface region of barium titanate and especially of strontium titanate has been subject of increasing research efforts, making use of state-of-the-art surface-sensitive methods [46][49]-[52]. Especially effective analytical tools are atomic force microscopy (AFM), scanning tunneling microscopy (STM), by means of which atomic resolution can be achieved, x-ray photoemission spectroscopy (XPS), electron diffraction (LEED, RHEED) or mass spectroscopy of secondary particles generated by ion bombardment of the surface (SIMS, SNMS), to name just a few.

It is revealed that the surface region of titanates can be restructured by exposing the sample to extreme atmospheric conditions, elevated temperatures and prolonged annealing times [49]-[51][53]. Szot found the formation of droplets and terrace-like structures on the surface of $SrTiO_3$ after annealing for 24 hours at 1000 °C under oxidizing atmospheres ($pO_2 \sim 1$ bar) [51]. A compositional analysis, which revealed an enrichment of Sr, led to the suggesttion of the formation of Ruddlesden-Popper phases $(SrO)\cdot(SrTiO_3)_n$ [4][5]. The formation of such morphological modifications required temperatures of 1000 - 1100 °C and annealing times between 24 and 48 hours. Hagendorf observed a similar behavior in the case of $BaTiO_3$ [46]. In contrast, Kazimirov also reports the formation of small droplets under oxidizing conditions, but attributed them to monoclinic TiO [53].
Under reducing conditions ($pO_2 \sim 10^{-11}$ bar), Szot also proved the growth of steps and an enrichment of Ti in the surface region (or depletion of Sr and O, respectively) [50]. The restructuring of surfaces and the formation of steps already start at temperatures of 800 °C, but the changes then remain within a lateral size of some nanometers. Due to the fact that segregation is a thermally activated diffusion process, it is evident that the observed effects become larger for higher temperatures and longer annealing times.

Unfortunately, to date no quantitative description of the correlation between oxygen partial pressure, temperature, annealing time and the extent of these segregation processes has been published.

3.4 Summary

In this chapter the defect chemistry of alkaline earth titanates, in particular the characteristic interrelationship between the conductivity and the oxygen partial pressure, has been described. Innumerable investigations on this topic have focused especially on the materials $BaTiO_3$ and $SrTiO_3$ and selected papers have been cited. The results which were reported for a large variety of different morphologies (from single crystalline to polycrystalline with grain sizes in the micrometer regime), varying stoichiometries ($BaTiO_3$, $SrTiO_3$ and their solid solutions), nonstoichiometries, and diverse doping incorporation, are amazingly similar. Table 3.9 gives an overview of some important papers on original and comprehensive work.

Table 3.9

Selected publications featuring conductivity characteristics of alkaline earth titanates as a function of pO_2.

system	morphology	nonstoichiometry/doping	ref
$SrTiO_3$	single crystal	-	[13][23]
"	polycrystalline	Al, Fe, Cr	[35]
"	polycrystalline, > 5 µm	Al, TiO_2 excess	[24]
"	polycrystalline	La	[13][30]
$Ba_{0.03}Sr_{0.97}TiO_3$	single crystal	-	[16][18]
$BaTiO_3$	poly + single crystal	BaO excess, Fe	[36]
"	polycrystalline	Al, Nb, TiO_2 excess	[37][38]

To the best of the author's knowledge, no specific information on the behavior of the $BaTi_{1-y}Zr_yO_3$ system has been published. The substitution of titanium by zirconium introduces a hardly to reduce element to the lattice. In addition, zirconates require much higher sintering temperatures than titanates. However, due to the fact that Zr always has the valence 4+, a decreasing sensitivity to reduction with increasing Zr content is expected for $BaTi_{1-y}Zr_yO_3$.

As far as grain sizes are stated explicitly, they have always been in the micrometer regime. Defect chemical investigations on nanocrystalline $Ba_{1-x}Sr_xTiO_3$ materials with feature sizes of a few tens of nanometers, as observed in polycrystalline thin films, have still not been reported.

References

[1] J. Maier, Festkörper - Fehler und Funktion - Prinzipien der Physikalischen Festkörperchemie, B.G. Teubner Verlag, Wiesbaden, 2000.

[2] R. Waser, D. M. Smyth, "Defect Chemistry, Conduction and Breakdown Mechanism of Perovskite-Structure Titanates", in: *Ferroelectric Thin Films: Synthesis and Basic Properties,* J.F. Scott, ed., Gordon & Breach, 1994.

[3] K. Szot, W. Speier, R. Carius, U. Zastrow and W. Beyer, "Localized Metallic Conductivity and Self-Healing during Thermal Reduction of $SrTiO_3$", *Phys. Rev. Lett.* **88**, (2002).

[4] S.N. Ruddlesden and P. Popper, "New compounds of the K_2NiF_4 type", *Acta Cryst.* **10**, 538 (1957).

[5] S.N. Ruddlesden and P. Popper, "The compound Sr_3TiO_7 and its structure", *Acta Cryst.* **11**, 54 (1958).

[6] M. Vollmann, "Elektronische Korngrenzeigenschaften akzeptordotierter $SrTiO_3$-Dielektrika", PhD thesis, RWTH Aachen, Fortschrittberichte VDI, Reihe 9, Nr. 246, Düsseldorf, 1997.

[7] R. Hagenbeck, "Simulation der elektrischen Korngrenzeigenschaften akzeptordotierter $SrTiO_3$-Keramiken", PhD thesis, RWTH Aachen, Fortschrittberichte VDI, Reihe 9, Nr. 284, Düsseldorf, 1998.

[8] Th. Hölbling, "A Simulation Model for Large-Signal dc Charge Transport Phenomena in p-type $SrTiO_3$", PhD thesis, RWTH Aachen, Shaker, Aachen, 2003.

[9] Y.M. Chiang and T. Takagi, "Grain Boundary Chemistry of Barium Titanate and Strontium Titanate: I, High-Temperature Equilibrium Space Charge", *J. Am. Ceram. Soc.* **73**, 3278 (1990).

[10] Y.M. Chiang and T. Takagi, "Grain Boundary Chemistry of Barium Titanate and Strontium Titanate: II, Origin of Electrical Barriers in Positive-Temperature-Coefficient Thermistors", *J. Am. Ceram. Soc.* **73**, 3286 (1990).

[11] R.A. De Souza, O. Kienzle, J. Fleig, J. Maier and M. Rühle, "Electrical and Structural Characterization of a Low Angle Tilt Grain Boundary in Fe-doped $SrTiO_3$", in: *Ionic and Mixed Conducting Ceramics IV*, T.A. Ramanarayanan, W.L. Worrell, and M. Mogensen, eds., 226, Vol. **PV 2001-28**, The Electrochemical Society, Pennington, 2001.

[12] F.A. Kröger and H.J. Vink, "Relations between the Concentrations of Imperfections in Crystalline Solids", in: F. Seitz and D. Turnbull, eds., *Solid State Physics* **3**, 307 (1956).

[13] R. Moos, "Donatordotierung in Strontiumtitanat: Elektrische Eigenschaften und modellhafte Beschreibung", PhD thesis, Universität Karlsruhe, Fortschrittberichte VDI, Reihe 5, Nr. 362, Düsseldorf, 1994.

[14] R. Waser, T. Bieger and J. Maier, "Determination of Acceptor Concentrations and Energy Levels in Oxides using an Optoelectrochemical Technique", *Sol. Stat. Commun.* **76**, 1077 (1990).

[15] R. Waser, "Bulk Conductivity and Defect Chemistry of Acceptor-Doped Strontium Titanate in the Quenched State", *J. Am. Ceram. Soc.* **74**, 1934 (1991).

[16] G.M. Choi and H.L. Tuller, "Defect Structure and Electrical Properties of Single-Crystal $Ba_{0.03}Sr_{0.97}TiO_3$", *J. Am. Ceram. Soc.* **71**, 201 (1988).

[17] H. Yamada and G.R. Miller, "Point Defects in Reduced Strontium Titanate", *J. Sol. Stat. Chem.* **6**, 169 (1973).

[18] G.M. Choi, H.L. Tuller and D. Goldschmidt, "Electronic transport in single crystalline $Ba_{0.03}Sr_{0.97}TiO_3$", *Phys. Rev. B* **34**, 6972 (1986).

[19] Ch. Weißmantel and C. Hamann, *Grundlagen der Festkörperphysik*, Springer, Berlin 1980.

[20] R. Waser, D.M. Smyth, "Defect Chemistry, Conduction and Breakdown Mechanism of Perovskite-Structure Titanates", in: *Ferroelectric Thin Films: Synthesis and Basic Properties,* J.F. Scott, ed., Gordon & Breach, 1994.

[21] I. Denk, W. Münch and J. Maier, "Partial Conductivities in $SrTiO_3$: Bulk Polarization Experiments, Oxygen Concentration Cell Measurements, and Defect-Chemical Modeling", *J. Am. Ceram. Soc.* **78**, 3265 (1995).

[22] A.E. Paladino, "Oxidation Kinetics of Single-Crystal $SrTiO_3$", *J. Am. Ceram. Soc.* **48**, 476 (1965).

[23] K. Beetz, "Die geschlossene Festelektrolyt-Sauerstoffpumpe", PhD thesis, Universität Karlsruhe, Fortschrittberichte VDI, Reihe 8, Nr. 358, Düsseldorf, 1993.

[24] N.H. Chan, R.K. Sharma and D.M. Smyth, "Nonstoichiometry in $SrTiO_3$", *J. Electrochem. Soc.* **128**, 1762 (1981).

[25] S. Steinsvik, T. Norby and P. Kofstad, "Electrical Conductivity and Defect Structure in the System $SrTi_{1-x}Fe_xO_{3-y}$", Proceedings of Electroceramics IV, 691 (1994).

[26] W. Menesklou, "Kompensationsmechanismen der Überschußladung in lanthandotiertem Strontiumtitanat", PhD thesis, Universität Karlsruhe, Fortschrittberichte VDI, Reihe 5, Nr. 481, Düsseldorf, 1997.

[27] R. Moos, A. Gnudi and K.H. Härdtl, "Thermopower of $Sr_{1-x}La_xTiO_3$ ceramics", *J. Appl. Phys.* **78**, 5042 (1995).

[28] L.C. Walters and R.E. Grace, "Formation of Point Defects in Strontium Titanate", *J. Phys. Chem. Solids* **28**, 239 (1967).

[29] H.P.R. Frederikse, W.R. Thurber and W.R. Hosler, "Electronic Transport in Strontium Titanate", *Phys. Rev.* **134**, A442 (1964).

[30] U. Balachandran and N.G. Eror, "Electrical Conductivity in Lanthanum-Doped Strontium Titanate", *J. Electrochem. Soc.* **129**, 1021 (1982).

[31] R. Meyer, "Modellierung transienter Vorgänge in donatordotiertem Strontiumtitanat", PhD thesis, RWTH Aachen, Fortschrittberichte VDI, Reihe 21, Nr. 328, Düsseldorf, 2002.

[32] J. Nowotny and M. Rekas, "Defect Chemistry of $BaTiO_3$", *Solid State Ionics* **49**, 135, (1991).

[33] G. Perluzzo and J. Destry, "The characterization of pure and niobium-doped crystals of strontium titanate using Hall, electrical conductivity, and optical measurements", *Can. J. Phys.* **56**, 453 (1977).

[34] J. Maier, "Defektgleichgewichte in Oxiden", in: *Elektrokeramische Materialien*, 26. IFF-Ferienkurs, ISBN 3-89336-146-4, Forschungszentrum Jülich, 1995.

[35] N.G. Eror and U. Balachandran, "High-Temperature Defect Structure of Acceptor-Doped Strontium Titanate", *J. Am. Ceram. Soc.* **65**, 426 (1982).

[36] A.J.M.H. Seuter, "Defect Chemistry and Electrical Transport Properties of Barium Titanate", *Philips Res. Repts. Suppl.* **3** , 1974.

[37] N.H. Chan and D.M. Smyth, "Defect Chemistry of $BaTiO_3$", *J. Electrochem. Soc.* **123**, 1584 (1976).

[38] S.A. Long and R.N. Blumenthal, "Ti-rich nonstoichiometric $BaTiO_3$. I. High-temperature electrical conductivity measurements", *J. Am. Ceram. Soc.* **54**, 515 (1971).

[39] S.S. Villamil, H.Y. Lee and L.C. Burton, "The Resistance of Grain Boundaries in $BaTiO_3$-Based Ceramics", *IEEE Trans. Comp., Hybrids, Manuf. Technol.* **CHMT-12**, 482 (1987).

[40] H. Neumann and G. Arlt, "Maxwell-Wagner Relaxation and Degradation of $SrTiO_3$ and $BaTiO_3$ Ceramics", *Ferroelectrics* **69**, 179 (1986).

[41] M. Vollmann and R. Waser, "Grain Boundary Defect Chemistry of Acceptor-Doped Titanates: Space Charge Layer Width", *J. Am. Ceram. Soc.* **77**, 235 (1994).

[42] M. Vollmann and R. Waser, "Grain Boundary Defect Chemistry of Acceptor-Doped Titanates: Inversion Layer and Low-Field Conduction", *J. Am. Ceram. Soc.* **80**, 2301 (1997).

[43] X. Guo, J. Fleig, and J. Maier, "Separation of Electronic and Ionic Contributions to the Grain Boundary Conductivity in Acceptor-Doped $SrTiO_3$", *J. Electrochem. Soc.* **148**, J50 (2001).

[44] J. Fleig, S. Rodewald, and J. Maier, "Spatially resolved measurements of highly conductive and highly resistive grain boundaries using microcontact impedance spectroscopy", *Solid State Ionics* **136-137**, 905 (2000).

[45] N.D. Browning, J.P. Buban, H.O. Moltaji, S.J. Pennycock, G. Duscher, K.D. Johnson, R.P. Rodrigues and V.P. Dravid, "The influence of atomic structure on the formation of electrical barriers at grain boundaries in $SrTiO_3$", *Appl. Phys. Lett.* **74**, 2638 (1999).

[46] Ch. Hagendorf, "Oberflächenphysikalische Untersuchungen an ein- und polykristallinem $BaTiO_3$", PhD thesis, Universität Halle-Wittenberg, 2000.

[47] R.F. Klie and N.D. Browning, "Atomic scale characterization of oxygen vacancy segregation at $SrTiO_3$ grain boundaries", *Appl. Phys. Lett.* **77**, 3737 (2000).

[48] M. Kim, G. Duscher, N.D. Browning, K. Sohlberg, S.T. Pantelides and S.J. Pennycock, "Nonstoichiometry and the Electrical Activity of Grain Boundaries in $SrTiO_3$", *Phys. Rev. Lett.* **18**, 4056 (2001).

[49] K. Szot, M, Pawelczyk, J. Herion, Ch. Freiburg, J. Albers, R. Waser, J. Hulliger, J. Kwapulinski and J. Dec, "Nature of the surface layer in ABO_3-type perovskites at elevated temperatures", *Appl. Phys. A* **62**, 335 (1996).

[50] K. Szot and W. Speier, "Surfaces of reduced and oxidized $SrTiO_3$ from atomic force microscopy", *Phys. Rev. B* **60**, 5909 (1999).

[51] K. Szot, W. Speier, U. Breuer, R. Meyer, J. Szade and R. Waser, "Formation of micro-crystals on the (100) surface of $SrTiO_3$ at elevated temperatures", *Surface Science* **460**, 112 (2000).

[52] S.V. Kalinin and D.A. Bonnell, "Effect of phase transition on the surface potential of the $BaTiO_3$ (100) surface by variable temperature canning surface potential microscopy", *J. Appl. Phys.* **87**, 3950 (2000).

[53] A. Kazimirov, D.M. Goodner, M.J. Bedzyk, J. Bai and C.R. Hubbard, "X-ray surface diffraction analysis of structural transformations on the (001) surface of oxidized $SrTiO_3$", *Surface Science* **492**, L711 (2001).

4 Sample Preparation and Characterization

Right at the beginning of this work it was seen that the conduction characteristics under different oxygen ambients are markedly affected when materials are scaled down from single crystals or bulk samples in the millimeter range to thin films with feature sizes in the nanometer regime. This means that effects now become influential or dominant that were negligible or even nonexistent in bulk materials. It is evident that a lot of parameters change because the technological methods applied to grow thin films on an atomic or molecular level, like the utilization of organic precursor chemicals and preparation temperatures far below usual sintering conditions, and the necessity of using substrates cause a structural evolution during growth that leads to a quite different morphological habit.

One of the key questions in this work was therefore to reveal which parameters of the thin films affect the electrical properties. For this purpose it was essential to have access to a broad selection of samples, where factors like the morphology and the stoichiometry can be varied extensively. Of course, this is a demand that cannot be fulfilled by only one preparation technique. In the past a lot of different approaches have been taken and successfully developed into powerful tools for the fabrication of thin films or nanocrystalline ceramics. Most of the methods have distinct advantages and complement each other so that the experimental possibilities are highly versatile. Nevertheless, it is still difficult to change one characteristic parameter in a wide range, for instance the grain size, and at the same time to keep all other parameters untouched.

The material system of interest is primarily strontium titanate, $SrTiO_3$. Starting from the undoped situation, the studies should be extended to samples with a deliberate substitution of the cations. Of technical relevance is an acceptor- or a donor-type doping of the material with heterovalent elements in small amounts, like Mn or Fe as acceptors or La as donor. Another interesting question addresses the solid solution series $Ba_{1-x}Sr_xTiO_3$ and $BaTi_{1-y}Zr_yO_3$, where the cations are replaced by the isovalent and chemically similar elements Ba and Zr, respectively. From the structural and chemical point of view, the samples have to be monophase perovskites with a minimum amount of intrinsic impurities and minimal deviation from the stoichiometric

composition ABO_3. Further decisive quantities are the morphology, primarily the grain size, and the thickness of the films.

In this chapter, all the details concerning the preparation and the characteristics of the investigated samples will be given. The first section will briefly describe the demands made on the substrates against the background of electrical measurements and crystal growth. The following parts deal extensively with the advantages and limitations of chemical solution deposition (CSD) and laser ablation (PLD), the two methods by means of which all the thin film samples in this work were grown. The preparation methods of nanocrystalline ceramics and single crystals are then outlined. Besides this, the analytical methods used to characterize the samples with respect to their morphological, structural and topographical properties will be explained. In the last part, all relevant data obtained by these procedures for the investigated samples are finally summarized.

4.1 Substrates

For a precise determination of the intrinsic electrical conduction behavior of titanate-based thin films at high temperatures, the substrate material has to meet certain requirements, primarily with respect to its electrical properties. This is illustrated in Figure 4.1. Commercially available substrates usually have a thickness ranging from a few hundred

Figure 4.1

Longitudinal cross section of a sample. The vertical scale is grossly exaggerated. The sputtered platinum contacts on top are about 100 nm thick.

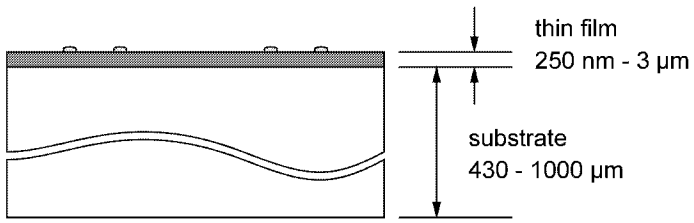

micrometers up to 1 mm. In contrast to this, the film thickness in the present study was varied between 250 nm and 3 µm. As a direct consequence, the conductivity of the substrate must be at least 3 orders of magnitude lower than the minimum value of the film, because the thickness ratio of substrate to film is about 1000:1. In order not to cover the reading of the film, the current through the substrate should not be larger than a few percent of that of the film so only highly resistive materials can be taken into consideration. This is not a problem at room temperature, but the choice of materials becomes more restricted when considering measurement

temperatures of up to 1000 °C. Additionally, the resistivity of the material should also show no or only a small dependence on the oxygen partial pressure.

Table 4.2

Properties of material systems and substrate materials. Data taken from [1][2][3][4].

material systems	lattice parameters	thermal expansion	remarks
$SrTiO_3$	cubic, a = 0.3905 nm	$10.3 \cdot 10^{-6}$ / K	
$BaTiO_3$	tetragonal a = 0.399 nm c = 0.404 nm		
$BaZrO_3$	cubic, a = 0.4192 nm		
substrates			
Al_2O_3 (sapphire) 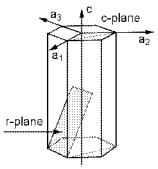	hexagonal a = 0.4758 nm c = 1.1299 nm r-plane ($1\bar{1}02$) a = 0.348 nm	$7.5 - 9 \cdot 10^{-6}$ / K (depending on orientation)	very resistant to chemical solvents for polycrystalline and epitaxial films
MgO	cubic a = 0.4216 nm	$12.8 \cdot 10^{-6}$ / K	rather resistant to solvents well suited for epitaxial growth of titanate thin films

In Table 4.2, the structural data of suitable substrate materials are given. Suitability concerning the electrical properties at various temperatures and oxygen partial pressures cannot be evaluated from literature data. This has to be determined by a so-called 'blank test' of uncoated substrate samples. Additional criteria are the available sizes, the geometry or compatibility with the projected deposition process. Other possible substrate options for future work are lanthanum aluminate ($LaAlO_3$) or LSAT, $(La_{0.18}Sr_{0.82})(Al_{0.59}Ta_{0.41})O_3$, a recently introduced crystal with perovskite structure, but their intrinsic conduction characteristics are not yet known.

For this work, almost all films were grown on r-plane sapphire ($1\bar{1}02$) in the case of chemical solution deposition and on MgO (100) in the case of laser ablation. This was mainly due to extensive experience with this methods and the specific advantages of these combinations. More details will be given in the next two sections.

4.2 Chemical Solution Deposition (CSD)

The growth of complex oxide thin films via the decomposition of organic precursors has been brought to a high degree of versatility and practicability and can be seen as a standard technique in the field of thin film applications today. Chemical approaches offer the advantage of extensive flexibility regarding the material systems and a precise control of stoichiometry and deliberate doping incorporation. Furthermore, the chemistry can be optimized with respect to process conditions and (to some extent) to morphological or structural requirements. Wet chemical methods are characterized by direct application of a precursor solution on the substrate. The CSD processes include sol-gel and the metal-organic decomposition (MOD) methods, which have the highest flexibility concerning the material side and at the same time make limited demands on laboratory equipment.

The basic idea of chemical routes is to make a metal-organic precursor compound that consists of one of the cations and an organic part. Typical precursors are, for instance, alcoholates, $M^{x+}(OR)_x$, carboxylates, $M^{x+}(OOCR)_x$ or β-diketonates, $M^{x+}(RCOCHCOR')_x$. M represents a metal cation and R, R' denote alkyl groups. The precursors are chemically salts and are dissolved in the corresponding acid. Which organic route is used is a question of the decomposition behavior, of its wetting behavior with respect to the chosen substrate, and of the viscosity, which is directly associated with the film thickness of a single coating. Additional (more or less) free parameters are the dilution of the precursor in the solvent and the mixing ratio in the case where different solvents are used for the Ti-precursor and the Ba- or Sr-precursors, respectively. More information on the underlying theoretical aspects, the effects of parametric changes or related processes can be found in [7].

The preparation process of a CSD-derived thin film is illustrated in Figure 4.3 by the exemple of the so-called 'propionate route', by means of which most of the CSD films in this work were made.

The A-site cation (Ba or Sr) is brought in as propionate, $Ba(OCOC_2H_5)_2$ or $Sr(OCOC_2H_5)_2$, respectively. Both are synthesized by a reaction of the corresponding hydroxides, which are commercially available from various suppliers with a high degree of purity, with propionic acid (C_2H_5COOH) [8]. The precipitated and dried propionate powder is then redissolved in propionic acid and builds the first part of the metal organic precursor solution. Another well-established route is the use of acetates, which are dissolved in acetic acid, CH_3COOH.

The other part of the precursor solution comprises titanium tetra-n-butylate ($Ti(OBu^n)_4$ or 'TBT', Merck) as titanium precursor mixed with n-butanol (C_4H_9OH or Bu^nOH). To stabilize this complex and prevent premature precipitation or uncontrolled hydrolysis, the TBT is converted with twice the amount of acetylacetone ($CH_3COCH_2COCH_3$ or 'Hacac') according to

$$Ti(OBu^n)_4 + 2Hacac \rightarrow Ti(OBu^n)_2(acac)_2 + 2Bu^nOH\,. \tag{4.1}$$

The (acac)-ligand builds a double chelate bonding to the titanium, thus creating a complex with the preferred sixfold coordination (see [7] or [9]). This is the same coordination the Ti cation has in the final perovskite structure. TBT is produced in large amounts as a titania precursor and is easily available in high purity grades. In the case of titanate - zirconate solid solutions, the Zr-precursor is $Zr(acac)_4$. A lot of doping elements like Fe, Mn or La are also readily available in the form of acetylacetonates, which are dissolved in propionic acid. The incorporation of dopants is therefore compatible with the existing chemistry and is thus readily accomplished.

Regarding the stoichiometry of the films, it is assumed that in the case of an acceptor-type doping the stoichiometric compensation is governed by oxygen vacancies, given by the defect chemical reaction

$$2MO + A_2O_3 \rightleftarrows 2M_M + 2A'_{Ti} + 5O_O + V_O^{\bullet\bullet}\,, \tag{4.2}$$

where M denotes the Ba- or Sr-cation and A the heterovalent acceptor element, e.g. Mn or Fe. As an example, the chemical formula of iron-doped $SrTiO_3$ then reads

$$SrTi_{1-x}Fe_xO_{3-\delta}\,. \tag{4.3}$$

In the case of donor-doped $SrTiO_3$, which was achieved by the incorporation of lanthanum, the equivalent reaction for sintering under oxidizing atmospheres can be formulated as

$$La_2O_3 + 3TiO_2 \rightleftarrows 2La_{Sr}^{\bullet} + V_{Sr}'' + 3Ti_{Ti} + 9O_O\,. \tag{4.4}$$

Here the compensation should be realized by strontium vacancies V_{Sr}''. The stoichiometric composition is given by

$$Sr_{1-\frac{3}{2}x}La_xTiO_{3-\delta}\,. \tag{4.5}$$

According to the desired stoichiometry and the compensation reactions, the individual precursor solutions are mixed and diluted with propionic acid and n-butanol. The volume ratio of propionic acid to Bu^nOH was usually 2:3. The final concentration of the precursor solution was between 0.1 M and 0.3 M with respect to the B-site component. As was shown in [7], the morphology of the films is sensitively related to the dilution of the precursor chemicals. For the present work, a rather high dilution of 0.1 M was chosen, primarily to obtain very dense films. Just before the coating process, the solution is filtered through a PTFE filter (Millipore) with a pore size of 0.2 µm to remove residual particles. The precursor solutions are regularly analyzed for their stoichiometric composition and impurity concentrations by means of ICP methods (inductive coupled plasma). The results verify an excellent control of the stoichiometry and minor impurity concentrations of approximately 500 ppm, which are mostly acceptor-type elements like Na, K, Al, Cu or Zn [10].

Because of the chemical stability and the high electrical resistivity, sapphire (r-plane, CrysTec) was used as substrate material for the thin films prepared by CSD. Before the first coating, the wafers were cleaned in 2-propanol and/or acetone in an ultrasonic bath for several minutes. Afterwards, they were subjected a 'pre-run' in the furnace to clean the surface of persistent residues or adsorbed water. Initially, temperature and dwell time were adopted from a common pyrolization program (750 °C for 5 or 10 minutes). Many of the films were grown on 2" wafers that were epi-polished on both sides (for optical measurements). In the course of this experimental work, the quality of these substrates distinctly deteriorated, most probably because of stresses inherent in the material due to the polishing procedures, which led to cracking the of wafers. To avoid losses, the pre-annealing procedure was changed to a temperature of 1000 °C and annealing times of 5 hours with very slow heating and cooling rates.

By using round 2" substrates, several samples can be cut, thanks to a very homogeneous coating as far as 2 mm from the margin of the wafer. The coating is performed in two steps (5 s at 500 rpm and subsequently 30 s at 4000 rpm) with a spin-coater (B.L.E. Products). After each (repeated) coating, the sample is passed slowly into a hot diffusion furnace (Centrotherm). During this time (about 2 minutes), the sample heats up, the solvents of the wet film evaporate and the film condenses. At higher temperatures (about 450 °C), the organic residuals of the precursor chemistry start to decompose [7]. To complete this so-called pyrolization, each coating is heated to 750 °C and annealed in flowing oxygen for 5 or 10 minutes. Under these conditions, the coating also crystallizes in the perovskite structure. With these deposition parameters and a 0.1 M propionate-based precursor solution, every single coating yields a thickness of nearly 9 nm. For a final film thickness of about 500 nm, which is typical of this work, 55 or more single

coatings are necessary. Final crystallization and overall densification is achieved by annealing all layers at 800 °C for 1 h in flowing oxygen. Because of the different thermal expansion coefficients of sapphire and titanate materials and increasing stresses, care has to be taken not to induce cracks due to thermal shocks during cooling.

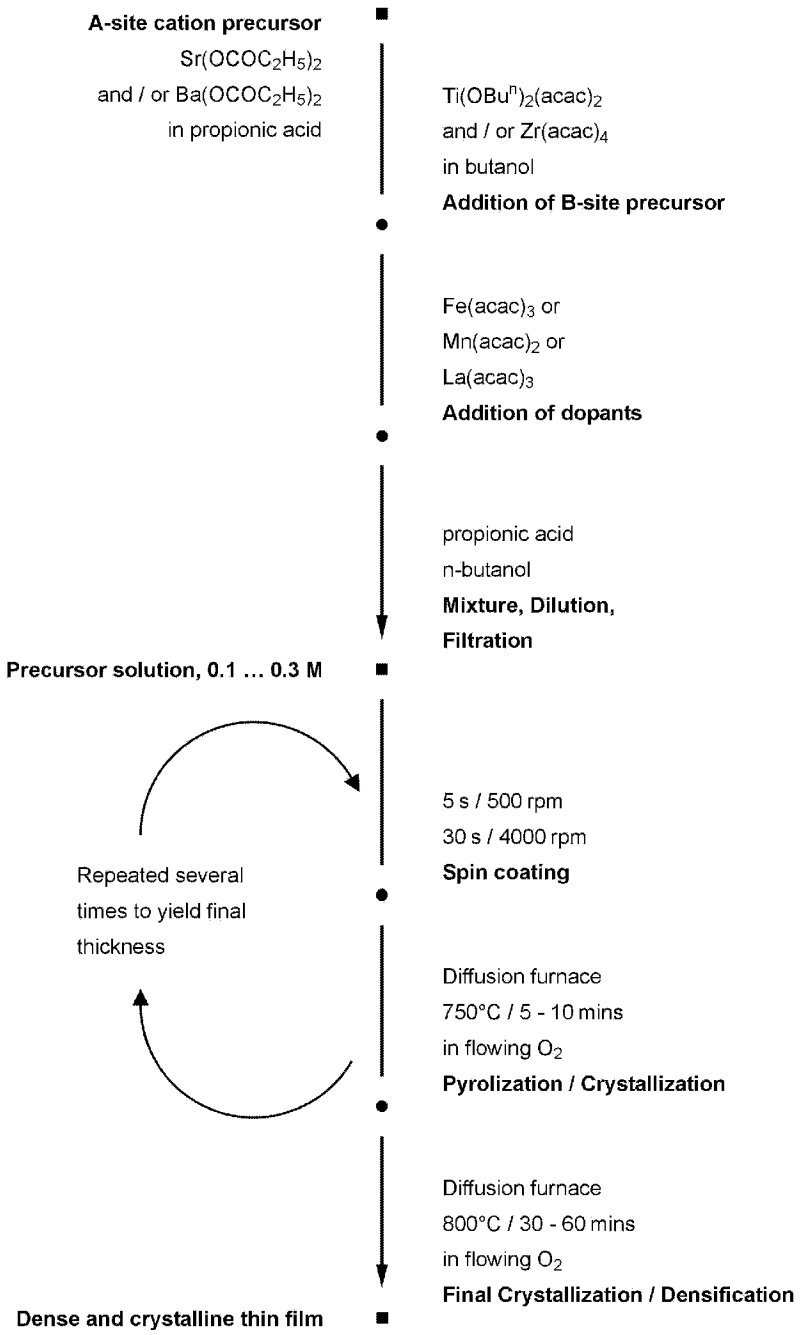

Figure 4.3

Flow chart of a typical CSD process, following the propionate-based route.

The choice of the solvent route, the dilution (also regarding the substrate material) and the deposition parameters are of essential importance for the thin film's morphology. The data given here are typical process parameters, which can vary to accommodate different solvent routes, stoichiometries (material systems) and types of substrate.

Figure 4.4

Cross-sectional SEM picture of an undoped $SrTiO_3$ thin film STO5 made by CSD. The film consists of 55 single layers. The diameter of the columns can be estimated to be about 50 nm.

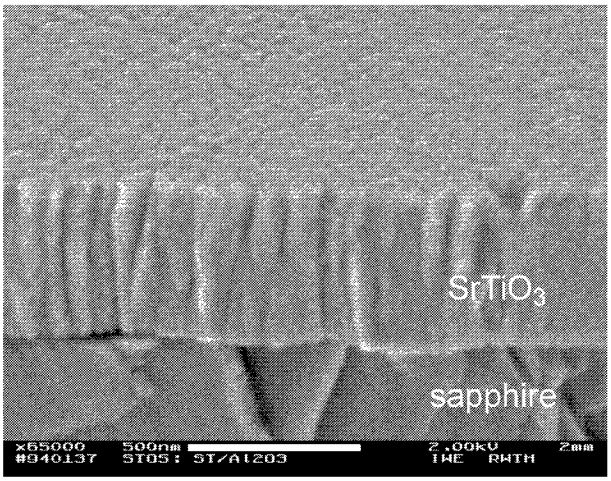

Figure 4.4 shows the morphology of a 500 nm thick, nominally undoped $SrTiO_3$ film grown by 55 single coatings. The image was taken with an SEM (Zeiss Gemini), the primary analytical tool for the qualitative investigation of thin film morphology. This image is a representative depiction of CSD-derived thin films, prepared from propionate based and with 0.1 M highly diluted precursor chemicals. The picture reveals a columnar film morphology with a barely visible intergranular porosity at the boarders of the columns. Earlier studies by x-ray reflectometry (XRR) on similarly processed $SrTiO_3$ thin films gave a density of ~ 97 % of the theoretical value [11]. In general, an inherent porosity of some percent is always seen in thin films as well as in ceramics prepared by wet chemical solution routes, [12][13].

Figure 4.5

Cross-sectional TEM micrograph of the $SrTiO_3$ thin film STO5.

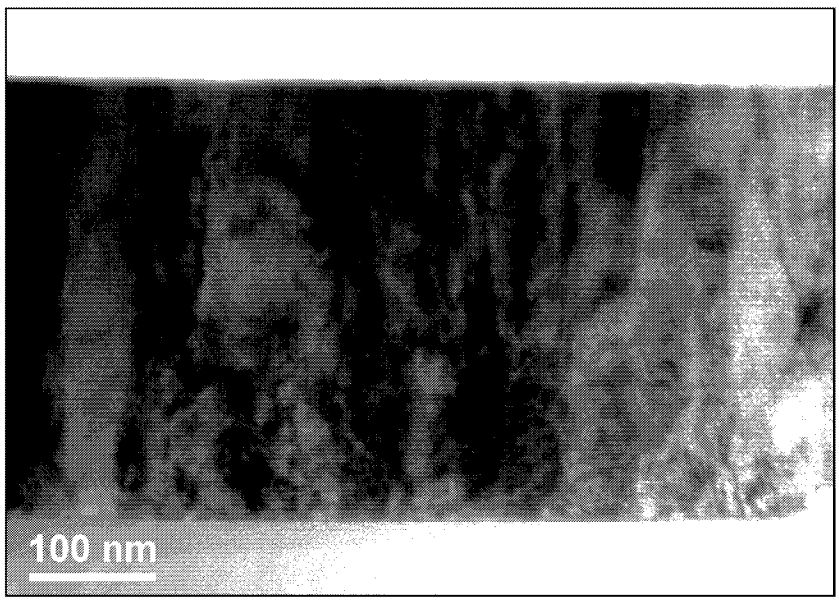

The cross-sectional transmission electron microscopy (TEM, JEOL 4000EX) analysis depicted in Figure 4.5 confirms the polycrystalline and columnar grain structure of the film. The remarkable detail of this image makes visible the tiny pores that can be found beneath each coating. Careful investigation reveals exactly 54 planes corresponding to the 55 single depositions by which this film was grown. This image also gives evidence for the assumption that the columns themselves grow in a single crystalline manner layer by layer [12].

A second, inevitable analysis addresses the structure of the film. This means the orientation of the grains or columns, the possible texture or potential secondary phases. The characterization is performed by x-ray diffractometry (XRD, Philips X'Pert) and the pattern is shown in Figure 4.6. The XRD diagram shows that the $SrTiO_3$ thin film is of polycrystalline perovskite structure without texture and free of secondary phases within the experimental limits. SEM and XRD confirm the high quality of CSD-derived thin films with regard to morphology and phase purity.

Figure 4.6

XRD diagram of the $SrTiO_3$ film shown in Figure 4.4 (STO5). Indexed peaks belong to $SrTiO_3$ [14].

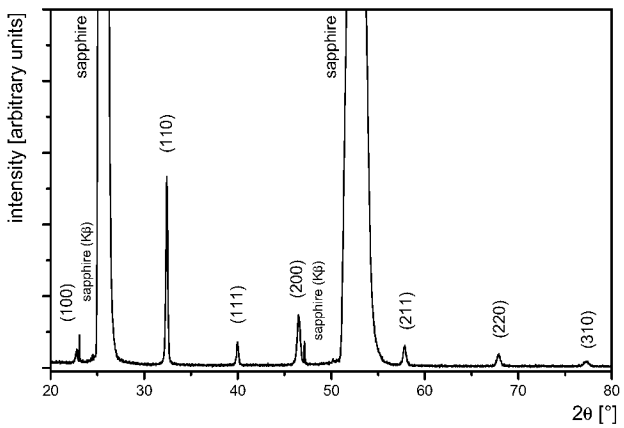

The topographical properties of the film, like the roughness, were studied by atomic force microscopy (AFM). This scanning tool offers an extremely high spatial resolution of a few nm laterally and down to the pm regime vertically. Another advantage is that the surfaces themselves do not have to be conductive. A typical scan is shown in Figure 4.7 for the undoped $SrTiO_3$ film STO5. This tool is especially useful for the detection of the smallest topographical changes of the surface as well as quantitative surface analysis via image processing.

Figure 4.7

AFM picture of STO5. As can be seen, the sample exhibits a quite smooth surface.

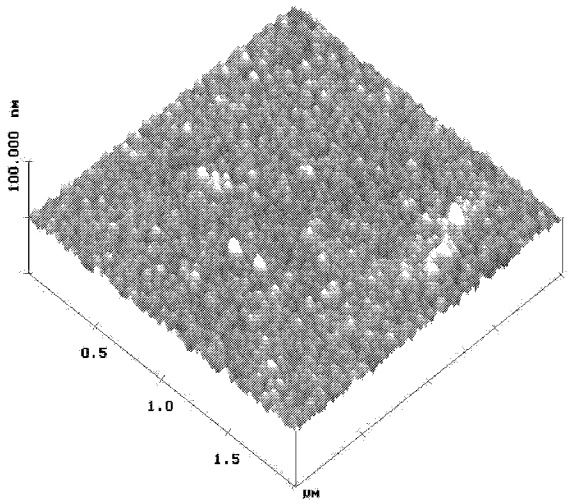

By image analysis, the mean grain diameter (as appears on the surface) can be calculated to be 52 nm, which quantitatively confirms the estimation made by SEM [15]. More detailed information on the applications of the AFM technique for the investigation of titanate surfaces can be found in [16].

4.3 Pulsed Laser Deposition (PLD)

As said before, the CSD process is very flexible regarding a variation of the stoichiometry of the films but is quite restricted when process parameters are to be varied. Another well established and useful technique for growing complex oxide thin films is by pulsed laser deposition (PLD) [17]. This method was used in the late 1980s for the epitaxial growth of superconducting $YBa_2Cu_3O_{7-x}$ films (e.g. [18]) and was then adopted and optimized for growing epitaxial titanate thin films for optical waveguiding applications [19]-[21]. For such applications, single crystalline films without light scattering grain boundaries are necessary and it was shown that single-crystalline $BaTiO_3$ films can be grown epitaxially by PLD on MgO (100) substrates up to some micrometers in thickness [22].

The PLD setup with its basic components is sketched in Figure 4.8. The pulsed laser beam is generated by a KrF excimer laser with a wavelength of 248 nm. This beam is focused by a cylindrical lens to form a line over the whole width of the target. Typical parameters of the laser operation are a pulse energy of ~ 1 J, a pulse length of 25 ns and a focus area of roughly 20 mm^2 on the target, which leads to a power density of one pulse of 0.16 – 0.20 GW/cm^2 [21]. This

energy density causes the atoms of the surface region of the target to evaporate and to form a plasma plume of ionized particles. The geometry of the plume is optimized for a homogeneous deposition on a substrate that is placed into the plasma.

Figure 4.8

Schematic picture of the on-axis PLD setup.

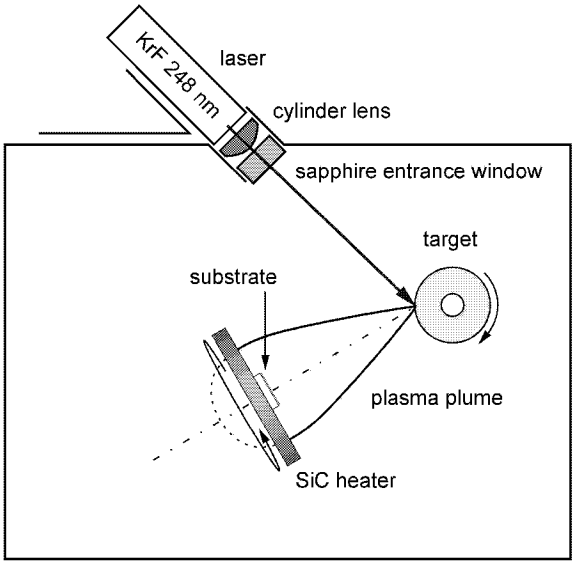

One great advantage of PLD is the stoichiometric material transfer from the target onto the substrate. That means that materials with complex stoichiometries can be grown if only a cylindrical target is available (this can be single crystals as well as ceramics). The disadvantage at the same time is that for a change in stoichiometry a new target must be provided. The target cylinder rotates for a uniform material ablation. The substrate is placed on a rotatable resistive SiC heating element so that the substrate's temperature during deposition can be controlled up to temperatures of 1200 °C. Because the laser is placed outside the chamber, the type and operating pressure of the filling gas inside can be varied widely and become further essential process parameters, by means of which a lot of different nanostructures can be obtained. Although the basic principles of laser deposition sound simple, it still requires a considerable effort to find out the appropriate parameters for growing thin films with precisely tailored properties. An additional task is to keep these parameters identical at each deposition run because, especially for epitaxial growth of films, the interplay between the surface roughness, cleanliness and temperature of the substrate and the energy density of the laser beam on the target is crucial and reacts sensitively to deviations.

Figure 4.9

SEM analysis of PLD-prepared $SrTiO_3$ thin films on MgO with different substrate temperatures during growth.

a. *#3462, deposited at 800 °C < T < 850 °C.*

(#3462 was processed identically and subsequently to #3461)

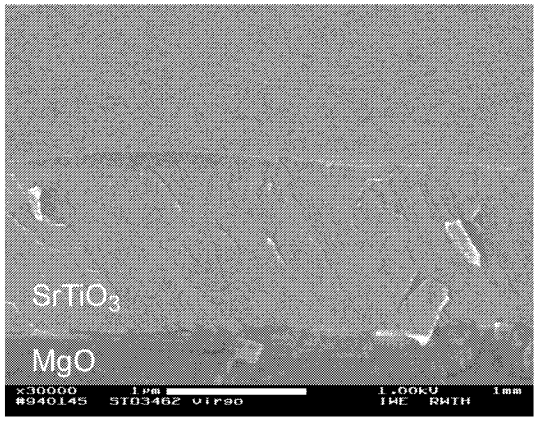

b. *#3666, 750 °C < T < 800 °C.*

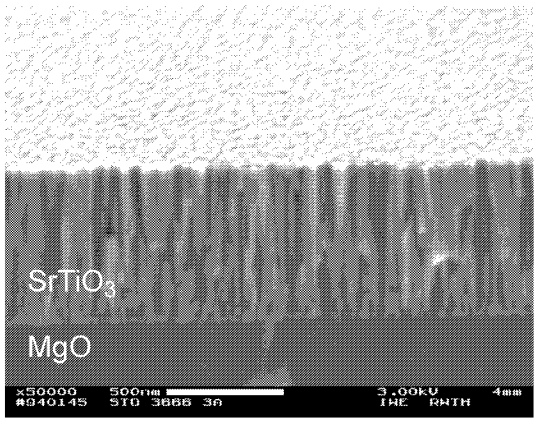

c. *#3667 620 °C < T < 660 °C.*

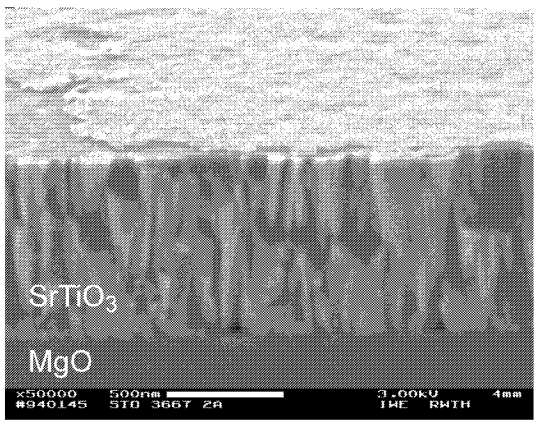

d. *#3668 480 °C < T < 520 °C.*

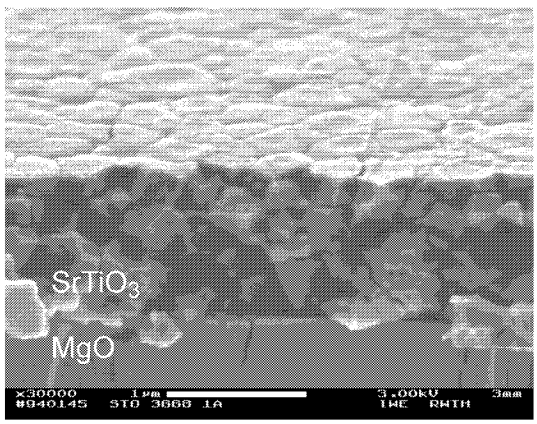

All PLD films in this work were prepared by J. Schubert (ISG 2)

Figure 4.10

XRD patterns corresponding to Figure 4.9

a. *#3461, confirming epitaxial growth. See also the according ϕ - scan in Figure 4.11.*

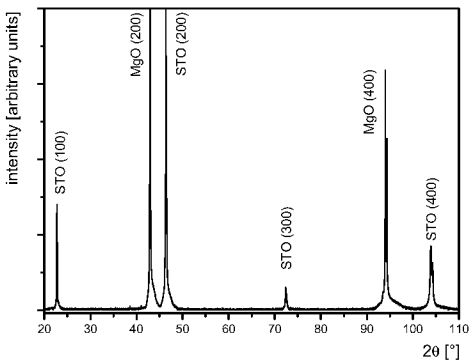

b. *#3666, exhibiting a high degree of texture along the (100) direction.*

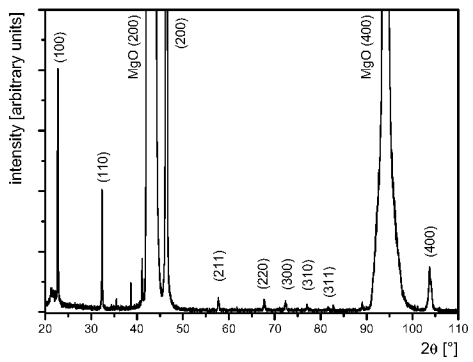

c. *#3667, polycrystalline structure without preferential orientation.*

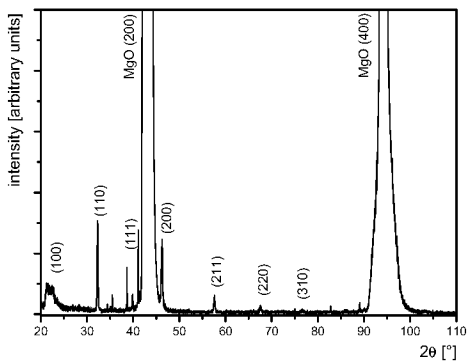

d. *#3668, again randomly oriented, polycrystalline structure.*

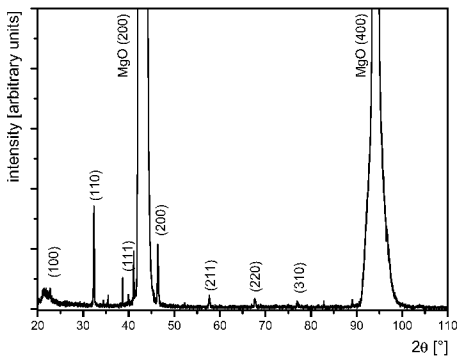

Even though there is a lattice mismatch with respect to MgO of roughly 5 % in the case of $BaTiO_3$ and about 7 % for $SrTiO_3$, it is possible to grow heteroepitaxial titanate thin films on MgO substrates. As will be shown later, MgO is particularly suitable due to its highly insulating properties. A beneficial effect is the larger thermal expansion coefficient of MgO, which puts the film under some compressive stress when cooled down to room temperature. The deposition of heteroepitaxial $SrTiO_3$ thin films was performed at a substrate temperature between 800 and 850 °C and under an oxygen partial pressure of $3 \cdot 10^{-6}$ bar. (The determination of an exact substrate temperature is difficult, because the method used here via a pyrometer is somewhat inaccurate. Usually, the temperature is stated in terms of the heater current.)

Figure 4.9 and 4.10 portray the morphology and the structure of several PLD-processed $SrTiO_3$ thin films on MgO. The SEM picture of the heteroepitaxially grown 1 µm thick film (Figure 4.9a) reveals no indication of any grain boundaries; in addition, the surface roughness is apparently very low. From this view, the film is single crystalline. This is confirmed by a θ - 2θ - scan by x-ray diffraction, shown in Figure 4.10a. As can be seen, only the (n00) - reflections occur, also proving the single orientation on the (100)-oriented MgO substrate. A further verification of the heteroepitaxial growth is that no twisted parts exist. This is proven by the ϕ-scan depicted in Figure 4.11, where reflection peaks only appear every 90 °, according to the fourfold symmetry of the cubic perovskite structure.

Figure 4.11

ϕ-scan of an epitaxial $SrTiO_3$ thin film (#3461).

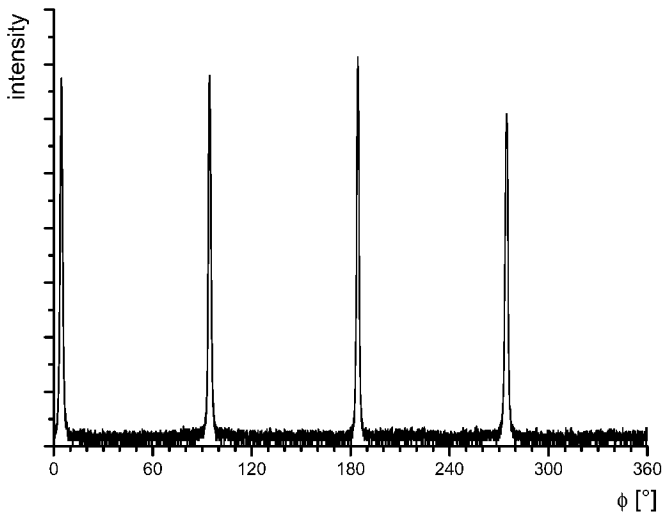

Another analytical tool for the examination especially of epitaxial thin films is Rutherford backscattering spectrometry (RBS) in combination with ion channeling (IC). This technique monitors the interaction of the material with highly energetic He^+-ions (typically 1.4 MeV) that

are shot onto the sample. The energy distribution of the (at a certain angle) backscattered ions allow information to be deduced on the element composition (i.e. the stoichiometry) and the element depth distribution along the incident beam (by means of which for instance the thickness of the film can be determined). This is accomplished by the special simulation program RUMP [23] that simulates the measured spectrum by fitting element and thickness parameters. When the He^+-beam is directed along a lattice orientation, the ions can 'channel' through the lattice and the rate of backscattered ions becomes very low. To avoid influences from this channeling, the sample is tilted by 5 ° and turned during measurement. This is called the 'random' measurement and crystal planes and the direction of the ion beam have a mutual random orientation. The effect of channeling itself is deliberately utilized in a second 'channeling' measurement, where the beam is carefully aligned with respect to the lattice.

Figure 4.12

RBS/IC measurement of an epitaxial $SrTiO_3$ thin film made via PLD (#3461, 1 µm thick).

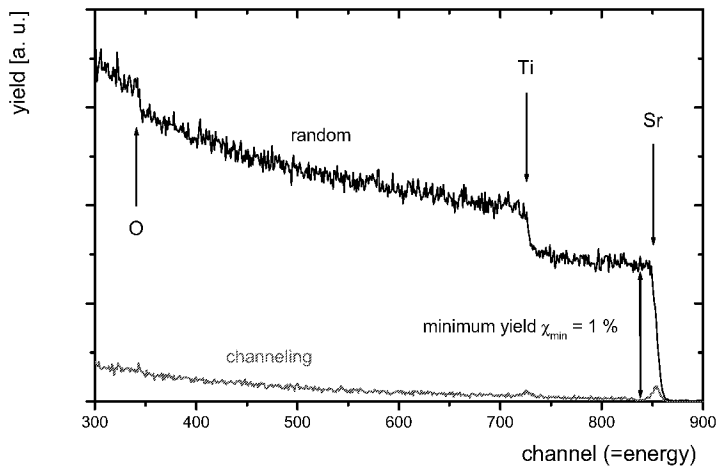

In comparison to the random spectrum, the minimum yield χ_{min} of backscattered ions is a reliable measure for the crystal quality, because lattice imperfections like grain boundaries drastically increase scattering. χ_{min} is given in proportion to the corresponding value of the random spectrum. A typical RBS/IC analysis is shown in Figure 4.12. For a bulk single crystal, χ_{min} is less than 1 % [24]. Common values for the PLD-derived, heteroepitaxial thin films prepared for this work are between 1 and 1.5 %, proving an excellent crystal quality. For further reading on the RBS/IC method, the reader is referred to [25][26].

Two further beneficial applications of the PLD technique were utilized for the thin films studied in this work. The first one addressed the intention of evaluating the influence of the surface on electrical properties, which can be done by varying the film thickness. Fortunately, as mentioned

above, the PLD process offers the possibility of making heteroepitaxial titanate thin films up to a thickness of some micrometers [22]. This means roughly one order of magnitude more than available with CSD. The range of different thicknesses within this work covered films from 250 nm to 3 μm. It should be pointed out in this context that it becomes increasingly difficult to grow single crystalline thin films in the micrometer regime due to larger lattice constrictions. The crystal habit must therefore be considered very carefully.

A second advantage already mentioned is the changing of the film morphology by decreasing the substrate temperature during deposition. A heteroepitaxial growth of the thin film requires a certain minimum temperature. Below this temperature, the film first exhibits a needle-like morphology with a high degree of texture along the (100) - direction perpendicular to the film surface. With further temperature reduction, the texture first disappears and then the film becomes fully polycrystalline, accompanied by a visible change of the size and shape of the grains from columnar to equiaxed. SEM cross section micrographs and XRD patterns of a series from heteroepitaxial to coarse-grained polycrystalline PLD films grown at different substrate temperatures are shown in Figure 4.9 and Figure 4.10.

Figure 4.13

In-plane TEM micrograph of the PLD-processed $SrTiO_3$ thin film #3666.

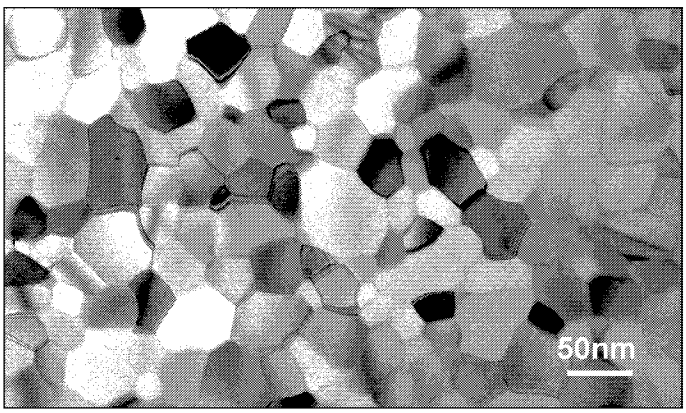

Figure 4.13 shows a plane view TEM analysis of the textured $SrTiO_3$ film #3666. This micrograph nicely shows the habit and the size distribution of the needle-like columnar grains, which are single crystalline throughout the entire height. In comparison, the TEM study of #3667 (not shown here) revealed that the columns that can be seen in the SEM image are not always of a particular crystallographic orientation. For all samples (#3666 to #3668), the grain boundaries are crystallographically 'sharp' and there is no apparent porosity [27]. This series, with identical stoichiometry and comparable thickness, should therefore allow the influence of the inner interface density, namely grain boundaries to be studied.

4.4 Single Crystals and Nanocrystalline Ceramics

Of course, the primary reference for the measurements is a $SrTiO_3$ single crystal. These can be purchased from every major supplier of single crystals, as $SrTiO_3$ is a common substrate material for many applications of perovskite films in general and also for high-temperature superconductor growth. $SrTiO_3$ single crystals are mostly grown by the Verneuil method, the flame fusion of oxide powders to grow a single crystalline boule of the material [5]. Possible stresses in $SrTiO_3$ single crystal samples can change the high temperature conductivity behavior significantly. Therefore annealing the samples at very high temperatures to heal stresses and defects from polishing may be useful for 'conditioning' the material.

The conventional mixed-oxide route for the preparation of titanate ceramics, for instance $SrTiO_3$, starts with the solid state reaction of titania (TiO_2) and strontium carbonate, $SrCO_3$. A powder mixture of both materials is calcined for some hours at temperatures commonly between 1200 and 1400 °C to decompose the carbonate and lose CO_2 to the atmosphere. The $SrTiO_3$ phase is then formed by interdiffusion via several transitional phases ([28] and references therein). During calcination the particles aggregate and grow significantly so that before being consolidated to bulk ceramics via sintering calcined powders have to be milled again. This potentially causes contamination from the milling media such as unwanted doping. Even intensive milling can hardly reduce the particle size to more than 300 or 400 nm.

Finer powders are made today via wet-chemical preparation routes like hydrothermal or alkoxide synthesis. With these methods, particle sizes can be as small as 50 – 70 nm [29]. First attempts to prepare samples from these powders by sinter forging demonstrated the feasibility of synthesizing dense ceramics with grain sizes just about the feature size of CSD films, but the samples also exhibited second phases of up to 10 μm size of severe nonstoichiometry due to an unfovourable Sr : Ti ratio of the starting powder [30].

In recent years, a different method has been developed to synthesize $BaTiO_3$ powders of an unprecedentedly small particle size of about 10 nm by the microemulsion ([31]-[33] and cited references). The synthesis is based on a sol-gel-type hydrolysis of metal organic alkoxide precursors, which is limited to tiny water droplets of a water-in-oil microemulsion. These droplets build the nucleation centers for the nanosized $BaTiO_3$ particles and are therefore sometimes called 'nanoreactors'. The droplets form spontaneously, when water is dispersed in, e.g., cyclohexane by the addition of an appropriate amount of a surface-active agent. These so-

called 'surfactants' have both a hydrophilic and a lipophilic part, which reduce the interfacial tension between water and the oil and thus stabilize nanosized water droplets. The diameter of these 'micelles' can be controlled, besides other parameters, by the type of surfactants used and the temperature of the microemulsion. They are usually between 5 and 100 nm [31]. The advantage, besides an extremely small particle diameter, is the uniform shape of the particles and the very narrow distribution in particle size, which is nearly monodisperse. With this technique it was possible for the first time to prepare a powder with a particle size far below the mean grain size of thin films prepared by CSD.

Nanosized powders tend to agglomerate and start sintering below 600 °C because of the extremely high specific surface [33]. In this case, for the particle size of ~ 10 nm, the surface area was determined by physisorption (BET) as 117.3 m^2/g [34]. It is therefore difficult to remove the residual organics after synthesis, which normally necessitates temperatures of 600 or 700 °C. For the samples studied in this work, the organics were burned out at 700 °C for 1 hour. Due to this, a coarsening of the particles was unavoidable. The synthesis of nanocrystalline titanate powders is an emerging field and at the time of writing many ideas are being pursued to improve their characteristics and widen the spectrum of material systems. (For this work, only $BaTiO_3$ powder was available in sufficient amounts.) In addition, various parameter combinations are established for preparing nanocrystalline ceramics.

The preparation of green bodies is very similar to that of conventional ceramic processing. The nanocrystalline $BaTiO_3$ powder was pressed into pellets (if necessary with the use of an organic binder to improve mechanical stability) and compressed further by cold isostatic pressing (CIP) under a pressure of up to 5500 bar. The green bodies prepared in this way had a density of between 50 and 55 % of the theoretical value.

The best results for the final nanocrystalline ceramic were obtained by pressure-assisted sintering. However, it seems to be necessary to keep the sintering temperatures and times as low as possible. One of the simplest methods is probably sinter forging by uniaxial pressing, which is schematically depicted in Figure 4.14a. The sample is placed between two pistons, of which one is hydraulically driven (the setup used in this work was an FCT 8210). The forces applied can be as high as 100 kN, but evidently the effective pressures depend on the actual sample diameter. To improve the pressure distribution within the sample, a surrounding matrix giving back-pressure is very useful. The sample can be processed in vacuum or under different gases / partial pressures and at temperatures above 1000 °C.

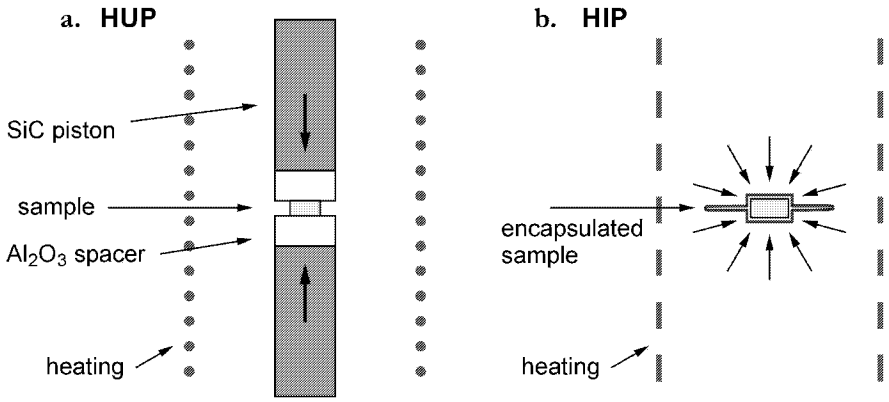

Figure 4.14

Basic principles of
a. *hot uniaxial pressing (HUP) and*
b. *hot isostatic pressing (HIP).*

Figure 4.15 illustrates the morphology of a hot uniaxially pressed $BaTiO_3$ ceramic. The sample was sintered at a temperature of 1000 °C for 30 minutes. The force applied was 20 kN on a cross-sectional area of about 100 mm^2, corresponding to a pressure of roughly 2000 bar. The picture shows a fracture surface about 2 mm from the sample's margin. As can be seen, the sample has a grain size of approximately 100 nm and the residual porosity is estimated to be ~ 10 %. This is mainly attributed to the inhomogeneous radial pressure distribution due to the lack of a die during sintering yielding back-pressure. Therefore it can be assumed that the middle of the sample exhibits a higher density and probably smaller grains.

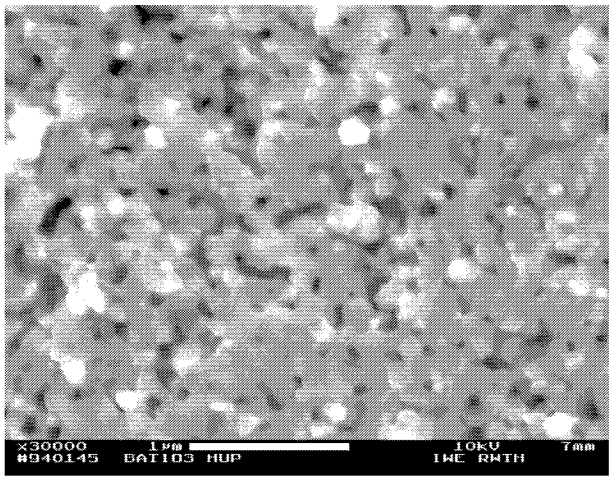

Figure 4.15

SEM picture of a nanocrystalline $BaTiO_3$ ceramic made by hot uniaxial pressing. The pressure of 2000 bar was applied at the sintering temperature of 1000 °C for 30 minutes. The grain size is about 100 nm. This picture was taken at the margin of the sample, showing residual porosity.

The method of choice is clearly hot isostatic pressing (HIP, depicted in Figure 4.14b), where the above mentioned inhomogeneities cannot occur. The isostatic pressure is exerted via a surrounding gas medium, which is usually an inert gas like argon. In this way pressures up to 3500 bar and temperatures up to 2000 °C can be realized (e.g. National Forge as used here). This technique is commonly used to compress already synthesized materials to their theoretical density, but this works only if the samples do not exhibit residual open porosity.

To sinter a green body with a porosity of 40 or 50 %, the sample is first freed from any organic residues like surfactants or binders and is then enclosed in an appropriate capsule. The material and the form of this capsule is crucial for the densification process as well as the final morphology and the structure of the ceramic and therefore several requirements have to be met. First of all, the material must offer adequate ductility to transfer the pressure on the powder and must be able to shrink sufficiently to obtain a sample density of 100 % at best. If the capsule is too stiff, it absorbs all the pressure. Excellent choices are metals, especially noble metals like gold or platinum, though expensive, with a wall thickness of 0.25 or 0.5 mm. Silver and copper are even softer, but their potential oxidation (resulting in possible reduction of the sample) can be problematic. Duran (Schott) or Pyrex (Corning) glass is also worth thinking about, because it is easy to handle and becomes sufficiently soft above ~ 700 °C. The disadvantage is its fragility at temperatures below this because of its negligible ductility. That means the sample must be heated up first without load and be kept at the final temperature level for a considerable length of time to build up the maximum pressure. Both heating up without any pressure and long annealing times promote an unfavorable grain growth. Additionally, the sample also has to be enclosed in platinum to inhibit unwanted contamination by the glass capsule.

The capabilities of hot isostatic pressing are demonstrated in Figure 4.16. A load of 2000 bar was applied before sintering at 860 °C for 30 minutes. In some parts, the grain size is as low as 35 nm. Unfortunately, the sample was severely reduced by the copper capsule used here and was therefore useless for further electrical investigations.

Figure 4.16

SEM picture of a dense nanocrystalline $BaTiO_3$ ceramic made by HIP.

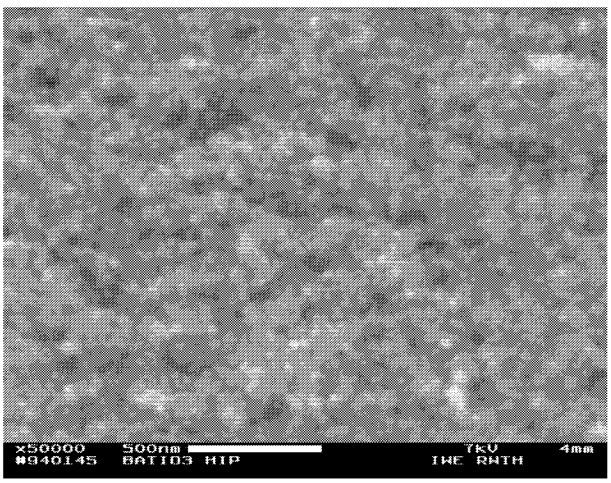

4.5 Sample Overview

Table 4.17 gives a brief overview of the samples presented in this work and summarizes their structural and morphological properties as well as doping concentrations.

Table 4.17

Sample overview. For more details see also text.

	material / doping	morphology / structure	remarks
Chemical Solution Deposition (on sapphire $(1\bar{1}02)$)			
ST_HTL01	$SrTi_{1.005}O_3$	columnar, polycryst.	~ 500 nm thick
ST_HTL04	$SrTiO_3$ / 2 at.% La	"	"
ST_HTL09	$SrTiO_3$ / 6 at.% Mn	"	"
ST_HTL12	$SrTiO_3$ / 2 at.% Fe	"	"
STO5	"	"	"
STMO6	$SrTiO_3$ / 0.7 at.% Mn	"	"
101100-E	$Ba_{0.7}Sr_{0.3}TiO_3$	"	"
210600-A	$BaTiO_3$	"	"
210600-F	$SrTiO_3$ / 1.5 at.% Mn	"	"
210600-G	$SrTiO_3$ / 3 at.% Mn	"	"
040302-B	$BaTi_{0.8}Zr_{0.2}O_3$	"	"
040302-C	$BaTi_{0.5}Zr_{0.5}O_3$	"	"
040302-D	$BaZrO_3$	"	"
Pulsed Laser Deposition (on MgO (100))			
#3461	$SrTiO_3$	heteroepitaxial	thickness ~ 1 µm
#3462	"	"	"
#3666	"	columnar, textured	"
#3667	"	fine grained, poly.	"
#3668	"	coarse grained, poly.	"
#3946	"	heteroepitaxial	thickness ~ 250 nm
#3950	"	"	thickness ~ 3 µm
Single Crystals			
CrysTec	$SrTiO_3$	single crystalline	substrate wafer
Litzenberger	$SrTiO_3$	"	major impurity Mn < 800 ppm
Nanocrystalline ceramics			
HUP	$BaTiO_3$	grain size ~ 100 nm	residual porosity
HIP	$BaTiO_3$	grain size ~ 50 nm	dense, severely red.

References

[1] www.mticrystal.com

[2] www.escete.com

[3] D. Duppalapudi, E. Iliopoulos, S.N. Basu, T.D. Moustakas, "Epitaxial growth of gallium nitride thin films on A-plane sapphire by molecular beam epitaxy", *J. Appl. Phys.* **85**, 3582 (1999)

[4] www.mkt-intl.com/sapphires

[5] www.mateck.de

[6] Ch. Tragut, "Kinetik schneller Sauerstoffsensoren", PhD thesis, Universität Karlsruhe, Fortschrittberichte VDI, Reihe 8, Nr. 291, Düsseldorf, 1992.

[7] S. Hoffmann, "Modifizierte Erdalkalititanat-Dünnschichten für integrierte Bauelemente: Morphologie, dielektrische Eigenschaften und Ladungstransportmechanismen", PhD thesis, RWTH Aachen, Fortschrittberichte VDI, Reihe 9, Nr. 288, Düsseldorf, 1998.

[8] U. Hasenkox, S. Hoffmann and R. Waser, "Influence of Precursor Chemistry on the Formation of $MTiO_3$ (M=Ba, Sr) Ceramic Thin Films", *J. Sol-Gel Sci. Tech.* **12**, 67 (1998).

[9] B.C. Bradley, R.C. Mehrotra and D.P. Gaur, *Metal Alkoxides*, Academic Press, London, 1978.

[10] Unpublished results. Based on a LA-ICP-MS (laser ablation inductively coupled plasma mass spectrometry) impurity analysis by C. Pickhardt, ZCH, Research Centre Jülich, 2002. See also R. Liedtke, "Herstellung, Charakterisierung und Bauelementsimulation von integrierten, elektrokeramischen Dünnschichtkondensatoren", PhD thesis, RWTH Aachen, to be published.

[11] G. Krüger, "Optische Charakterisierung akzeptordotierer Strontiumtitanat-Dünnschichten", diploma thesis, RWTH Aachen, 1999.

[12] C.L. Jia, K. Urban, S. Hoffmann and R. Waser, "Microstructure of Columnar-Grained $SrTiO_3$ and $BaTiO_3$ Thin Films Prepared by Chemical Solution Deposition", *J. Mat. Res.* **13**, 2206 (1998).

[13] D.F.K. Hennings, Ch. Metzmacher and B.S. Schreinemacher, "Defect Chemistry and Microstructure of Hydrothermal Barium Titanate", *J. Am. Ceram. Soc.* **84**, 179 (2001).

[14] Joint Committee for Powder Diffraction Standards (#35-734). International Centre for Diffraction Data, www.icdd.com.

[15] Ch. Ohly, S. Hoffmann, K. Szot and R. Waser, "High Temperature Conductivity Behavior of Doped $SrTiO_3$ Thin Films", *Integr. Ferroelectr.* 33, 363 (2001).

[16] K. Szot and W. Speier, "Surfaces of reduced and oxidized $SrTiO_3$ from atomic force microscopy", *Phys. Rev. B* **60**, 5909 (1999).

[17] D.B. Chrisey and G.K. Hubler, editors, *Pulsed Laser Deposition of Thin Films*, Wiley, New York, 1994.

[18] B. Stritzker, J. Schubert, U. Poppe, W. Zander, U. Krüger, A. Lubig and Ch. Buchal, "Comparison of YBCO-films prepared by laser ablation and sputtering", *J. Less-Common Met.* **164-165**, 279 (1990).

[19] L. Beckers, "Herstellung und Charakterisierung epitaktischer ferroelektrischer Schichten für optische Anwendungen", PhD thesis, Berichte des Forschungszentrums Jülich, Jül-3554, 1998.

[20] A. Eckau, "Optische und elektrooptische Eigenschaften von $BaTiO_3$-Dünnschichtwellenleitern", PhD thesis, Berichte des Forschungszentrums Jülich, Jül-3855, 2001.

[21] M. Siegert, "Wachstumsuntersuchungen an Bariumtitanat-Dünnschichten, hergestellt mit gepulster Laserdeposition", PhD thesis, Berichte des Forschungszentrums Jülich, Jül-3898, 2001.

[22] L. Beckers, J. Schubert, W. Zander, J. Ziesmann, A. Eckau, P. Leinenbach and Ch. Buchal, "Structural and optical characterization of epitaxial waveguiding $BaTiO_3$ thin films on MgO", *J. Appl. Phys.* **83**, 3305 (1998).

[23] L.R. Doolittle, "Algorithms for the rapid simulation of Rutherford backscattering spectra", *Nucl. Instr. Meth.* **B9**, 344 (1985).

[24] J. Schubert, ISG2, Research Centre Jülich, personal communication.

[25] W.K. Chu, J.W. Mayer and M.A. Nicolet, *Backscattering Spectrometry*, Academic Press, New York, 1978.

[26] J.W. Mayer and E. Rimini, editors, *Materials Analysis by Ion Channeling*, Academic Press, New York, 1982.

[27] Unpublished results. TEM analysis by C.L. Jia and Y. Ding, IFF (IMF), Research Centre Jülich, 2002.

[28] D.F.K. Hennings, B.S. Schreinemacher and H. Schreinemacher, "Solid-State Preparation of $BaTiO_3$-Based Dielectrics Using Ultrafine Raw Materials", *J. Am. Ceram. Soc.* **84**, 2777 (2001).

[29] Alfa Aesar, #41633 and #41634, www.alfa.com.

[30] unpublished results.

[31] Ch. Beck, W. Härtl and R. Hempelmann, "Size-controlled synthesis of nanocrystalline $BaTiO_3$ by a sol-gel type hydrolysis in microemulsion-provided nanoreactors", *J. Mat. Res.* **13**, 3174 (1998).

[32] J. Wang, J. Fang, S.-C. Ng, L.-M. Gan, C.-W. Chew, X. Wang and Z. Shen, "Ultrafine Barium Titanate Powders via Microemulsion Processing Routes", *J. Am. Ceram. Soc.* **82**, 873 (1999).

[33] Ch. Pithan, personal communication.

[34] Ch. Pithan, R. Waser, F.-H. Haegel and J. Dornseiffer, "Nanocrystalline $BaTiO_3$-ceramics prepared via microemulsion synthesis", International Joint Conference on the Applications of Ferroelectrics IFFF, Nara 2002.

5 Experimental Procedures

The main objective of this work is the determination of the electrical conductivity of alkaline earth titanate thin films and its interrelationship to the nonstoichiometry in the oxygen sublattice. As described above, at temperatures between approximately 500 and 1000 °C, the defect chemistry of titanates, and thus also their electrical properties, are dominated by the exchange of oxygen between the material and the ambient atmosphere. In order to obtain a comprehensive picture, a wide and continuous range of temperatures and partial pressures has to be studied. Another problem is the high actual resistance of thin films, which is due to the thickness and reach the G Ω regime even at higher temperatures.

These requirements make high demands on the experimental side. In this chapter, the techniques utilized for the measurements and the actual design of the setup will be elucidated in detail. The first part explains the concept of controlling the ambient oxygen partial pressure via an electrolytic oxygen pump made of stabilized zirconia, adapted from a setup originally intended measurements on single crystals and bulk ceramics. This technique is rarely encountered because of its technical difficulties but offers some distinct advantages compared to other more common methods. The second part of this chapter is dedicated to the description of several improvements that were introduced over time to meet the specific requirements of thin films and make the electrical measurements reliable. The final sections will cover the actual assembly and the preparation and contacting of the samples as well as a description of the measurement procedure.

Finally, the experimental setup combined with the 4-point dc measuring technique represents a facility for performing extensive and reliable investigations on titanate thin films.

5.1 The Measurement Setup

The measurement setup is illustrated schematically in Figure 5.1. The original construction is based on a layout by K. Beetz, who demonstrated the functionality of a closed oxygen pump using a solid state electrolyte [1]. The tube furnace itself is a quite simple construction and is controlled by a programmable Eurotherm controller. Its thermal isolation is not as good as that

of a muffle-type furnace so that the axial temperature distribution along the tube decreases towards the end flanges. (These flanges are water-cooled due to the fact that the oxygen pump and the sample holder contain several Viton O-rings or sealings with adhesives suitable for vacuum conditions and the use of organic components or a fixed bonding of materials with unlike thermal behavior does not tolerate temperature differences of some hundred K).

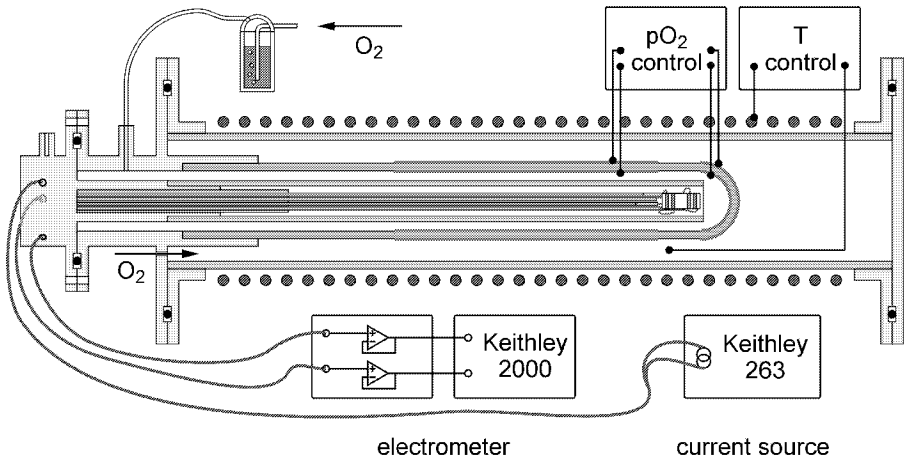

Figure 5.1

Schematic picture of the measurement setup (not to scale). The individual parts are described in the text.

The circumstance of thermal inhomogeneity along the furnace tube was deliberately used to gain information on the thermopower in the samples (due to the Seebeck effect) and finally the sample was positioned slightly off center in the furnace, where there was a slight gradient of approximately 2 K/mm. The furnace temperature was controlled by a thermocouple placed at the position of the sample outside the zirconia tube. Because the design of the sample holder did not permit an additional thermocouple to meter the temperature directly at the sample, the temperature can vary by 10 to 20 K.

5.2 Control of the Oxygen Partial Pressure (pO_2)

There are several basically different ways of controlling the oxygen activity in an atmosphere. The decision on which method is most appropriate depends on the measuring requirements. In this study, where the conductivity and the defect chemistry is to be investigated as a function of the oxygen nonstoichiometry, the primary prerequisite is a wide and continuous range of controllable oxygen partial pressures. As described above in detail, the temperature regime in which the variation of the oxygen sublattice is the dominant effect ranges from 500 °C to 1000 °C and in order to obtain both reducing and oxidizing conditions, the partial pressures should be variable from pure oxygen (1 bar) down to activities of less than 10^{-20} bar.

Figure 5.2 shows which regimes (pO_2 vs. T) are covered by the different methods. The easiest approach would be to flush the sample room with pure oxygen and then to evacuate it to the desired pressure. However, the lower pO_2 limit is somewhere between 10^{-5} bar and 10^{-10} bar, depending on the quality of the vacuum system. Despite this, the control and reliable monitoring of different pO_2 values remains questionable. Additionally, the tracking of impurities becomes relevant. Another still very common method makes use of readily available Ar/O_2 mixtures with varying oxygen content. The argon acts as a carrier gas (so that an open system can be built) and the oxygen concentrations can be well defined to a few ppm, but the same control problem results. Inherent in both methods is that they are limited to oxidizing ambients.

Figure 5.2

pO_2 regimes accessible by different gas mixtures and the electrolytic cell.

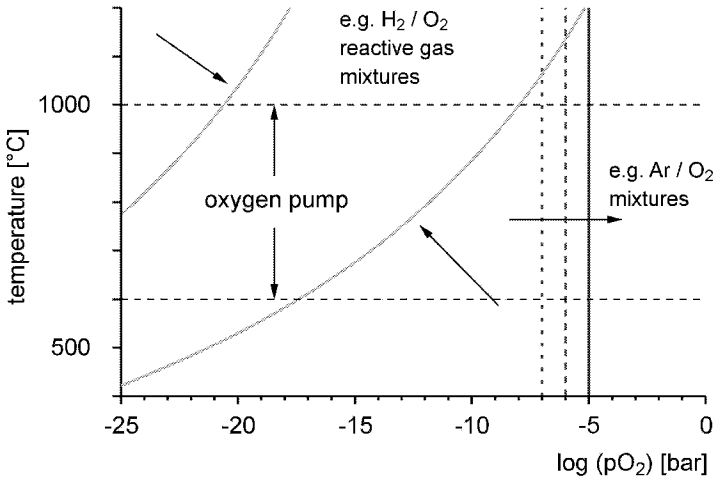

To get lower (reducing) partial pressures, the oxygen must be buffered by a reaction with another chemical component. This can be a metal like nickel or titanium, which establish fixed oxygen activities in the gas phase. These equilibrium reactions follow an exponential thermal activation. A much more flexible control of the pO_2 is maintained by the mixture of a reactive gas like CO or H_2. Let us consider the reaction of hydrogen with oxygen to water (these are always present to some extent and this fact will later be deliberately used to improve the control characteristics of the pump):

$$H_2 + \tfrac{1}{2}O_2 \rightleftarrows H_2O. \tag{5.1}$$

In the thermodynamic equilibrium, the corresponding law of mass action gives:

$$pH_2 \cdot (pO_2)^{1/2} = k_{H_2O}(T) \cdot pH_2O. \tag{5.2}$$

with

$$k_{H_2O}(T) = k_{H_2O} \cdot e^{-E_A/k_B T} . \tag{5.3}$$

Here, pH_2 and pH_2O represent the hydrogen and water vapor partial pressures, respectively, and k_{H_2O} the reaction constant. k_B is the Boltzmann constant.

When in equilibrium, the partial pressures of hydrogen, oxygen and the water vapor are in a certain proportion. k_{H_2O} is the reaction constant specific for this reaction like the activation energy E_A. The actual value can be found in tables like [2]. This (exemplary) reaction offers two freely variable parameters, namely pH_2 and pH_2O. It should be emphasized that only by such equilibrium reactions can the pO_2 be reduced to extremely low values. The oxygen partial pressure is of course described more precisely now as an "activity" quantity with statistical meaning. (It should be mentioned at this point that virtually in every vacuum system such buffering gases exist as impurities, so one always has to keep an eye on the associated equilibrium reactions). As can be seen in Figure 5.2, the range of partial pressures that can be achieved is still restricted.

The substantial disadvantage of these methods lies in the difficulty, if not impossibility, of controlling intermediate values. Not until temperatures of about 1000 °C are reached do the regimes covered by these methods overlap. Because the defined temperature range is below this level, these methods do not fulfill the requirement of a continuous partial pressure range mentioned above. Therefore, a fundamentally different technique has to be applied. For several decades the use of solid state electrolytes has been a standard tool for measuring oxygen partial pressures [3][4][5]. The most familiar application is the λ-sensor. This unit monitors the oxygen content of combustion engine exhausts to optimize the combustion reaction. This technique has been adopted to design an 'oxygen pump' [1]. Because of its outstanding versatility, it was also the preferred option for this work and will now be introduced in detail.

The assembly of this oxygen pump, which is sometimes also called an electrolytic or amperometric cell, is shown in Figure 5.3. The body consists of a ceramic tube closed at one end, which is made of yttria stabilized zirconia ('YSZ') that is utilized because of its superb oxygen ion conductivity [6]. The stabilization is inevitable, due to the different modifications pure ZrO_2 takes on at different temperatures. The most severe phase transformation between monoclinic and tetragonal occurs at approximately 1170 °C where the transformation is accompanied by a volume change of about 8 %, which explains why ceramic components of pure zirconia cannot

Figure 5.3

Schematic picture of the oxygen pump assembly.

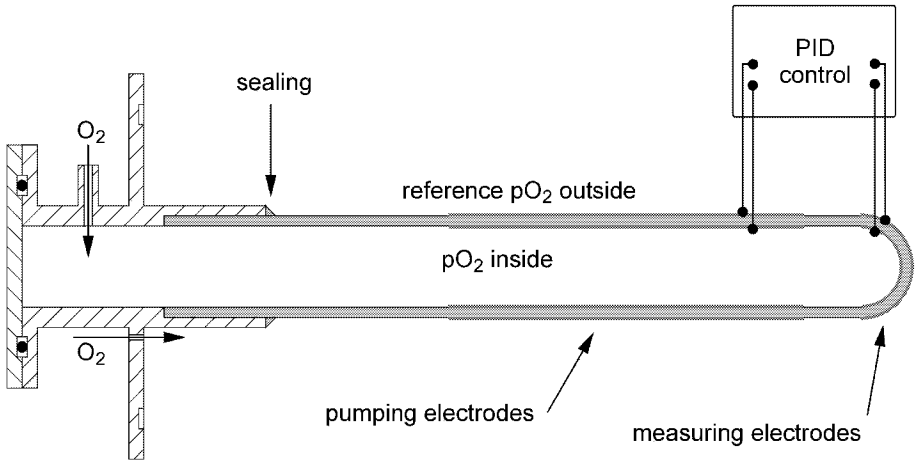

be made. The addition of elements like Ca or Y in the form of oxides not only stabilizes the high temperature phase but also introduces oxygen vacancies as charge compensation. In this way tubes of different sizes can be manufactured, exhibiting excellent electrolytic properties.

To use such an electrolytic oxygen ion conductor for the determination (and later the control) of oxygen partial pressures, porous electrodes are applied on both sides of the tube. The tube separates two regions with different oxygen concentrations, of which one serves as the reference atmosphere. In this design, a constant flow of oxygen is applied around the tube (1 bar) and the interior is the sample chamber with variable oxygen partial pressure. The porosity of the electrodes is essential for an oxygen exchange with the atmosphere, as shown schematically in Figure 5.4:

Figure 5.4

Triple phase boundaries.

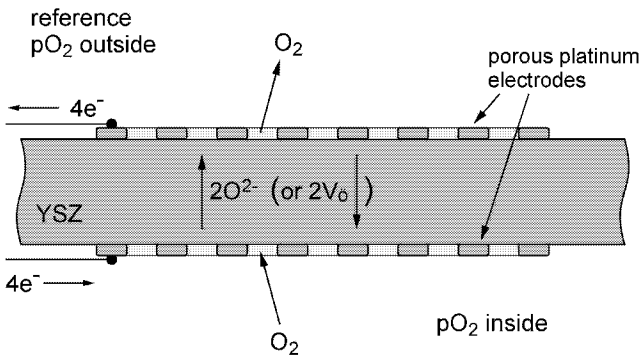

At the triple point between the atmosphere, the electrode metal and the electrolyte, an adsorbed O_2 molecule is dissociated into two single oxygen atoms that each take up two electrons from the electrode. The simplified dissociation reaction then reads:

$$O_2\,(\text{gas}) + 4e^-\,(\text{metal}) \rightleftharpoons 2O^{2-}\,(\text{electrolyte})\,. \tag{5.4}$$

This reaction can be converted into the corresponding electrochemical potentials, once a thermodynamic equilibrium has been established (for a detailed deduction see [1]). Due to the high ionic conductivity, the difference between the oxygen potentials of the two sides can be expressed directly by the electrostatic potential difference between the electrodes. This voltage is known as the Nernst voltage given by

$$U_N = \frac{k_B T}{4e} \cdot \ln\left(\frac{pO_2(\text{inside})}{pO_2(\text{outside})}\right), \tag{5.5}$$

with e being the unit charge. By measuring this voltage and exposing the outer electrode to a defined reference ambient, the oxygen activity inside the tube can be easily calculated. Using this effect in an inverse manner, by applying a voltage or a current, respectively, the oxygen is forced to move through the electrolyte, leaving behind an ambient with decreased oxygen content. Because of the underlying nature of this technique, i.e. the fact that the oxygen is directly acted on, the oxygen partial pressure can be controlled very sensitively and continuously over a wide range. This (compared to the other methods) great advantage makes the design of an oxygen pump with an electrolytic oxygen conductor presently the only tool available to vary oxygen atmospheres and temperatures independently and continuously in the desired range.

Such a construction is usually not operated above ambient pressure (1 bar). Besides the risk of fracture, the times to change the pO_2 would become immense because of the amount of oxygen that has to be transported. At mid range partial pressures, the amount of free oxygen is in the same order of magnitude as the residual, reactive gas impurities in the system. These depend crucially on the gas by means of which the chamber was flushed before the start of an experiment. In this region, the partial pressure reacts extremely sensitively to disturbances or leakages and control becomes equally difficult. A common problem is that the system runs into a resonant oscillation and the actual value is no longer defined. The reason is that the system operates at the transition point of a titration and the control points are too coarse. The most helpful tool is a PID controller (such as the Eurotherm 2408) with carefully adjusted parameters and a very good resolution. Some modern controllers offer an 'auto tune' to find the best parameters, which can be very useful. At lower partial pressures, the buffering properties of the reactive impurities in the chamber (introduced by flushing before the start of the experiment) become noticeable and controlling becomes easier again. The oxygen is no longer free but bound

to the buffer gas, as in the example in Equation (5.1). Experience has shown that conditions as low as 10^{-20} bar are easily maintained.

The second important parameter is the temperature. The lower operating limit is marked by the onset of sufficient oxygen ion diffusion somewhere between 600 and 650 °C. Below these temperatures, the diffusion is too slow to regulate the partial pressure within reasonable times. The maximum operating temperature is restricted by the stability of the electrodes. Under extremely reducing conditions (< 10^{-20} bar) and temperatures of about 1000 °C, the electrodes degenerate or sometimes even delaminate. Another complication is the residual electronic conductivity of YSZ. At temperatures higher than approximately 1100 °C, the electronic part can no longer be neglected so that Equation (5.5) is no longer valid in this form but has to rewritten.

The zirconia tube is approximately 300 mm long and has an inner diameter of nearly 16 mm. The pumping electrode is about 130 mm long and has a distance of about 25 mm to the measuring electrode on the top end of the tube. The electrodes themselves are multiple brush painted with a fritless platinum paste and contacted with insulated platinum wires [7]. The nature of this electrode, i.e. the porosity and cleanness, is very important for the speed of the pump. After firing to burn out solvents and other organic constituents of the paste, the electrodes were cleaned in hot nitric acid.

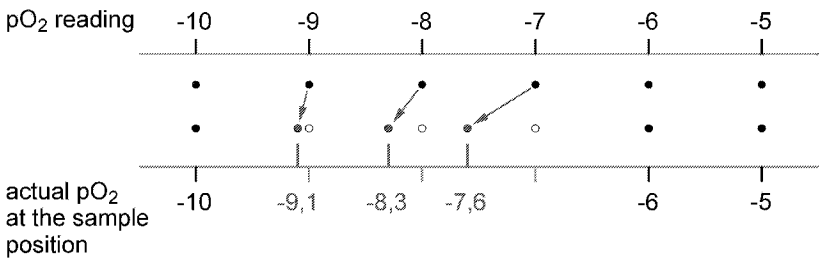

Figure 5.5

Deviations from the pO_2 reading and corrected values.

The spacing between the measuring and the pumping electrodes on either side of the tube plays an important role for the measurement and control of partial pressures. This geometry is somewhat susceptible to gradients in the mid range pO_2 regime. It was shown that in such cases the measuring electrode, which can of course also work as a sensor, always displayed **lower** pO_2 values than the measuring cell, depicted in Figure 5.5, and that the deviations depend crucially on the residual gas components. Due to this, the construction and the dimensions as well as the gas conditioning experienced some improvements over time. In its latest arrangement the sample is as near as possible to the sensing electrode. For this configuration, the actual partial pressures at the place of the sample were measured by a second, independent sensor. As specified, at 700 °C only a few values showed visible deviations.

5.3 Conductivity Determination on Thin Films

Electrical conductivity measurements of single crystals or bulk ceramics usually do not necessitate great effort and are carried out by use of the 4-point dc method [8][9]. Due to the dimensions of such samples, where cross sections are several mm^2, the actual resistances are barely higher than a few M Ω over the entire partial pressure range at temperatures of 700 °C and above. Because electrical disturbances commonly do not interfere significantly, the sample holder construction can be made to maximum mechanical stability and other requirements. The current and voltage leads can then be fed through supporting alumina capillary tube to overcome the temperature gradient to the sample because the leakage currents through the ceramic can be neglected.

In contrast to this, the thicknesses of thin films are normally between 500 nm and 1 µm, which is roughly three orders of magnitude smaller than that of ceramic samples or single crystals. As already mentioned in the last chapter, the conductivities of the substrates, which are still 0.5 mm and 1 mm thick, have to be many orders of magnitude smaller than that of the material of the film to compensate for this thickness ratio. As stated above, sapphire and MgO are excellent candidates, as will be demonstrated later. The absolute resistance of a thin film considered here, which is actually determined by the measurement, can become very high, sometimes as much as several G Ω. In this case, electrical disturbances by, for instance, a not perfectly compensated bifilar wiring of the heating coils or parasitic currents through the ceramic parts of the holder can easily affect and falsify the results. Due to such reasons, the precise determination of the electrical properties of thin films is technically quite demanding. The sample holder used here has to fulfill several requirements and its design was developed in a previous work [10]. In the present work some additional improvements were made and the more sophisticated layout is shown in Figure 5.6. The special capabilities are the full triaxial shielding of both the wiring and the sample itself as well as an insulation of the electrical wiring in the temperature zone.

The electrical connections consist of four individual platinum wires, each 0.5 mm in diameter. They are carried by thin-walled, high density alumina tubes (Ø 0.8/1.2 mm), which themselves are held by a four-bore alumina capillary tube [12]. The first two bores are reserved for the voltage leads to the two inner electrodes of the sample. The thin alumina tubes are platinized outside and are then contacted to the inner triaxial shield. This inner shield is set at the same potential as the actual lead so that the intrinsic resistivity of the tube does not matter and the tube is close to the sample. The sealing between the sample and the wire outside the furnace is

Figure 5.6

Drawing of the sample holder.

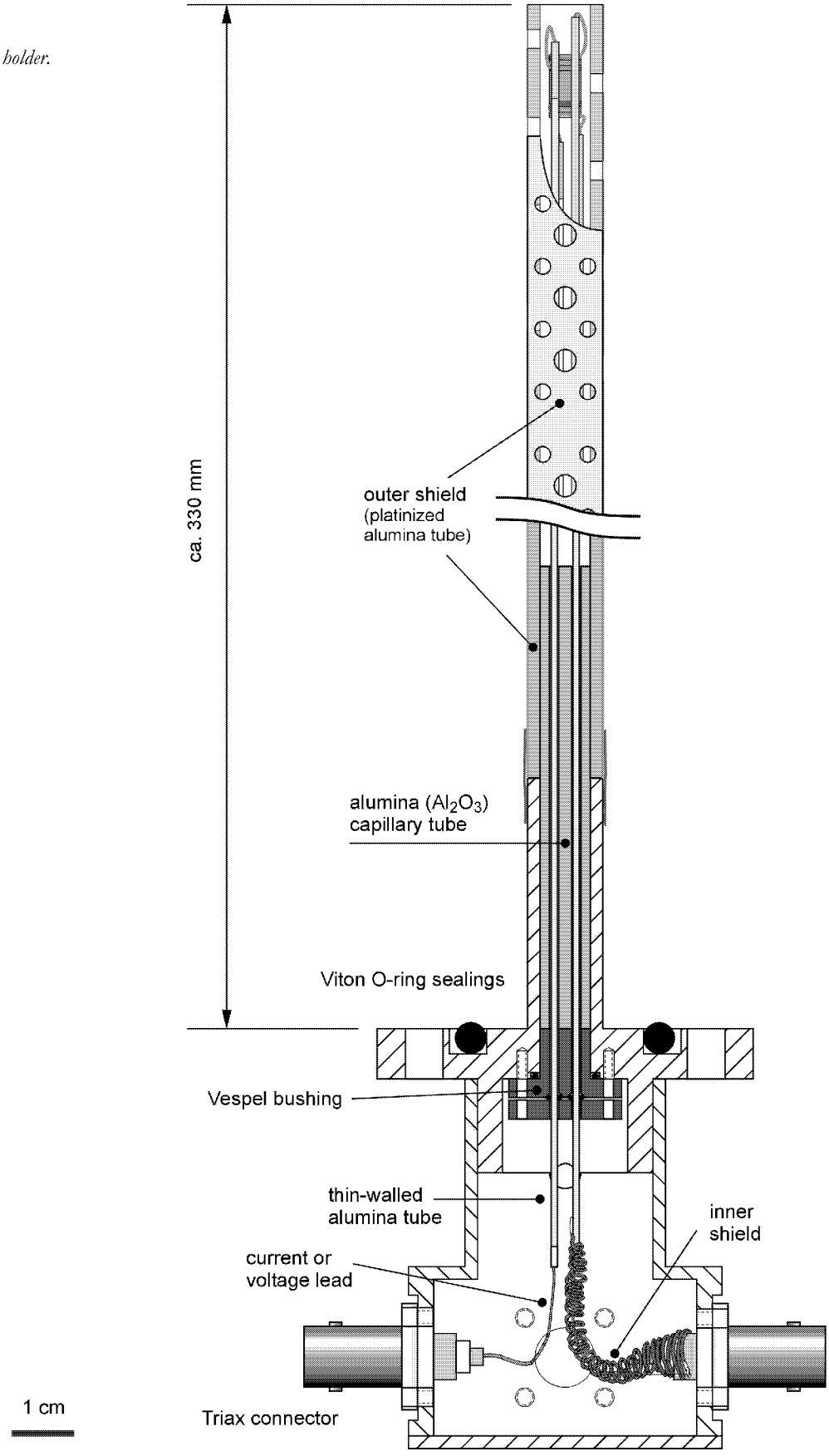

achieved by epoxy resin [11]. The sealing against the Vespel bushing is performed by miniature Viton O-rings. The third bore is used for the connection to the current source. Normally, the current is supplied and lead away coaxially, which could easily be realized by a metallization of the guiding tube, but the insufficient resistivity of alumina at the measurement temperatures from 700 up to 1000 °C does not allow the current to be conducted in this way. Instead of this, the current flows back from the sample through the fourth wire. This wire is then soldered to the platinization of the current input tube, which extends just behind the sealing for two reasons: the coaxial current guidance is restored and the last bore can serve as a gas inlet to flush the inside of the oxygen pump (i.e. the sample chamber). For the same reasons just described, also the capillary tube extends only a few centimeters into the oxygen pump. The stainless steel holder itself and an auxiliary alumina tube around the sample act as the outer shield, both of which are both connected to ground. In this tube more than 80 holes were drilled to maintain a good gas exchange inside the oxygen pump and especially around the sample. This construction is extremely fragile, but it allows for the first time the exact and reliable determination of resistances of at least 25 G Ω, as will be demonstrated later. Because of the desired flexibility and due to maintenance reasons, all parts can be easily taken apart and be replaced.

The connections to the metering and the sourcing instruments are realized by commercial triaxial plugs. The current supply is maintained by a Keithley Model 263 Calibrator/Source with an exceptionally fine resolution of 50 aA. In this way the current and voltage levels of the measurement can be kept low enough to not run the risk of altering the sample by electrical overload.

The voltage between the inner two electrodes must be metered with a high impedance input, which is not provided by conventional digital multimeters. This is the domain of an electrometer, but a circuit integrating a high-impedance operational amplifier meets all needs, too (Figure 5.7).

Figure 5.7

Electrometer circuitry by using the operational amplifier AD 549L [13].

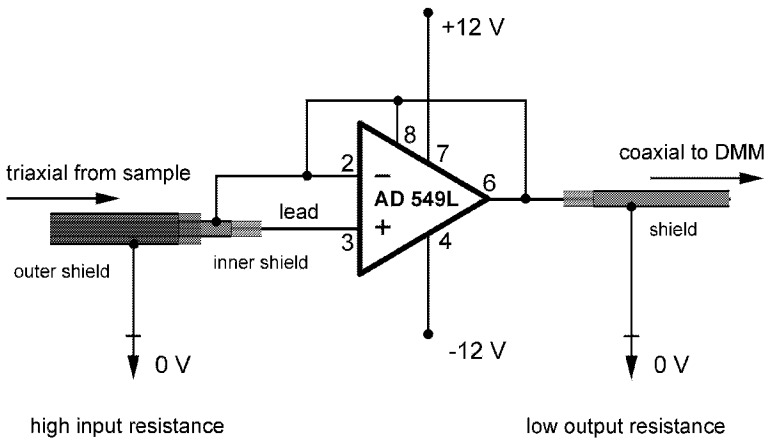

With this well-established four-probe measurement technique, the conductivity σ is calculated by:

$$\sigma = \frac{I}{U} \cdot \frac{l}{b\,d} \quad . \tag{5.6}$$

I denotes the current applied to the outer electrodes, U the measured voltage drop over the two inner electrodes, which are separated by the distance l. b is the width of the sample and d the thickness of the crystal or the thin film, respectively. Of course, the accuracy of σ is limited by how precisely these geometrical quantities are known.

5.4 Sample Preparation and Measurement Procedure

In order to perform electrical measurements under varying atmospheric and temperature conditions, suitable electric contacts must be applied onto the sample. First of all, the samples are cut into pieces of 5×10 or 5×15 mm^2, depending on the initial size of the substrate that has been coated. In the case of CSD processing, preferably round sapphire substrates of 2 inches in diameter were used. When the films were deposited by laser ablation, the sample size was restricted to 10×10 mm^2 due to the given geometry of the heating chuck of the PLD setup. The final geometry of a sample with its 4 electrodes is depicted in Figure 5.8.

Figure 5.8

Actual sample geometries. Grey areas are the sputtered platinum electrodes.

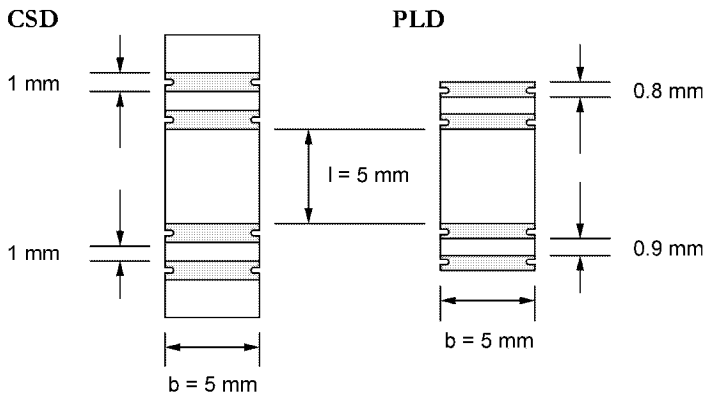

To make good and reliable electrical contacts with equal conditions for each measurement (mainly an identical geometry), the electrodes are made of platinum, a frequently used electrode material due to its stability against oxidation and temperature effects. They are applied by means of sputtering and utilization of a laser-cut shadow mask. The connections to the current leads or voltage readings are realized by 0.25 mm platinum wires that are fixed to the sputtered platinum electrode by platinum paste. To hold them in place, 8 notches are cut with a diamond-coated

wire saw and after tightening the platinum wires and firing the paste, mechanically strong connections with low contact resistances are obtained. It appeared that the sputtered platinum tend to form little droplets due to surface tension and thus leading to an undefined contact geometry. This depends on the thickness of the electrode, normally about 100 nm, and primarily on the measurement temperature (usually above 900 °C). This effect can be sufficiently reduced by covering the whole sputtered area with platinum paste.

The wires are then connected by thermo-bonding (Unitek Unibond) to the 0.5 mm thick platinum leads. Because of the different diameters and the settings of the bonder, the two wires are not welded but can be detached without damage to the lead wire, which therefore can be used repeatedly. Nevertheless, a prolonged use leads to deterioration of the lead wire deteriorate and finally to rupture. When the sample is attached to the leads, proper care has to be taken to avoid any interconnect. The outer shielding is governed by a platinized alumina tube of 8 mm inside diameter and because of this extremely limited space, it takes considerable time to mount and adjust a sample with enough clearance and to prevent it from sagging.

After attaching the shielding tube and assembling the sample holder to the oxygen pump, the chamber is flushed with oxygen (quality 4.8) to achieve well-defined starting conditions. The oxygen is sometimes moistened, which is achieved by feeding it through water-filled bubblers with special frits. These frits are made by sintering tiny glass globules, which gives a very small pore size and thus comparatively small bubbles. The water take-up by the oxygen is the greater the higher the specific surface of the bubbles is. It can take many hours to remove all unwanted residues from the sample chamber, because of an unavoidable dead volume (which can be water molecules in the case it is necessary to run the experiment with dry oxygen). This flushing usually lasts for the whole heating period.

When the final measurement temperature is reached, the flushing oxygen is disconnected. However, it then takes some time for the sample inside to take on a stationary state. Once the reading is constant, a 'zero reading' is taken. This is the voltage drop between the two inner electrodes without an applied current which represents the thermopower due to the Seebeck effect. After starting coming from low values, of course) to such a magnitude that the voltage drop is below 100 or 200 mV at maximum. After checking the reverse poling, the next pO_2 value is set.

A typical measurement takes 9 – 12 hours, mainly depending on the measurement temperature. The measurement cycle of the nanocrystalline ceramic takes even longer (~ 18 hours), most likely due to the larger thickness of the sample compared to thin films.

References

[1] K. Beetz, "Die geschlossene Festelektrolyt-Sauerstoffpumpe", PhD thesis, Universität Karlruhe, Fortschrittberichte VDI, Reihe 8, Nr. 358, Düsseldorf, 1993.

[2] Landoldt-Börnstein

[3] J. Fouletier, H. Seinera and M. Kleitz, "Measurement and regulation of oxygen content in selected gases using solid electrolyte cells. I. Discontinuous use of gauges", *J. Appl. Electrochem.* **4**, 305 (1974).

[4] J. Fouletier, H. Seinera and M. Kleitz, "Measurement and regulation of oxygen content in selected gases using solid electrolyte cells. II. Differential gauge", *J. Appl. Electrochem.* **5**, 177 (1975).

[5] J. Fouletier, H. Seinera and M. Kleitz, "Measurement and regulation of oxygen content in selected gases using solid electrolyte cells. III. Oxygen pump-gauge", *J. Appl. Electrochem.* **5**, 111 (1975).

[6] The tubes used in this work were made by Zircoa, USA. Other suppliers are Viking, Denmark, or Vesuvius McDanel, www.techceramics.com.

[7] Electro Science Lab, Platinum Paste #5542, www.electroscience.com.

[8] Ch. Tragut, "Kinetik schneller Sauerstoffsensoren", PhD thesis, Universität Karlsruhe, Fortschrittberichte VDI, Reihe 8, Nr. 291, Düsseldorf, 1992.

[9] W. Menesklou, "Optimierung des Ansprechverhaltens resistiver Sauerstoffsensoren", diploma thesis, Universität Karlsruhe, 1991.

[10] Ch. Ohly, "Untersuchungen zur Hochtemperatur-Leitfähigkeit in dotierten Erdalkalititanat-Dünnschichten", diploma thesis, RWTH Aachen, 2000.

[11] Varian TorrSeal, www.varian.com

[12] Friatec GmbH, Germany, Degussit Al23

[13] Analog Devices, Norwood, www.analog.com

[14] K. Szot, personal communication.

6 Electrical Conductivity Behavior under Changing Oxygen Ambients

In this chapter, the electrical high-temperature conduction behavior of strontium titanate thin films as a function of the oxygen partial pressure of the surrounding atmosphere will be presented.

After briefly summarizing the experimental limitations of the measurement setup and the contributions of the substrate materials, the conductivity characteristics of a single crystalline $SrTiO_3$ sample will be thoroughly explained. The results are discussed with respect to the suitability and reliability of the setup and are taken as a reference for the following measurements.

The third section deals in depth with the conduction behavior of polycrystalline thin films. Starting with nanocrystalline $SrTiO_3$ films prepared by CSD, the general characteristics will be compared to the well-known classical characteristics of the single crystal. After that, the effects of doping with acceptor (Mn) as well as donor-type elements (La) and the influences of an isovalent variation of the cation sublattice are shown. The latter aspect includes the solid solution series $Ba_{1-x}Sr_xTiO_3$ and $BaTi_{1-y}Zr_yO_3$.

The next section elucidates the consequences of altering of the interface density, which is accomplished by varying morphologies, i.e. different grain sizes, of PLD-derived polycrystalline thin films on MgO.

The following part discusses in detail the properties of heteroepitaxial $SrTiO_3$ thin films. To separate the influence of the surface itself and to find out more about the dimension where effects become apparent, a series of varying thicknesses was studied.

The final section portrays the conductivity characteristics of a nanocrystalline $BaTiO_3$ ceramic to fill the gap between single crystals and bulk ceramics studied in the past and the thin films with

feature sizes in the nanometer regime. For the first time, a ceramic sample was analyzed that exhibits a mean grain size of the same order of magnitude as is often present in polycrystalline thin films.

6.1 Experimental Limitations

The problem is that the measurement of thin film conductivity is a low-level measurement. The setup can, very approximately, be divided into three main resistances: the film, the substrate and the wiring/sample holder. The special difficulty is that the films are microscopically thin and can, intrinsically, exhibit extremely small conductivities. The precise determination of the thin film resistance demands, besides the precise control of the measurement parameters, that erratic currents through the sample holder or the substrate are preferably several orders smaller and can therefore be neglected.

As mentioned in the previous chapter, the sample holder was optimized as far as possible within the given geometrical and mechanical constraints to suppress parasitic currents through the holder. The resulting resistance, i.e. the resistance of an open circuit at measurement temperatures, was determined to be at least $2.5 \cdot 10^{10}\ \Omega$. Of central importance here is the cleanness of the ceramic components, primarily the Al_2O_3 tubes. Especially soldering additives appeared to be problematic.

It turned out in this work that the limiting factor regarding the precise determination of thin film conductivity is the intrinsic resistivity of the substrate material. As pointed out earlier, the actual resistance of the substrate (that is roughly a thousand times thicker than the film) has to be larger than that of the film. The substrate materials used here are sapphire (almost exclusively r-plane, $(1\bar{1}02)$) or MgO (100). Both materials are known for their highly insulating properties due to their large bandgap and thus lack electronic conduction at temperatures up to 1000 °C.

In Figure 6.1, an uncoated sapphire substrate blank was examined with respect to its conduction behavior against temperature and dependence on pO_2. To be on the safe side, this was controlled at a temperature of 1000 °C where an increasing electronic contribution to the conductivity is more pronounced. If the conductivity shows no significant dependence on the pO_2, it can therefore be assumed to be valid at lower temperatures, too, thus proving the material's suitability.

As expected, the absolute conductivity of sapphire is very low. Only under reducing conditions can a slight dependence on the oxygen partial pressure can be detected, which is neglected in the further discussion. To get a more visual comparison, because actually the resistance of the substrate competes with the resistance of the film, σ is normalized with respect to the thickness ratio:

$$\sigma_{norm} = \sigma_{meas} \cdot \frac{d_{substrate}}{d_{film}} \tag{6.1}$$

The sapphire substrates applied for CSD preparation were usually 430 µm thick, while the film thickness was generally 500 nm. This yields a normalization factor of 860. The values obtained in this way, also plotted in Figure 6.1 on the right, can now directly be compared to the thin film data.

Figure 6.1

Conductivity of an r-plane sapphire substrate as a function of temperature and oxygen partial pressure. The left vertical axis gives the actual value of σ for a 430 µm thick sample. The right axis denotes the conductivity, normalized with respect to a 500 nm thick CSD thin film according to Equation (6.1).

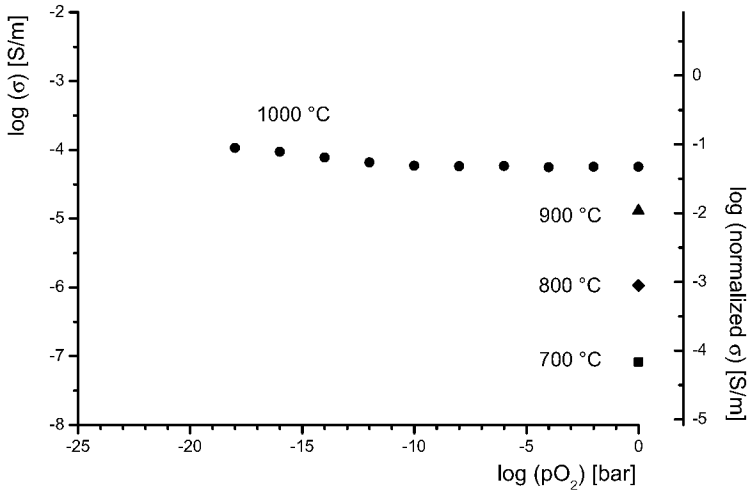

An analogous measurement on 1 mm thick MgO substrate (not shown here) resulted in similar values. In all the substrate measurements, the influence of the holder is included so that the 'substrate levels' are the actual limitations for the studies on thin films.

To summarize possible sources of experimental errors, the deviations in oxygen partial pressure control (see Section 5.2) are only noticeable at 700 °C and are quite small. The restrictions due to inaccurate temperature determination are estimated to lie within ± 20 K. This is because the sample holder did not allow a thermocouple to be installed, so that the latter had to be positioned outside the zirconia tube. The temperature gradient inside the furnace tube was determined from separate measurements without the oxygen pump. It can be assumed that the thermal gradient inside the oxygen pump might be smaller.

The errors induced by the electrical measurement system, i.e. the current source, the electrometer circuit and the voltage meter were tested and can be neglected. Finally, an error of 10 % has to be accounted for with respect to deviations from the sample's geometry that was used to calculate σ according to Equation (5.6). This stems mainly from the fact that the film thickness could only be determined from optical spectrometry, miscut during sample preparation and tolerances in the sputter deposition of the electrodes through a shadow mask.

As long as the measured resistance is considerably less than $\sim 10^{10}\,\Omega$, the erratic influence by the circuitry, the sample holder or the substrate can therefore be neglected and the measured data can be attributed to properties of the film alone.

6.2 $SrTiO_3$ Single Crystal

The electronic conduction characteristics of single crystalline strontium titanate have been reported by numerous groups and the data that can be found in literature are very uniform (see Chapter 3). Therefore, a $SrTiO_3$ single crystal was measured to prove the reliability of the setup, above all the solid state electrolyte oxygen pump, and to obtain a reference data set for the following investigations on thin films. The nominally undoped single crystal used here exhibited an impurity concentration of roughly $10^{18}/cm^3$, which was predominantly caused by Mn, resulting in a net acceptor-type doping [3][4]. The four-point dc measurement was performed at temperatures between 700 and 900 °C at intervals of 50 K and at oxygen partial pressures ranging from 1 bar to 10^{-20} bar, as displayed in the $\log(\sigma)$ - $\log(pO_2)$ - diagram of Figure 6.2.

The results demonstrate an excellent agreement with the published data as well as with defect chemical predictions. The main characteristics are the n-type conduction behavior under reducing conditions, the intrinsic minimum at mid-range pO_2 values and the p-type regime. In the n-type region, where σ is dominated by the generation of electrons due to the loss of oxygen to the ambient, the curve very closely follows the predicted slope of - ¼ in this double logarithmic plot. At higher temperatures (at 850 °C and especially at 900 °C) and extremely low partial pressures, a flattening of the - ¼ - slope can be seen. This leveling of the curve indicates the transition to the region with a slope of - 1/6, where the concentration of extrinsically generated oxygen vacancies exceeds that of intrinsic vacancies due to impurity compensation. In this regime, the defect chemical reactions are expressed by Equations (3.10), (3.13), (3.26) and (3.27), respectively.

Figure 6.2

Electrical conductivity of a $SrTiO_3$ single crystal as a function of temperature and oxygen partial pressure (measured in the YSZ oxygen pump).

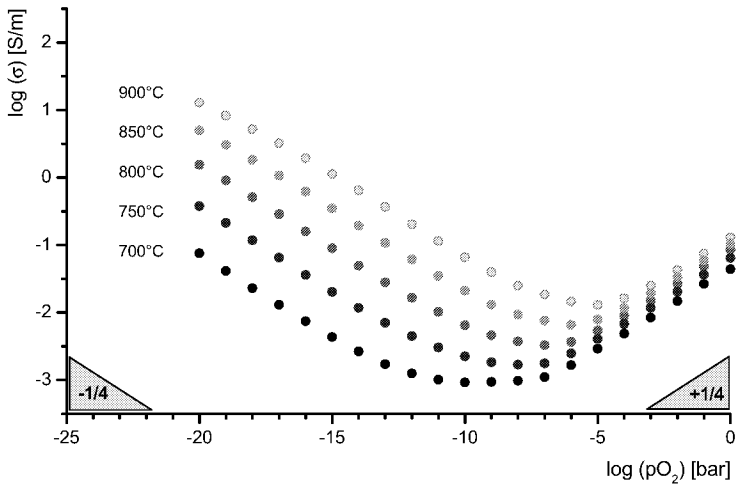

Moving from the conductivity minimum towards oxidizing atmospheres, the p-type region is entered and the conductivity increases with a slope of + ¼. This behavior resembles the gradual filling of the intrinsic vacancies, where electron holes become the dominant charge carriers. The linear parts of these electronic branches can be fitted and hence the electronic contribution to the conduction behavior can be derived. The fits, shown in Figure 6.3, deviate from the theoretically predicted ± ¼ - slope by less than 1 or 2 %, respectively. The deviations of the measured curve from the fit indicate the - $^1/_6$ - behavior at higher temperatures and reducing conditions as well as the contributions to σ by the diffusion of oxygen vacancies in the conductivity minimum.

Figure 6.3

Electronic fitting of the conductivity data from Figure 6.2. Deviations are due to intrinsic reduction (-$^1/_6$ regime) or ionic diffusion of oxygen (conductivity minimum).

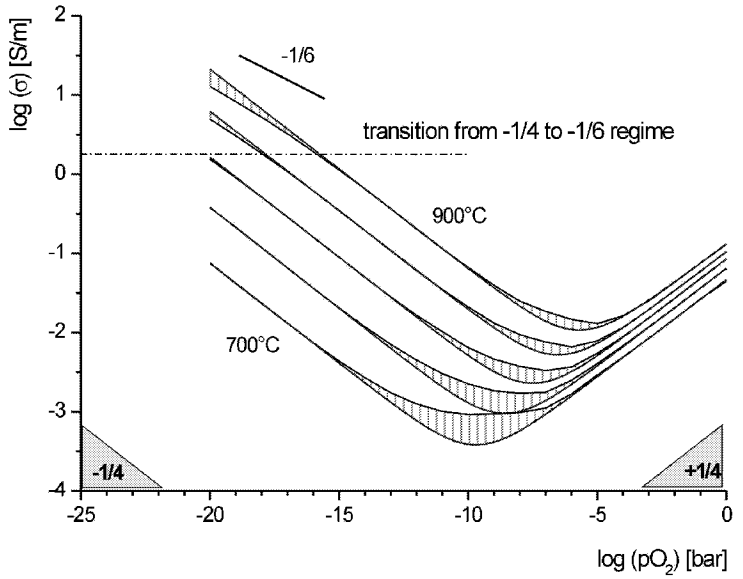

The determination of the electronic part of the conductivity allows a considerable amount of information on the electrical conduction properties of $SrTiO_3$ to be extracted:

In the electronic minimum of the conductivity, the charge carrier concentration resembles the intrinsic thermal generation of electrons and holes over the bandgap:

$$\text{nil} \rightleftarrows e' + h^{\bullet} . \tag{6.2}$$

The associated mass action relation reads

$$\begin{aligned} n \cdot p = K_i(T) &= K_{i,0} \cdot e^{-E_G(T)/k_B T} \\ &= N_C(T) \cdot N_V(T) \cdot e^{-E_G(T)/k_B T} \end{aligned} \tag{6.3}$$

with

$$E_G(T) = E_G(0K) - \beta_G \cdot T , \tag{6.4}$$

where β_G denotes the temperature coefficient, $K_{i,0}$ the mass action constant and $N_C(T)$ and $N_V(T)$ the density of states in the conduction or the valence band, respectively. Expressing $n \cdot p$ by the minimum electronic conductivity value, one obtains

$$\sigma_{el,min} = 2e\left(N_C(T)\,\mu_n(T) \cdot N_V(T)\,\mu_p(T)\right)^{1/2} \cdot e^{-E_G(T)/2k_B T} . \tag{6.5}$$

(μ_n and μ_p are the mobilities of the respective charge carriers). Figure 6.4 shows the Arrhenius plot of $\sigma_{el,min}$ against the inverse absolute temperature. The bandgap energy $E_G(0\ K)$ can be calculated from the slope and the temperature coefficient β_G from the intercept with the y-axis.

With $N_C(T)$, $N_V(T)$, $\mu_n(T)$ and $\mu_p(T)$ taken from [5], the following values are obtained, which are in satisfactory agreement with the literature :

$$E_G(0K) = (3.30 \pm 0.17)\ eV \tag{6.6}$$

$$\beta_G = (5 \pm 1) \cdot 10^{-4}\ eV/K . \tag{6.7}$$

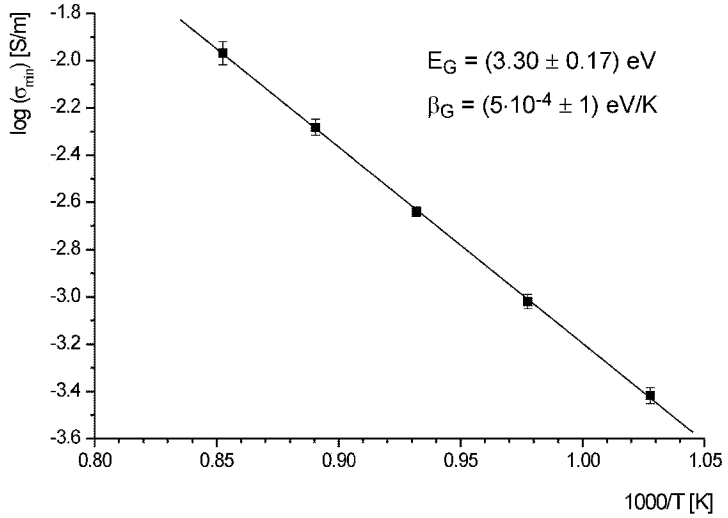

Figure 6.4

Arrhenius diagram of the electronic conductivity minima of the $SrTiO_3$ single crystal for the determination of the bandgap energy $E_G(T) = E_G(0K) - \beta T$. The line is a least squares fit.

Unfortunately, the measurement does not allow further information to be obtained on the reduction and oxidation enthalpies, ΔH_{red} and ΔH_{ox}, respectively. The reason is that ΔH_{red} is obtained from the activation in the intrinsic - $^1/_6$ - regime and ΔH_{ox} by $\Delta H_{red} + \Delta H_{ox} = 2E_G$. In this case, the determination would be very vague. But, for reasons of comparison, the activation energies in the $\pm$ ¼ - regimes were calculated (the errors mean upper limits):

$$\begin{aligned} E_{A,red} &= (2.78 \pm 0.14)\ eV \\ E_{A,ox} &= (0.51 \pm 0.05)\ eV \end{aligned} \qquad (6.8)$$

The contribution of ionic conductivity due to oxygen vacancy diffusion plotted in Figure 6.5 can be obtained by subtracting the electronic part, i.e. the fit curve, from the total conductivity, in other words the difference between the two curves in Figure 6.3. As can be expected from the activation energies, the ionic part is only of significance at lower temperatures and when the electronic charge carrier concentration is at a minimum. Although the influence is quite small at these measurement temperatures, the activation energy of oxygen vacancy diffusion can be determined by starting from the Einstein equation that relates the diffusion constant to the mobility according to

$$D_i = \mu_i RT/z_i F \qquad (6.9)$$

R is the gas constant, F the Faraday constant and z_i the charge on the ion, here an oxygen vacancy $V_O^{\bullet\bullet}$, and μ_i the mobility. D is the diffusion constant, which follows an exponential thermal activation:

$$D_i = D_{i,0} \cdot e^{-E_{A,i}/k_B T} \tag{6.10}$$

Substituting $\mu_{V\ddot{o}}$ from $\sigma_{V_O^{\bullet\bullet}} = 2e_0 \cdot \mu_{V_O^{\bullet\bullet}} \cdot [V_O^{\bullet\bullet}]$, where $2[V_O^{\bullet\bullet}] = [A']$ is the compensation for the acceptor impurities (here $[Mn_{Ti}']$), the following expression is obtained:

$$\sigma_{V_O^{\bullet\bullet}} \cdot T = \frac{2e^2}{k_B[A']} \cdot D_0 \cdot e^{-E_{A,V\ddot{o}}/k_B T} \tag{6.11}$$

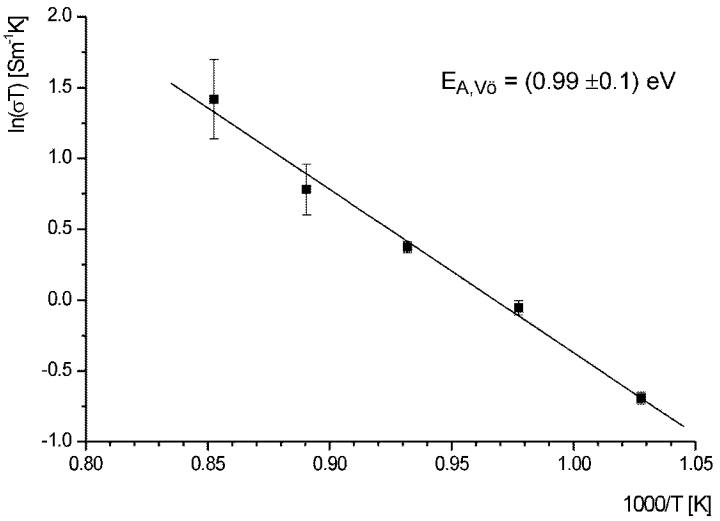

Figure 6.5

Arrhenius diagram for the calculation of the thermal activation energy of oxygen vacancy diffusion. The data were obtained by subtracting the electronic contribution from the total conductivity in Figure 6.2.

From the linear fit in Figure 6.5, the activation energy for oxygen vacancy diffusion can be calculated as

$$E_{A,V_O^{\bullet\bullet}} = (0.99 \pm 0.1)\ \text{eV}, \tag{6.12}$$

which agrees very well with the data known from the literature (see Chapter 3).

This section demonstrates the capabilities and especially the reliability of the setup with respect to the control of the oxygen partial pressure. Furthermore, the measurement on the $SrTiO_3$ single crystal yielded an indispensable reference for comparison with the following thin film measurements. The agreement with the data published in the literature is excellent and again confirms the defect chemical expectations. Though the absolute values of σ of the $SrTiO_3$ single crystal can vary slightly, mainly due to inaccurate temperature determination, the single crystal data are a very precise reference because the measurements were performed on the same setup as the experiments described in the following.

6.3 Polycrystalline Thin Films

With respect to the applications mentioned in Chapter 1, which are accompanied by feature sizes of several ten nanometers due to common thin film deposition parameters and often insufficient lattice accommodation to the substrate, polycrystalline thin films probably represent a very common morphological habit. Therefore, the investigations first focus on CSD thin films (see Chapter 4), which have a mean grain size of approximately 50 nm and therefore stand for the extreme opposite to the single crystal regarding the density of interfaces.

General Behavior

In Figures 4.4 – 4.7, the morphological and structural properties of a typical CSD-processed strontium titanate thin film are illustrated in detail. The film STO5 exhibits a columnar, polycrystalline and non-textured single-phase perovskite structure. This nominally undoped $SrTiO_3$ film showed a slight concentration of acceptor-type elements (~ 500 to 1000 ppm, [8]) due to unavoidable impurity incorporation; the thickness is about 500 nm and the mean grain diameter of the columns is roughly 50 nm.

The very surprising conductivity behavior is shown in the double logarithmic plot in Figure 6.6 for the temperature range from 700 to 1000 °C. Apparently, the film reveals several substantially different characteristics compared to those of the single crystal shown in Figure 6.2.

Figure 6.6

Conductivity characteristics of a nominally undoped $SrTiO_3$ thin film STO5.The columnar structured polycrystalline morphology is pictured in Figure 4.4.

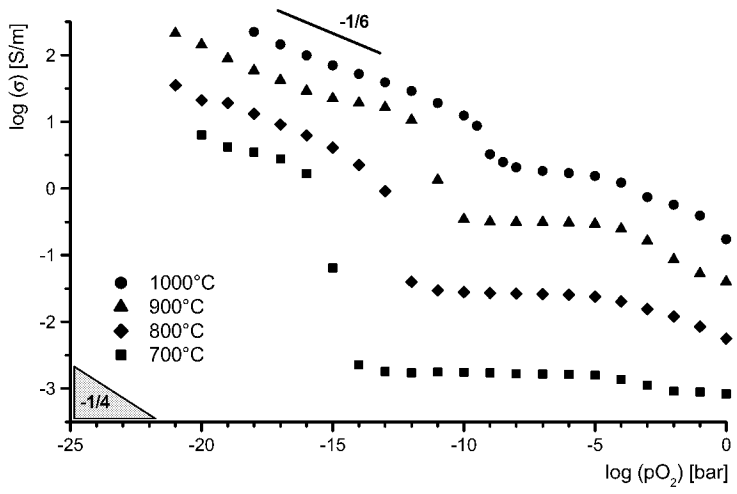

The most remarkable feature is certainly the drop of the conductivity curve down to a plateau region stretching over several decades of oxygen partial pressure. Another apparent characteristic is the lack of a p-type increase of σ under oxidizing partial pressures.

Looking at the behavior under reducing conditions, which approximately range from 10^{-20} bar up to 10^{-15} bar at 700 °C and up to 10^{-10} bar at 1000 °C, the shape of the curve is the same as that of the typical n-type behavior of σ in single crystals. This regime is attributed to the generation of electrons due to the loss of oxygen to the atmosphere although the slope is only - $1/6$. Because the overall conduction behavior is so drastically different, it cannot be said at this point whether the slope of - $1/6$ stems solely from the reduction reaction as is the case for the single crystal. Another significant difference is that the absolute values of σ in this region are approximately 2 orders of magnitude higher than that of the single crystal.

Following the curve towards oxidizing conditions, the conductivity exhibits a sharp drop to a regime where σ does not change visibly with the pO_2. Within the resolution of the pO_2 values, σ drops in less than one decade to the plateau and covers nearly 3 orders of magnitude at 700 °C, while at 1000 °C it is reduced to about half a decade. The partial pressure at which the jump occurs also shifts with temperature from about 10^{-15} bar at 700 °C to ~ $10^{-9,5}$ bar at 1000 °C. With regard to deviations in the control of the oxygen partial pressure, which was discussed in Chapter 5.2, a measurement artifact, as is assumed in literature [10], can be excluded here.

The characteristics under oxidizing conditions, at partial pressures of 10^{-5} bar and above, are also quite different. According to the behavior of bulk materials, an increasing p-type conductivity with a slope of + ¼ would be expected, resulting from the increasing generation of electron holes. But in this case, the conductivity decreases further. The decline is only barely visible at 700 °C and becomes more pronounced for higher temperatures. Because of the missing p-type regime, an intrinsic minimum does not occur either.

The plateau regime is noteworthy because it reminds one of a classical donor plateau as depicted in Figures 3.5 and 3.6. There, a donor type impurity is compensated by electrons (Equation (3.33)) and σ does not change with pO_2 [5]. As described in Chapter 3, the thermal activation of the conductivity in a donor plateau regime stems solely from the power-law dependence of the electron mobility $\mu_n(T)$. Figure 6.6 leads to the assumption that the plateau region of the $SrTiO_3$ thin film cannot be attributed to a donor doping. To confirm this, the dependence on temperature is calculated from an Arrhenius plot, which is shown in Figure 6.7.

Figure 6.7

Thermal activation in the n-type regime and the plateau region of the undoped $SrTiO_3$ thin film STO5. Values were obtained by linear fits of the n-type as well as the plateau region.

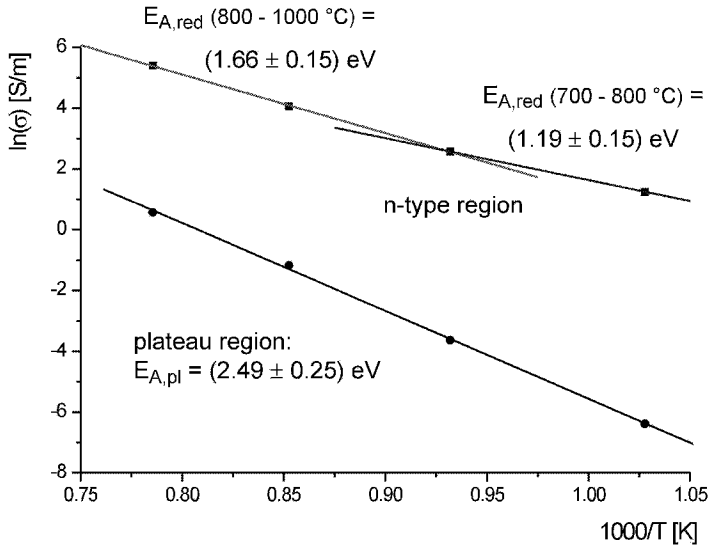

Evidently, the activation in the plateau follows an exponential behavior and therefore undoubtedly speaks against a donor plateau. Another piece of evidence is the drop to the plateau instead of a continuous transition, which is typically observed for donor-doped titanates.

The question arises of whether the plateau region can be attributed to ionic conduction. Looking at the curve taken at 700 °C, the sharp drop from the n-type region to the plateau covers nearly three orders of magnitude. The absolute conductivity value in the plateau is $\sigma(700\ °C) \approx 10^{-2.75}$ S/m, which roughly equals the conductivity of the single crystal in the minimum, where the electrons and holes are at minimum and oxygen vacancies become the dominant charge carriers. This leads to the assumption that in the case of the thin film plateau the electrons are trapped, however, and the residual conductivity is dominated by ionic charge carriers, too. The thermal activation in this region is calculated by the Arrhenius plot as

$$E_{A,pl} = (2.49 \pm 0.3)\ \text{eV}\,. \tag{6.13}$$

This is considerably higher than the activation energy for oxygen vacancy diffusion which was determined in the previous section to be ~ 1 eV. From this point of view, it has to be concluded that either the diffusion is hindered by the high interface density or that the current is not carried by oxygen vacancies but another ionic species.

The thermal activation of the conductivity in the reducing regime is determined as

$$\begin{aligned} E_{A,red} &= (1.66 \pm 0.15)\ \text{eV}\ (800\,°C \le T \le 1000\,°C) \\ E_{A,red} &= (1.19 \pm 0.15)\ \text{eV}\ (700\,°C \le T \le 800\,°C) \end{aligned} \tag{6.14}$$

In contrast to the single crystal, where $E_{A,red}$ = 2.78 eV (Equation (6.8)), the activation energy for reduction is significantly lowered. Interestingly, at temperatures below 800 °C the activation energy decreases further. Due to missing p-type region, the bandgap energy as well as the oxidation enthalpy cannot be determined from this electrical measurement.

This very different behavior was also observed for differently prepared $SrTiO_3$ thin film samples of similar morphology and thickness. Furthermore, the curve taken at 700 °C was measured several times to prove its reproducibility. The conductivity characteristics of undoped polycrystalline $SrTiO_3$ thin films exhibit a lot of differences compared to bulk behavior. The discrepancies are so fundamental that an explanation by the established point defect chemistry, at first fails. Nevertheless, under reducing conditions the slope of the conductivity curves does show apparent similarities to bulk behavior. Therefore the question arises of the parameters which alter this behavior and if further similarities or an approximation to the bulk behavior can be found. This will be studied in the next section by hetero- and isovalent cation substitution and in the following by varying the film morphologies.

Doping Effects

In Chapter 3 it was discussed in detail how the incorporation of acceptor- or donor-type impurities influences the conduction behavior of bulk titanate material. That's why the question arises of if and how these unusual characteristics of polycrystalline strontium titanate films are affected by doping.

Figure 6.8

Conduction behavior of a 0.7 at.% Mn-doped $SrTiO_3$ thin film (STMO6). The thickness is 500 nm.

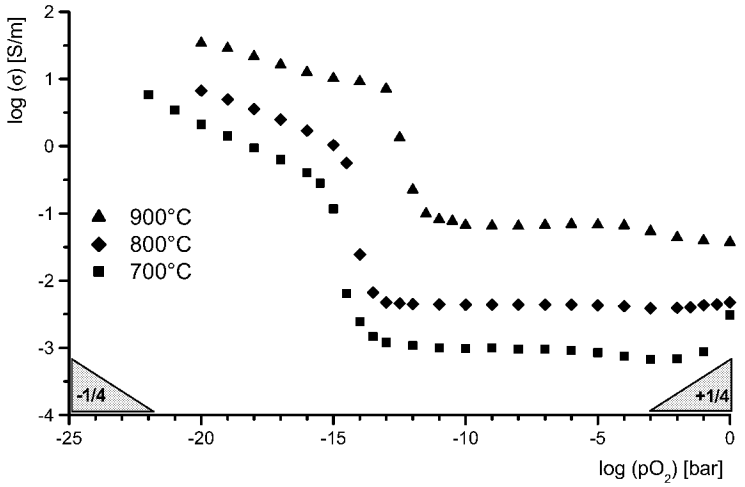

Figure 6.8 shows the conduction behavior of a 0.7 at.% manganese-doped $SrTiO_3$ thin film. Although Mn has a variety of oxidation states it is most often found in the literature reacting as an acceptor-type dopant in titanates. The morphology of the film is quite similar to that of the undoped film due to nearly identical processing parameters. The thickness is also approximately 500 nm.

Apparently, the curves resemble the characteristics of the undoped film. Again, a drop occurs that is followed by a broad plateau region. Under reducing conditions the curve reflects the n-type behavior and under higher oxygen partial pressures, the p-type conduction is largely suppressed. Only at 700 °C and nearly pure oxygen atmospheres can a noticeable increase according to an electron hole conduction be seen.

The absolute values are about half a decade below those of the undoped film (Figure 6.6). The position of the drop appears to be at roughly the same pO_2 value at 700 °C, but does not shift as far as the undoped film towards higher partial pressures with increasing temperature.

The determination of the activation energies is again only possible for some regions. Due to the missing p-type increase under oxygen-rich atmospheres, neither the bandgap energy nor the oxidation enthalpy can be calculated. The determination of the thermal activation under reducing conditions and in the plateau region reveals the following values:

$$\begin{aligned} E_{A,red} &= (1.53 \pm 0.3)\ \text{eV} \\ E_{A,pl} &= (2.06 \pm 0.7)\ \text{eV} \end{aligned} \tag{6.15}$$

Within the tolerance these values are comparable to those of the undoped film (Equations (6.13) and (6.14)). The influence of the acceptor concentration was examined by increasing the amount of incorporated manganese successively up to 3 at.%. As can be seen in Figure 6.9, the general behavior presented so far is unchanged. But the interesting detail here is that the position of the drop shifts to more reducing atmospheres with increasing Mn concentration. This trend, namely a shift of the conductivity characteristic to more reducing atmospheres as a result of increasing acceptor concentration, is also known for bulk materials (see Section 3.1.3).

Figure 6.9

Influence of acceptor-type dopant concentration on the conductivity of polycrystalline $SrTiO_3$ thin films (500 nm thick) [7].

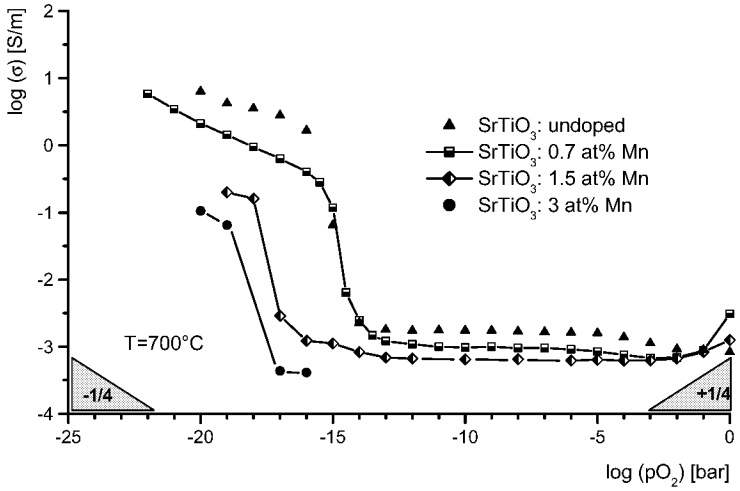

Figure 6.10 depicts the behavior of a 2 at.% lanthanum donor-doped thin film. In comparison to acceptor doping, the donor doping increases the overall conductivity slightly, and the general characteristics again resemble those observed for the other $SrTiO_3$ thin films. The n-type regime shows slopes of approximately - $^1/_8$ and the drop is shifted to higher partial pressures by 1 – 2 decades compared to the undoped case.

Figure 6.10

Conduction behavior of a 2 at.% La-doped $SrTiO_3$ thin film (ST_HTL04).

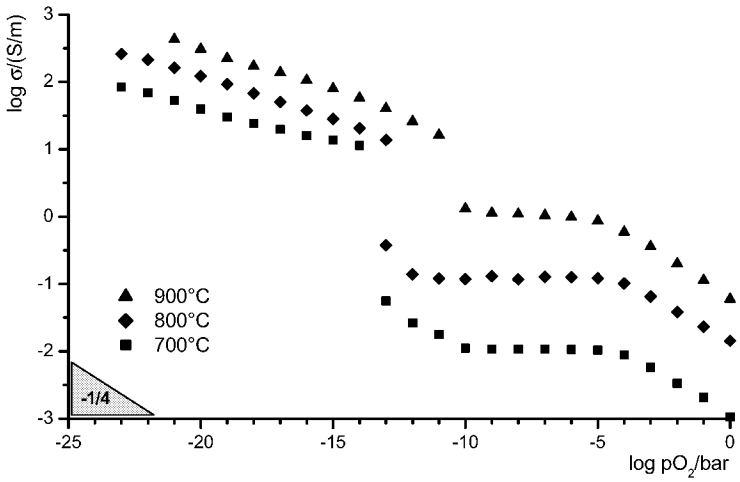

Under oxidizing ambients, the conductivity clearly decreases with a slope of - ¼. This behavior is different to what has been found for the undoped and acceptor-doped films, but it fits very well with the situation described for donor-doped bulk materials (see Chapter 3, especially Figure 3.5

and Figure 3.6). This decrease of σ, with increasing pO_2 starting around 10^{-5} bar, amounts to more than one order of magnitude up to 1 bar oxygen.

The activation energies in the reducing, plateau and oxidizing regions are determined as

$$\begin{aligned} E_{A,red} &= (1.01 \pm 0.1)\ eV \\ E_{A,pl} &= (2.26 \pm 0.15)\ eV \\ E^{*}_{A,red} &= (2.01 \pm 0.3)\ eV\ . \end{aligned} \qquad (6.16)$$

$E_{A,red}$ is considerably lower than before. In how far this is related to the donor incorporation requires further experimental evidence. The thermal activation in the plateau region agrees again very well with the behavior of the other films. The decline of σ under oxidizing conditions is activated with an energy of ~ 2 eV, which is in the same order as the activation energy in the - ¼ -regime of single crystals (see Equation (6.8)).

In summary, doping in polycrystalline thin films shifts the conductivity characteristics with respect to the pO_2 values and the absolute conductivity values, but the specific thin film features are still observed.

Isovalent Substitution / Solid Solutions

In addition to the incorporation of doping elements, also isovalent cation substitution was investigated because especially the $Ba_{0.7}Sr_{0.3}TiO_3$ solid solution is of interest for DRAM and for HF capacitor applications. Figure 6.11 shows the conduction behavior for selected members of the solid solution series $Ba_{1-x}Sr_xTiO_3$ (BST), namely the pure compositions $SrTiO_3$ and $BaTiO_3$ and $Ba_{0.7}Sr_{0.3}TiO_3$.

These films were also prepared by CSD and with respect to morphology and thickness are equivalent to the previously described films. For different BST bulk materials, the high temperature conductivity behavior is very similar (see Chapter 3.4). For the thin films, which exhibit comparable morphologies, the general trend is also retained. The remarkable fact is that the drop is shifted towards higher oxygen partial pressures over five decades when going from pure $SrTiO_3$ to pure $BaTiO_3$. The behavior in the n-type regime does not follow this uniform trend with respect to the Ba/Sr ratio, whereas the conductivity values in the plateau are almost identical. For comparison, the equivalent conductivity of the sapphire wafer at 700 °C is still lower than the plateau values.

Figure 6.11

Conductivity behavior of different members of the solid solution series $Ba_{1-x}Sr_xTiO_3$ [7]. The thickness of these CSD-prepared samples was approximately 500 nm.

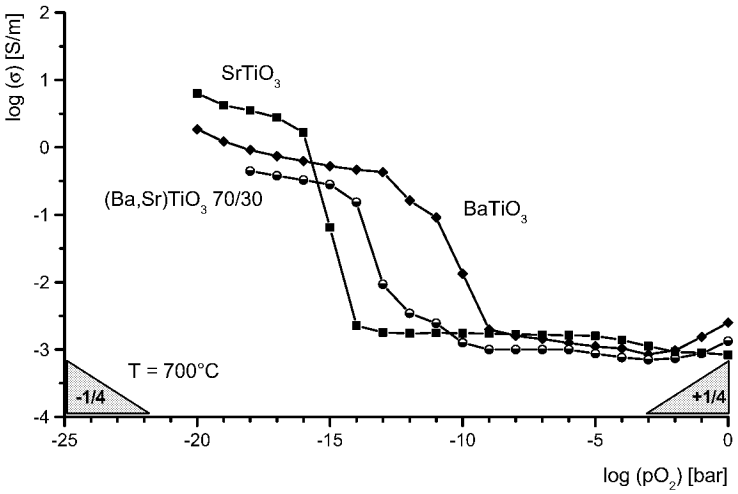

The solid solution series $BaTi_{1-y}Zr_yO_3$ was studied for selected stoichiometric compositions and reveals a marked alteration of the conduction behavior. As can be seen in Figure 6.12, an increasing content of zirconium drastically reduces the conductivity in the plateau region, but most significantly in the n-type regime. The end member of this series, $BaZrO_3$, barely shows a dependence on the oxygen partial pressure at all. The lowest values come close to the order of magnitude of the substrate's conductivity so that a quantitatively analysis is impossible.

Figure 6.12

Conductivity behavior in the solid-solution system $BaTi_{1-y}Zr_yO_3$.

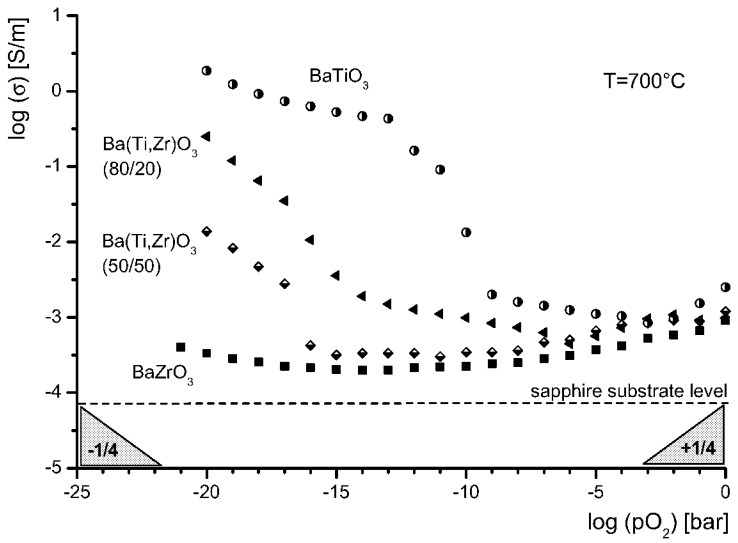

The behavior can be understood from the fact that zirconium is a much more stable element with respect to reduction than Ti and keeps the valence +4. Therefore, the generation of electrons due

to chemical reduction is drastically hindered. When the curve does reach the n-type region, it qualitatively follows a slope of - ¼.

6.4 Reduction of the Interface Density

Up to now, exclusively the conductivity characteristics of CSD prepared polycrystalline thin films have been discussed. The morphology of these films is somehow similar with respect to the grain size and all of them have a thickness of approximately 500 nm. As has been shown so far, the conductivity behavior of these films exhibits similar characteristics. The characteristics are generally also retained if iso- or heterovalent cation substitutions are performed (neglecting the zirconate samples for obvious reasons).

The major differences between respectively a single crystal or a coarse grained ceramic, as they are presented in literature, and the CSD thin films studied in this work are certainly, firstly, the fact that the thin films have a nanocrystalline morphology with grain sizes less than 100 nm and, secondly, thin films are clamped to a substrate and have thicknesses of 500 nm and below, which is much smaller than the thickness of bulk samples.

In order to elucidate the interplay between these effects on the conductivity curve and the interface density or the grain size, the morphological habit was varied in a series of nominally undoped $SrTiO_3$ thin films processed by PLD. The variation of the grain size was accomplished by changing the substrate temperature during processing as described in Chapter 4. The morphologies and structures of these PLD grown films are shown in Figures 4.9 and 4.10. Compared to the CSD thin films, only sample #3666 has a comparable morphology, as demonstrated by SEM and confirmed by the TEM analysis of Figure 4.13. The columns are single crystalline and, in contrast to the CSD process, neither intra- nor intergranular pores appear. In addition, this sample is highly textured and it has to be assumed that a lot of ordered small angle grain boundaries exist [12]. Sample #3667 is completely polycrystalline without any pronounced texture. The grains are columnar in shaped with a diameter of 50 – 100nm [12]. Sample #3668 is also polycrystalline and the shape of the grains, which are 200 – 400 nm in diameter, is equiaxed. Finally, also an epitaxial thin film was included in this study. Common to all films is a thickness of approximately 1 μm.

The conduction behavior as a function of the oxygen partial pressure is shown in Figure 6.13. Obviously, the curves generally resemble the bulk behavior much more than revealing similarities with the CSD derived films. Undoubtedly, the behavior under reducing conditions can be attributed to n-type electron conduction and under oxidizing atmospheres, the p-type region appears where the conductivity increases due to the generation of holes. However, the curves also reveal some features that are similar to the CSD films. The absolute conductivity values of the thin films in the n-type region are always higher than for the single crystal, but without a clear trend. Under oxidizing ambients, the characteristics show decreased p-type conductivities, which in the case of the columnar, polycrystalline sample (#3667) amounts to ~1 order of magnitude. On the other hand, there is almost no difference between the epitaxial film (#3461) and the single crystal in this regime. The values of the coarse grained and the textured films lie in between.

Overall, this is the first clear evidence for the importance of the grain boundary density: The more interfaces exist, the more pronounced is the decrease of the p-type conductivity.

The fact that the behavior of the textured film is almost identical to that of the coarse grained sample does not fit into this picture. Perhaps this has to be attributed to the texture, i.e. the ordered habit of the grain boundaries [16]. But at the present point, this remains unclear.

Figure 6.13

Conduction characteristics of PLD-derived thin films with different morphological habits, especially with variable grain boundary densities. For SEM and TEM analysis see Figures 4.9 and 4.10.

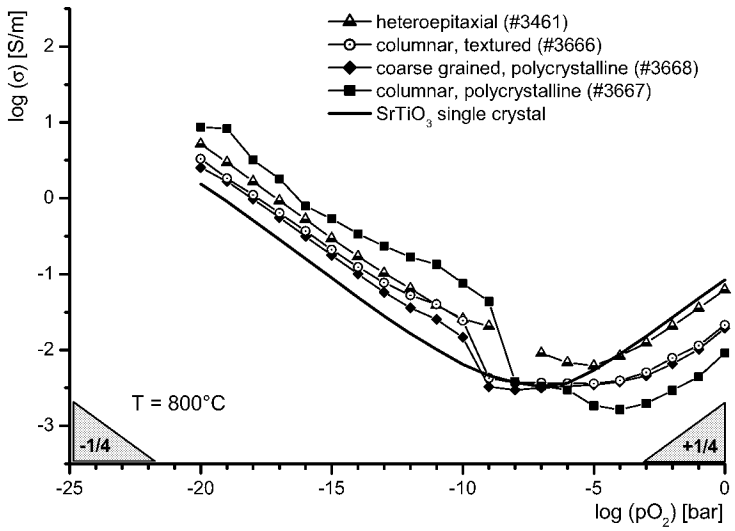

Another interesting detail is apparent for the polycrystalline thin films at oxygen partial pressures between 10^{-10} bar and 10^{-5} bar. Here a small drop and a plateau region can be seen in the conductivity behavior, which indicates a similar behavior to that of the CSD films. This effect is again predominant for the columnar polycrystalline sample #3667.

6.5 Heteroepitaxial Thin Films

As was shown in the last paragraph, the unusual conductivity characteristics of polycrystalline thin films, primarily the drop and the subsequent plateau region, exhibit a close relation to the density of grain boundaries in the films. Especially the heteroepitaxial $SrTiO_3$ thin film is interesting due to its bulk-like behavior. This is the motivation for investigating such films in more detail. Within the analytical limits of XRD, RBS and SEM, this film (#3461) does not exhibit any internal interfaces and can therefore be treated as single crystalline (see Figures 4.9 – 4.12).

Figure 6.14

Conductivity behavior of a heteroepitaxial $SrTiO_3$ thin film on MgO with a thickness of 1 µm. Missing values are due to technical problems.

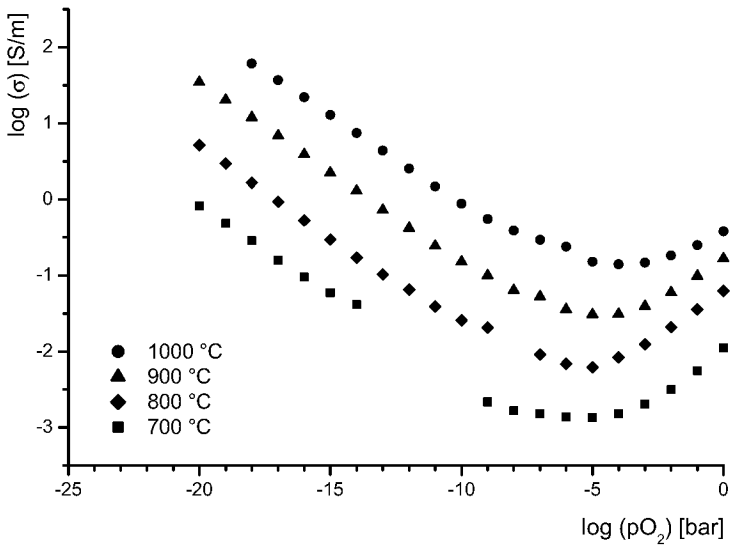

The conduction characteristics for the 1 µm thick heteroepitaxial $SrTiO_3$ film as a function of the oxygen partial pressure at different temperatures are depicted in Figure 6.14. Obviously, the behavior of this film is remarkably similar to that of bulk materials and corresponds to expectations from the established defect chemical model. The measurement curves at all temperatures reveal an n-type regime under reducing and a p-type behavior under oxidizing conditions and the slopes in these electronic branches fit the anticipated value of ± ¼ very well. In the mid range pO_2 regime, the curves show intrinsic minima.

In Figure 6.15, the corresponding curves from the single crystal have been added for quantitative comparison. On closer inspection, several differences are noticeable. First of all, the intrinsic minimum is shifted towards higher oxygen partial pressures when approaching lower tem-

peratures. This has direct consequences on the thermal activation of the absolute conductivity values in the reducing and oxidizing regimes, respectively, and on the calculated bandgap energy.

Figure 6.15

Comparison of the epitaxial film conductivity (symbols) with that of the single crystal one's (lines). Note that the curve of the single crystal at 1000 °C is extrapolated.

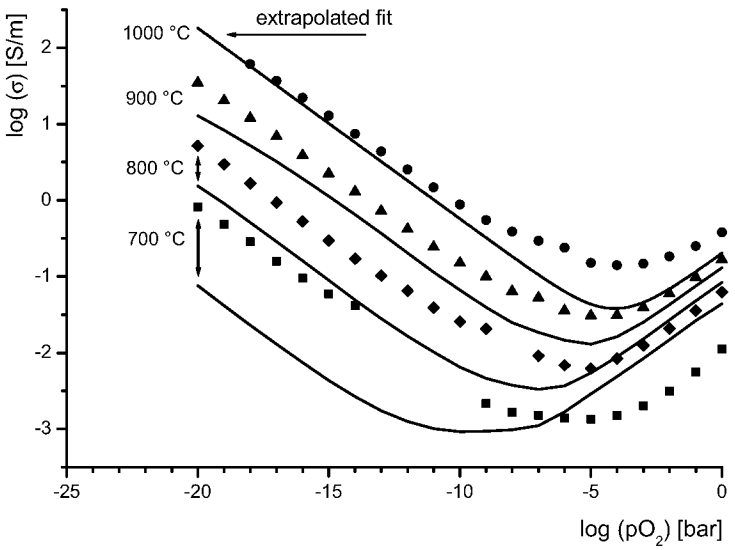

The values from an Arrhenius plot of the heteroepitaxial film cannot be fitted well by least squares. Therefore, the individual temperature regimes are considered separately:

Figure 6.16

a.

Arrhenius diagrams for the activation in the n-type and p-type regimes in Figure 6.14. Additionally, the thermal activation of the electronic conductivity minimum is plotted.

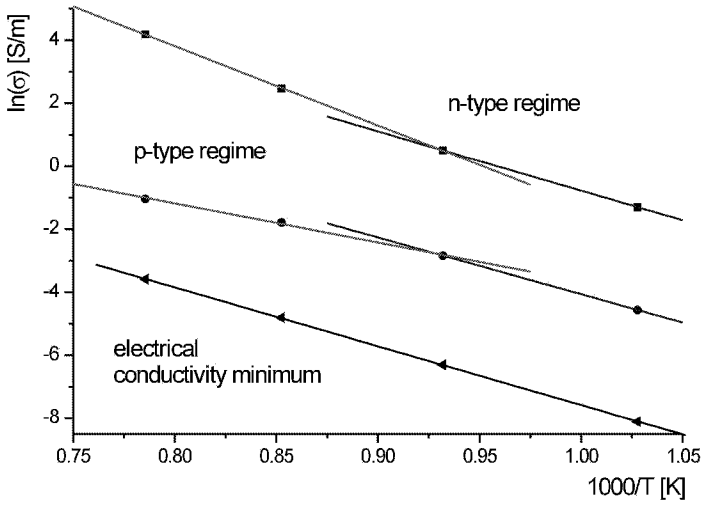

b.

Activation energies of the hetero-epitaxial $SrTiO_3$ thin film #3461.

temperature range	$E_{A,red}$	$E_{A,ox}$
700 - 800 °C	1.62 eV	1.55 eV
800 - 1000 °C	2.17 eV	1.06 eV

The particular detail here is that the energies markedly change with temperature. At temperatures between 700 and 800 °C, $E_{A,red}$ is comparable to values of the CSD-prepared $SrTiO_3$ thin film, whereas in the interval of 800 – 1000 °C, the activation energies can be compared to the values of the single crystal.

In contrast, the values of the electronic conductivity minimum are on a straight line. By fitting the electronic contribution to the conductivity in the ± ¼ branches, the bandgap energy can be determined and compared to the data found for the single crystal in Section 6.2. Here, the bandgap energy of the heteroepitaxial $SrTiO_3$ thin film (#3461) was calculated as

$$E_G = (3.35 \pm 0.2)\,eV\,, \tag{6.17}$$

which agrees well with the single crystal value.

Thickness Effects

As pointed out in Chapter 4, the PLD process enables single crystalline thin films of different thicknesses to be grown. It allows the extent to which the surface affects the conduction characteristics to be studied. This is shown in Figure 6.17 for $SrTiO_3$ films of thicknesses from 250 nm up to 3 µm measured at 700 °C. For comparison, the values of the single crystal are also plotted.

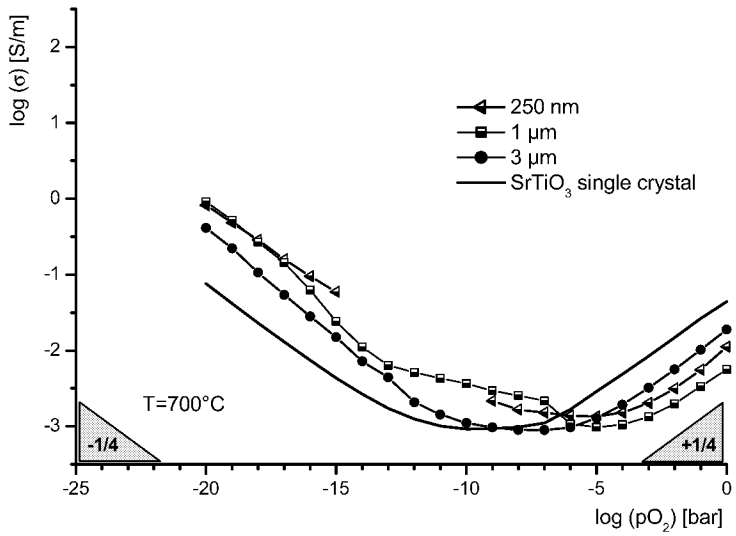

Figure 6.17

Influence of the film thickness on the conductivity behavior of heteroepitaxial, PLD-processed strontium titanate thin films.

The curves reveal interesting details. First of all, each film resembles more or less the characteristics of bulk materials. Looking closer at reducing conditions, the decrease of the film

thickness leads to an increase of the conductivity. For oxidizing atmospheres, the absolute values decline with decreasing thickness.

Another feature appears for the 250 nm thick film between 10^{-16} bar and 10^{-8} bar. Here, first indications become visible of a drop and a plateau region. This is an indication of the dimension at which the characteristics begin to alter from bulk behavior.

6.6 Nanocrystalline Ceramics

On the one hand side, the results presented in the previous sections reveal that CSD-prepared polycrystalline $SrTiO_3$ thin films exhibit drastic changes in the conduction characteristics compared to the single crystals. On the other hand, a successive decrease of the grain size, from coarse grained to finally single crystalline PLD films, more or less restores bulk behavior. From these experiments, the interface density is primarily thought to be responsible for the effects on conductivity characteristics like the drop and the plateau region.

In order to substantiate this picture, nanocrystalline ceramics were investigated to see whether they also show the effects of a drop and the plateau region in the conductivity characteristics. The results found in the literature for polycrystalline $SrTiO_3$ ceramics were obtained for samples with grain sizes down to a few micrometers and the results agree fully with the single crystal characteristics [13]. For a comparison with the thin films, it is necessary to further decrease the grain size to comparably small dimensions of several tens of nanometers. As described in Chapter 4, the microemulsion technique for the first time provides particle sizes below 10 nm and by using such a powder it was possible to prepare a nanocrystalline $BaTiO_3$ ceramic with a mean grain size of approximately 100 nm (Figure 4.15). The measured sample, which was cut from the middle of the sintered sample presumably exhibits an even smaller grain size and much less porosity as is visible in the picture. This is due to the HUP processing and the fact that the SEM picture was taken near to the margin of the sample. As has been pointed out in Chapter 3, the similarities of strontium titanate and barium titanate with respect to the high temperature conductivity characteristics allow this nanocrystalline $BaTiO_3$ ceramic to be compared with the $SrTiO_3$ thin films.

The conductivity characteristics of the nanocrystalline $BaTiO_3$ sample are quite remarkable and are depicted in Figure 6.18. Apparently, the behavior is very similar to what is found for the polycrystalline thin films.

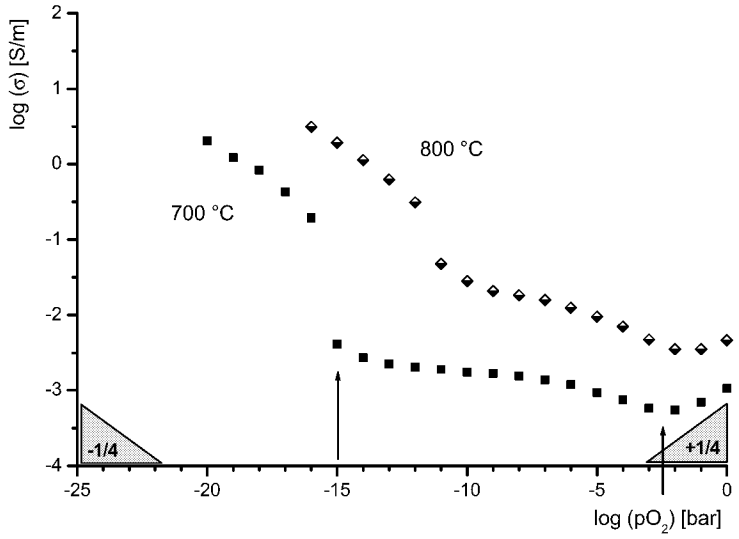

Figure 6.18

Conduction behavior of a nanocrystalline $BaTiO_3$ ceramic with a mean grain size of about 100 nm. The sample was hot uniaxially pressed from microemulsion-synthesized $BaTiO_3$ powder (see Chapter 4).

Under reducing conditions, the typical n-type behavior can be seen. And as in the case of the thin films, the absolute values of σ lie significantly above the bulk values, here about 1.5 decades [14]. The slope in this region of the log(σ) - log(pO_2) - plot fits - ¼ quite well. Towards higher oxygen partial pressures, a drop of the conductivity and an accompanying plateau region appear. Under oxidizing conditions, i.e. at oxygen partial pressures greater than approximately 10^{-7} bar, the conductivity first decreases slightly more, then a minimum is obtained before σ increases, which indicates the transition to a p-type behavior. Because this minimum is at relatively high oxygen partial pressures, a slope of + ¼ is only indicated. The approximate thermal activation energies in the n-type as well as in the plateau region can be calculated as

$$\begin{aligned} E_{A,red} &= 2.47\ \text{eV} \\ E_{A,pl} &= 2.18\ \text{eV}\,. \end{aligned} \tag{6.18}$$

Because only two isotherms are available, an error cannot be stated. The activation energy under reducing conditions comes close to that of the single crystal [15]. This is quite noteworthy because the general characteristics of this sample resembles the behavior of polycrystalline CSD thin films; but there the activation energies are between 1 and 1.5 eV in the corresponding temperature regime (for undoped and acceptor type doping). In contrast, the heteroepitaxial PLD-derived $SrTiO_3$ film (#3461) generally revealed bulk behavior and also showed a reduced activation energy of 1.62 eV. The activation of σ in the plateau region is similar to that of the polycrystalline thin films. Due to the lack of information in the p-type regime, the electrical determination of the bandgap energy cannot be carried out.

In contrast to the thin films, where the determination of thermopower turned out to be impossible because of the film geometry, the nanocrystalline ceramic sample does provide this opportunity. The result for the barium titanate sample is shown in Figure 6.19. Because of the difficulties mentioned in Section 6.1, this measurement can only be considered as qualitative, because no thermocouple could be brought into direct contact with the sample. Therefore, the exact thermal gradient remains vague, and possible offset voltages are also unknown.

Nevertheless, qualitative evidence for dominant negative charge carriers in the attributed n-type regime and in the plateau region (compare to Figure 6.18) is undoubtedly given. In the n-type region, the absolute value of the thermopower is reduced, as expected from Equation (3.31). In the region of the conductivity plateau, the thermopower is also constant, but still negative. This points to negative charge carriers in this region, too. Under oxidizing conditions, the change of the sign according to the transition from n-type to p-type conduction is excellently confirmed.

Figure 6.19

Thermopower of the nanocrystalline $BaTiO_3$ ceramic. Compare to the conductivity behavior shown in Figure 6.18.

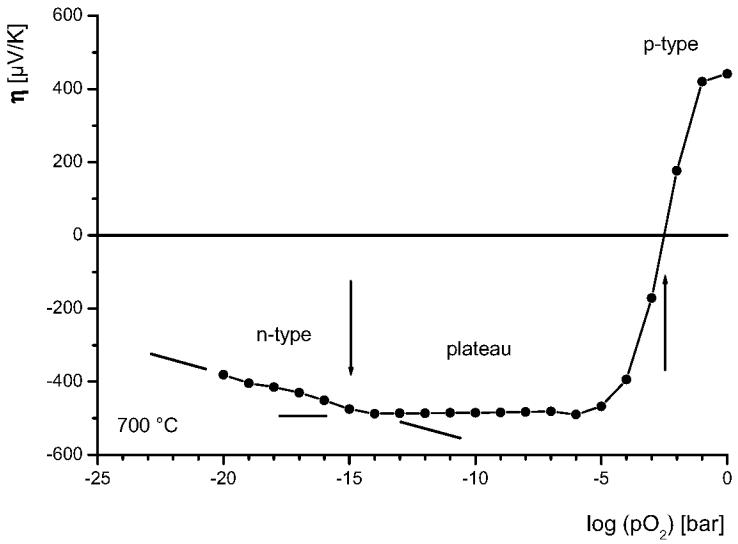

Generally, the conductivity characteristics of nanocrystalline $BaTiO_3$ reflect the behavior of titanate thin films with a high interface density. This confirms the dominant influence of grain boundaries in highly disordered nanocrystalline titanates on their conduction behavior. The similarities point to the possibility of applying a nanocrystalline ceramic as a model material for polycrystalline thin films.

A more detailed discussion on the numerous details of the different studies will be presented in Chapter 8.

References

[1] R. Moos, A. Gnudi and K.H. Härdtl, "Thermopower of $Sr_{1-x}La_xTiO_3$ ceramics" *J. Appl. Phys.* **78**, 5042 (1995).

[2] G.M. Choi, H.L. Tuller and D. Goldschmidt, "Electronic-transport behavior in single-crystalline $Ba_{0.03}Sr_{0.97}TiO_3$", *Phys. Rev. B* **34**, 6972 (1986).

[3] Fa. Litzenberger, Idar-Oberstein, Germany, an AES analysis revealed the following impurities: Al 52 ppm, Fe 16 ppm, Mn < 800 ppm, Cr and Nb < 2 ppm, see [4].

[4] Ch. Tragut, "Kinetik schneller Sauerstoffsensoren", PhD thesis, Universität Karlsruhe, Fortschrittberichte VDI, Reihe 8, Nr. 291, Düsseldorf, 1992.

[5] R. Moos, "Donatordotierungen im Strontiumtitanat: Elektrische Eigenschaften und modellhafte Beschreibung", PhD thesis, Fortschrittberichte VDI, Reihe 5, Nr. 362, Düsseldorf 1994.

[6] I. Denk, W. Münch and J. Maier, "Partial Conductivities in $SrTiO_3$: Bulk Polarization Experiments, Oxygen Concentration Cell Measurements, and Defect-Chemical Modeling", *J. Am. Ceram. Soc.* **78**, 3265 (1995).

[7] Ch. Ohly, S. Hoffmann-Eifert, K. Szot and R. Waser, "Defects in Alkaline Earth Titanate Thin Films - The Conduction Behavior of Doped BST", *Integr. Ferroelectr.* **38**, 229 (2001).

[8] Unpublished results. Based on an LA-ICP-MS (laser ablation inductively coupled plasma mass mpectrometry) impurity analysis by C. Pickhardt, ZCH, Research Centre Jülich, 2002.

[9] C.A. Palanduz and D.M. Smyth, "The effect of cation place exchange on the electrical conductivity of $SrBi_2M_2O_9$ (M=Ta, Nb)" *J. Europ. Ceram. Soc.* **19**, 731 (1999).

[10] A.A.L. Fereira, J.C.C. Abrantes, J.A. Labrincha and J.R. Frade, "Oxygen Losses and Electrical Conductivity of $SrTi_{1-y}Nb_yO_{3+\delta}$ Materials", *J. Europ. Ceram. Soc.* **19**, 773 (1999).

[11] R. Waser, "Bulk Conductivity and Defect Chemistry of Acceptor-Doped Strontium Titanate in the Quenched State", *J. Am. Ceram. Soc.* **74**, 1934 (1991).

[12] C.L. Jia, IFF (IMF), Research Centre Jülich, personal communication.

[13] N.H. Chan, R.K. Sharma and D.M. Smyth, "Nonstoichiometry in $SrTiO_3$", *J. Electrochem. Soc.* **128**, 1762 (1981).

[14] N.H. Chan and D. M. Smyth, "Defect Chemistry of $BaTiO_3$", *J. Electrochem. Soc.* **123**, 1584 (1976).

[15] N.H. Chan, R.K. Sharma and D.M. Smyth, "Nonstoichiometry in $BaTiO_3$", *J. Am. Ceram. Soc.* **64**, 556 (1981).

[16] S.R. Gilbert, L.A. Wills, B.W. Wessels, J.L. Schindler, J.A. Thomas and C.R. Kannewurf, "Electrical transport properties of epitaxial $BaTiO_3$ thin films", *J. Appl. Phys.* **80**, 969 (1996).

7 Morphological Aspects

This chapter addresses the important question of the extent to which the thin film samples might experience observable morphological changes initiated by the measurements due to the significant temperature load applied under various oxygen partial pressures and for different hold times. The importance of this point is evident, because measurement temperatures between 600 °C and 1000 °C are in the same range – sometimes even higher – than the deposition temperatures of the thin films. In the simplest case morphological changes result from grain growth. A more complicated scenario described in Chapter 3.3 might consider restructuring effects in the near-surface area as discussed by K. Szot for the surface of strontium titanate samples [1][2]. The essential question therefore arises: Do the high temperature conductivity measurements irreversibly alter the thin film samples in such a way that the electrical results might become unreliable?

7.1 Converging of Pores

Figure 7.1 illustrates the morphology of a CSD-prepared, polycrystalline 0.7 at.% Mn-doped $SrTiO_3$ film (STMO6) after a complete set of measurement cycles (see Figure 6.8). Additionally, this sample was annealed at up to 1000 °C over the whole range of oxygen partial pressures. In total, this film was under a temperature load of between 700 °C and 1000 ° for approx. 30 hours.

Figure 7.1

SEM cross section of a CSD-prepared 0.7 at.% Mn-doped $SrTiO_3$ thin film after measurement cycles, amounting to 30 hours at temperatures from 700 to 1000 °C.

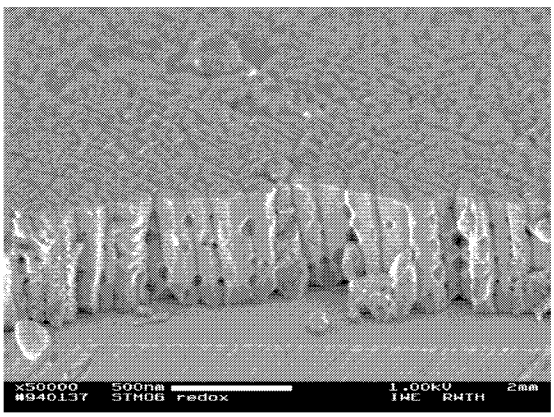

The picture reveals a changed morphology compared to the habit of the as-deposited film (similar to Figure 4.4). After the measurement cycling the sample exhibits a visible porosity at the grain boundaries. As has been discussed in Chapter 4, even in the as-deposited CSD film tiny intra- as well as intergranular pores appear (see Figure 4.5). A rough estimation of the amount of porosity after heat treatment does not provide support for an increase of porosity itself but, on the contrary, it can be assumed that the exposition to temperatures of up to 1000 °C leads to a converging of the pores already present [3]. This has been also confirmed by additional TEM analysis (not shown) [4].

Additional examinations were performed in order to find a lower temperature limit for this Ostwald-type process of pore converging. For this study samples were tempered at 900 °C for 4 hours under different oxygen partial pressures. As a representative example, the film heat-treated at a pO_2 of 10^{-4} bar is shown in Figure 7.2. In the cross section occasionally individual pores could be seen, thus marking the onset of pore converging. This study demonstrates that mass transport is clearly observed within reasonable times only for temperatures above 1000 °C. As a consequence, one has to keep in mind that the measurements performed at 1000 °C may have been accompanied by an Ostwald-type maturing process, and therefore may to a certain extent have changed the morphology of the thin film sample. In general, conductivity measurements were performed at temperatures from 700 °C to 900 °C, and for these conditions according to the investigations just presented we can neglect a significant effect of mass transport.

Figure 7.2

SEM cross section of a CSD-prepared undoped $SrTiO_3$ thin film after heat treatment at 900 °C for 4 hours under an oxygen partial pressure of 10^{-4} bar.

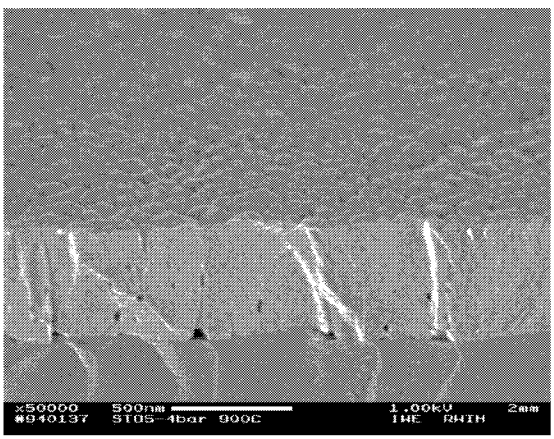

7.2 Surface Restructuring

In a series of studies polycrystalline $SrTiO_3$ thin film samples were exposed to different temperature loads under various oxygen partial pressures in order to perform a more detailed investigation of the morphological changes on the surface of thin films.

To eliminate the influence of exposure time, the samples were annealed for 24 hours in all experiments. The samples were annealed at temperatures from 700 °C to 1000 °C and under various oxygen partial pressures. The pO_2 values were chosen according to the characteristic regimes of the conductivity curve (see for instance Figure 6.6). That means, one batch of samples were annealed under reducing ambients, governed by a H_2/N_2 gas mixture to bring the samples into the n-type region. Another batch of samples was tempered in the plateau region (a mid-range pO_2, a controlled and constant oxygen flow of 10^{-8} bar) and the rest were finally exposed to air to achieve oxidizing conditions.

Figure 7.3

Polycrystalline, CSD-derived $SrTiO_3$ thin film; as-deposited.

This AFM measurement and those on the following pages were carried out by K. Szot (IFF).

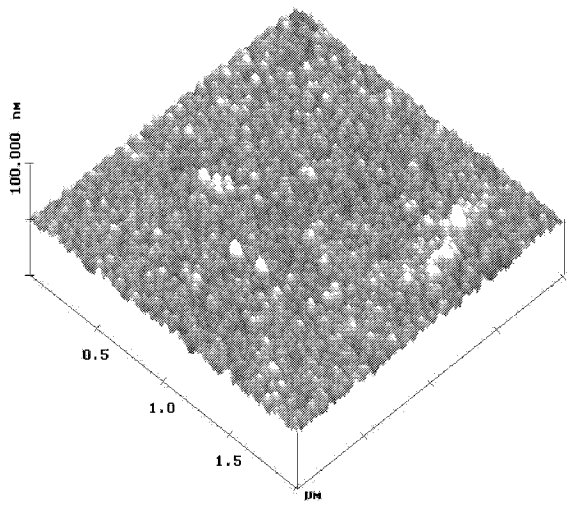

The state-of-the-art technique for topographical investigations is by atomic force microscopy (AFM), a method which can detect lateral features of several nanometers and offers an extremely high resolution in depth (better than 1 nm). As a reference, Figure 7.3 shows the CSD-prepared polycrystalline $SrTiO_3$ thin film STO5 in its as-deposited state (for a detailed description see Chapter 4.2). The rms roughness of this film was determined to be better than 2 nm and the local peak-to-valley value amounted to less than 10 nm [5][6]. This rather smooth surface quality

demonstrates the capabilities of batch-processing chemical solution deposition. It should be noted that the final densification and crystallization of these CSD films was performed under flowing oxygen atmosphere and temperatures of 800 °C.

Because most of the electrical measurements were taken at 700 °C, the first question addressed the changes at this temperature level. The topographies after annealing are shown in Figure 7.4 for three selected partial pressures, corresponding to the different conductivity regimes (see Figure 6.6).

Apparently, a morphological restructuring does not become significant at this temperature. Under all atmospheric conditions, the surface habit of the film remains virtually unchanged. The roughnesses of all three samples are comparably small and still in the order of 10 nm. Under oxidizing ambients, the surface appears even smoother than after deposition. On closer inspection, there is a certain tendency to an 'agglomeration' of grains (or columns), which is most prominent for the sample that was tempered at mid range oxygen partial pressures (Figure 7.4b). However, these effects are still minimal and are attributed to a minimization of surface energy. This leads to a faceting of the grains depending on their crystallographic orientation and this points to a simple reformation, i.e. a change of the grain shape, and not a restructuring to a new phase.

The unchanged thin film topography is a quite important result because, in comparison to typical measuring times of 9 – 12 hours, this relatively long annealing time of 24 hours does not lead to noteworthy changes. It can therefore be concluded that the morphology does not change significantly during the measurements.

Studies of annealed samples that were tempered at higher temperatures revealed larger changes of the topography, as could be expected from [1][2]. As examples, two examinations of thin film surfaces after annealing at 1000 °C are shown to illustrate the extent of these changes.

In Figure 7.5, the sample was annealed under reducing conditions of less than 10^{-14} bar O_2. The roughness is still relatively low, but the formation of terrace-like structures is clearly demonstrated. An accompanying SNMS depth profiling element analysis revealed a certain deviation from the stoichiometric composition (which was not quantified) within the topmost 10 - 30 nm of the surface [7]. However, the extent to which this has to be attributed to the formation of new phases remains unclear.

Figure 7.4

AFM surface analysis of STO5 after prolonged heating for 24 hours at T = 700 °C under different oxygen partial pressures.

a.

$pO_2 < 10^{-14}$ bar, (H_2/N_2 atmosphere)

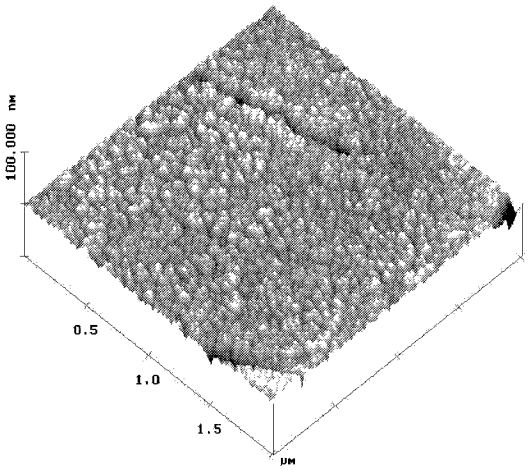

b.

$pO_2 = 10^{-8}$ bar, (constant pumping of flowing oxygen)

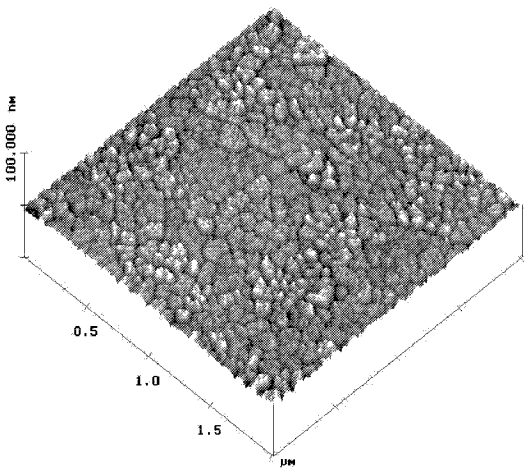

c.

$pO_2 \sim 0.2$ bar (air)

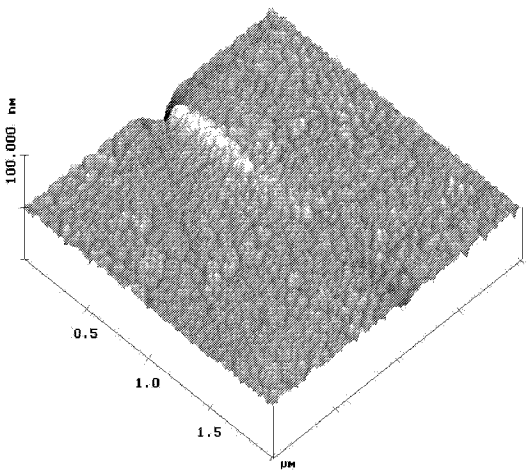

Figure 7.5

a.

$SrTiO_3$ thin film STO5 after annealing at T = 1000 °C, $pO_2 < 10^{-14}$ bar, t = 24 h

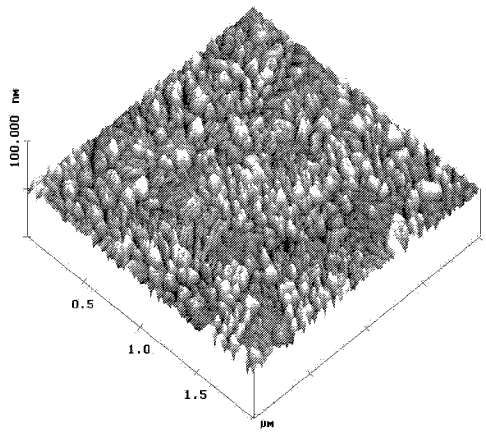

b.

Detail.

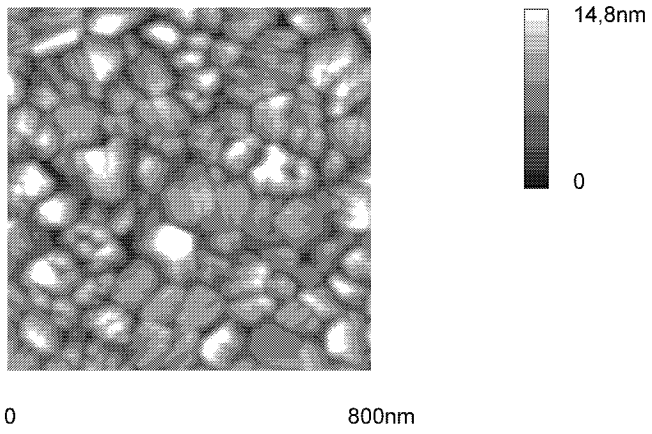

In contrast, an increasing oxygen concentration in the ambient atmosphere results in a pronounced faceting, where the height of individual facets can be estimated from Figure 7.6 to be 50 - 100 nm. This was scarcely visible after annealing at 700 °C, but now, at temperatures of 1000 °C, this effect becomes significant. Interestingly, the analysis by SNMS did not reveal a stronger influence on the stoichiometry, i.e. a further reaching compositional change. But it should be kept in mind that these changes evolved from a 1-day annealing procedure.

It has been shown that the surface region can be altered by prolonged annealing at comparatively high temperatures and extreme atmospheric conditions. The elucidation of the driving forces and the kinetics behind these restructuring effects go beyond the scope of this work. As far as electrical measurements here are concerned, it can be concluded from the results described in this chapter that morphological effects are negligible at lower temperatures and can

Figure 7.6

$SrTiO_3$ thin film STO5 after annealing at $T = 1000$ °C, $pO_2 = 10^{-8}$ bar, $t = 24$ h

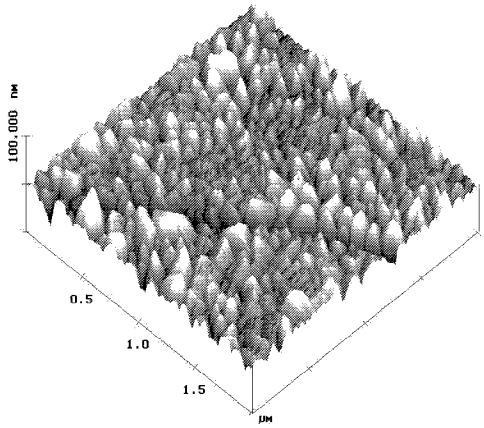

be considered to be small at higher temperatures. The most drastic changes were found for oxidizing conditions and temperatures of 1000 °C, a situation which was rarely encountered in measurements and lasted for only a few hours.

7.3 Interfacial Reactions between Film and Substrate

In order to check whether the measurement conditions affect the interface between the $SrTiO_3$ thin film and the sapphire (Al_2O_3) substrate, a cross-sectional high-resolution TEM analysis (HRTEM) of a cycled CSD thin film was performed. A possible reaction zone between the substrate and the film would be parallel to the current direction. As shown in Figure 7.7, the interface is extremely sharp, clearly excluding any formation of amorphous or secondary phases.

Figure 7.7

Cross section TEM analysis of the interface between the sapphire substrate and the CSD-prepared $SrTiO_3$ thin film (STO5) after cycling [8].

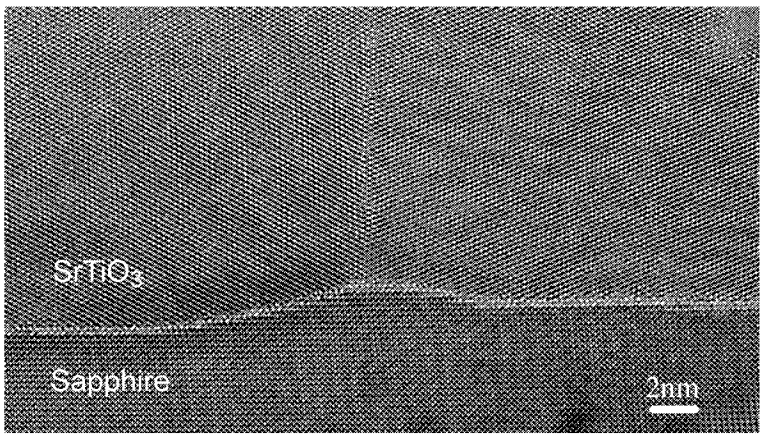

However, the micrograph reveals another interesting detail. It shows a triple phase boundary between two adjacent strontium titanate grains and the sapphire substrate. These substrates are received from the supplier with an 'epi-polished' surface quality, which usually exhibits an rms-roughness below 1 nm. A local roughness of 3 nm, as visible here, usually does not occur and has to be attributed to a thermally activated interface mass transport [4]. The reason for this morphological change in appearance is to be found in the reduction of the interface energy, which every system strives for. This picture is a nice example that the 90 ° - angle is not favored, but rather the system wants to build an angle of 120 °. This effect does not significantly influence the structure or morphology of the film at the interface, but it determines the temperature where the migration of surface atoms of the sapphire substrate is activated.

7.4 Conclusion

In conclusion, it can be stated that mass transport phenomena – either the unification of pores or segregation effects – are not relevant at temperatures below 900 °C. In addition, it has been shown that even after measurement cycles of up to 1000 °C no chemical reaction occurs at the interface between the film and the substrate.

References

[1] K. Szot and W. Speier, "Surfaces of reduced and oxidized $SrTiO_3$ from atomic force microscopy", *Phys. Rev. B* **60**, 5909 (1999).

[2] K. Szot, W. Speier, U. Breuer, R. Meyer, J. Szade and R. Waser, "Formation of micro-crystals on the (100) surface of $SrTiO_3$ at elevated temperatures", *Surface Science* **460**, 112 (2000).

[3] D. Hennings, Philips Forschungslaboratorien, Aachen, personal communication.

[4] Unpublished results. C.L. Jia, IFF (IMF), Research Centre Jülich, personal communication.

[5] Ch. Ohly, S. Hoffmann, K. Szot and R. Waser, "High Temperature Conductivity Behavior of Doped $SrTiO_3$ Thin Films", *Integr. Ferroelectr.* 33, 363 (2001).

[6] Ch. Ohly, S. Hoffmann, K. Szot and R. Waser, "Electrical conductivity and segregation effects of doped $SrTiO_3$ thin films", *J. Eur. Ceram. Soc.* **21**, 1673 (2001).

[7] Unpublished results. SNMS analysis by K. Szot.

[8] TEM analysis by C.L. Jia and Y. Ding, IFF (IMF), Research Centre Jülich, 2002.

8 Discussion

The distinctly different conductivity characteristics of nanocrystalline titanate thin films and ceramics presented in this work illuminate the extraordinary interplay between electrical properties and the morphology of the material when the scale is reduced to nanometer dimensions.

In this chapter, a comprehensive discussion of the measured conductivity characteristics of the different samples dependent on oxygen partial pressure is presented with respect to:

- the effects of increasing interface density, which assigns the grain boundary density and the surface-to-volume ratio;
- thermal activation energies of underlying conduction processes in the different pO_2 regimes;
- a detailed evaluation of all information on the conduction behavior in the plateau regime of nanocrystalline materials aiming to ascertain important characteristics of the major charge carriers in this region.

The discussion addresses the question of the extent to which the classical point defect chemistry model can still be applied and where there is a need for a different approach.

Figure 8.1

Different titanate morphologies studied in this work.

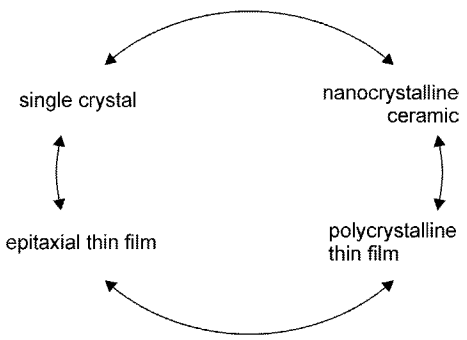

As illustrated again in Figure 8.1, a well-targeted variety of samples was examined to point out fundamental characteristics and to assign them to particular properties of the investigated samples. The discussion proceeds counterclockwise from a bulk single crystal through hetero-epitaxial thin films to polycrystalline thin films and finally comes to a nanocrystalline bulk ceramic to close the circle. This consideration includes all combinations of the important aspects of surface-to-volume ratio and grain boundary density.

As a starting point, a $SrTiO_3$ single crystal was analyzed to demonstrate the measurement technique's reliability and to gain a precise reference data set (Figure 6.2ff). The well-known characteristics are a decline in the conductivity σ with a slope of - ¼ in the $\log(\sigma)$ - $\log(pO_2)$ plot under reducing conditions (n-type regime) and the opposite + ¼ (p-type) behavior under oxidizing atmosphere. The n-type regime is thermally activated with an activation energy of $E_{A,red}$ = 2.78 eV, whereas the p-type region is activated by $E_{A,ox}$ = 0.51 eV (Eq. (6.8). The bandgap energy was calculated to be $E_G(0K)$ = 3.30 eV, Eq. (6.6), and the activation energy for oxygen vacancy diffusion could be determined to $E_{A,V\ddot{o}}$ = 0.99 eV (as given by Eq. (6.12)). All calculated values excellently fit those reported in the literature.

8.1 Heteroepitaxial Titanate Thin Films

Heteroepitaxial thin films grown by PLD are quite similar to bulk single crystals with respect to the structure, but the surface-to-volume ratio increases drastically by a factor of approximately 1000. As shown exemplarily in Figure 6.14, a 1 µm thick single crystalline $SrTiO_3$ film on MgO shows the same characteristic - ¼ and + ¼ slopes under reducing or oxidizing conditions, respectively, as obtained for the bulk single crystal. These regions can be clearly attributed to an n-type or correspondingly a p-type regime. The bandgap energy of 3.35 eV (Eq. (6.17)) is a very good fit to the values known for bulk materials.

Despite the similarities, a comparison of the absolute conductivity data of the thin film and the single crystal, Figure 6.15, also reveals decisive differences. As can be seen from the combined diagram, the conductivity curves of the film are shifted to higher oxygen partial pressures. This effect is the more pronounced, the lower the measurement temperature is. The behavior cannot be explained simply by a shift of the isoelectric point, as suggested in the literature [1]. Instead, the extent of shifting visibly depends on temperature. Also a pure doping effect cannot explain the observed behavior.

Looking more closely at the activation energies in the electronically dominated conductivity branches, determined from the Arrhenius-plot in Figure 6.16, some interesting details are revealed. While the values of the electronic conductivity minimum, for the determination of the bandgap energy, can be fitted very well to a straight line, the behavior in the n-type and p-type regimes has to be divided into two regimes. At higher temperatures (between 800 and 1000 °C), the thermal activation energies amount to $E_{A,red}$ = 2.17 eV and $E_{A,ox}$ = 1.06 eV. A break is observed for the lower temperature range from 700 – 800 °C, where the conductivity values in the n- and p-type region exhibit nearly the same activation energies $E_{A,red}$ = 1.62 eV and $E_{A,ox}$ = 1.55 eV.

In comparison to the single crystal data, the activation energies of the film decrease for the n-type and increase for the p-type regime. This trend is even more pronounced at lower temperatures around 700 °C. The discussed findings are consistent with results reviewed by Tragut [1]. He described a general trend of increasing oxidation energies when changing from single crystals to polycrystalline thick films and, at the same time, lowering the temperature. The most instructive example is probably reported for a thick film oxygen sensor, where the activation energy in the p-type region was determined to be $E_{A,ox}$ = 1.4 eV at 700 °C [2]. This agrees surprisingly well with the heteroepitaxial thin film under consideration here.

These results undoubtedly contradict to a description of the films – even the heteroepitaxial ones – as homogeneous and isotropic systems with respect to the charge transport.

More likely, an inhomogeneous system with concurring conduction processes has to be considered. In that case, the assumption of overall constant charge carrier mobilities is also questionable.

A detailed investigation of the surface effect on the conductivity curve goes beyond the scope of this work. Up to now, it is still difficult to trace surface defects of PLD-grown films and it is also not known whether they can be influenced or controlled by processing conditions.

8.2 Reduction of Grain Size

Although in principle the 1 µm thick heteroepitaxial $SrTiO_3$ film exhibited bulk-like behavior, some distinct deviations were also revealed. Differences to the bulk single crystal behavior

become more pronounced and also new characteristics appear when the grain size is reduced to the nanometer scale.

This trend is demonstrated by the conductivity behavior of a series of polycrystalline thin films shown in Figure 6.13. The films of comparable thickness were processed by PLD and are identified by different grain sizes (see Figures 4.9 and 4.13). Here, for a more or less constant surface-to-volume ratio, the grain boundary density increases significantly. Accompanying this morphological change, the trend of increasing absolute conductivity values in the n-type region and vice versa for the p-type regime is maintained.

With decreasing grain size, a drop in the conductivity curve and a small subsequent plateau region at mid-range oxygen partial pressures can be observed. The effects are most apparent for a columnar-grown, randomly oriented sample where the grain diameter is about 100 nm (#3667). The fact that a finer morphology (#3666 with a column diameter of only 50 nm) does not amplify the effects even more is attributed to the texture of the sample and the much more ordered character of the grain boundaries [3][4].

Due to the fact that the PLD-grown samples are of comparable thickness, the formation of the drop and the plateau region seems to be primarily an effect of the high density of grain boundaries.

These new characteristics in the $\log(\sigma)$ - $\log(pO_2)$ plot (drop of σ, plateau region) can also be illustrated by reducing the thickness of the heteroepitaxial thin films (Figure 6.17). The formation of a plateau appears here at a thickness of 250 nm (#3946). This dimension is comparable to the grain size of the coarse grained polycrystalline PLD film (#3668). Comparing the two, an approximate value of 250 nm can be taken as a critical feature size for the formation of the drop and the plateau regime of the conductivity profile.

8.3 Polycrystalline Thin Films

To further delve into the special conductivity characteristics found for films with feature sizes of less than 250 nm, the following discussion focuses on the CSD-derived, polycrystalline strontium titanate thin films. As described in Chapter 4, these films exhibit the smallest grain sizes (~ 50 nm) of all the samples encountered in this work. Not only is the grain boundary density

exceptionally high, also the intergranular porosity adds further interfaces (see Figures 4.4 and 4.5). Proceeding from the picture drawn before, the conduction profiles of these films most drastically differ from that of the single crystal.

The behavior of a nominally undoped, 500 nm thick polycrystalline $SrTiO_3$ thin film (Figure 6.6) lucidly illustrates the dramatic changes that are caused by the introduction of a large amount of grain boundaries to the matrix. Under reducing ambients, the absolute conductivity values are now about two orders of magnitude above that of the single crystal. Under oxidizing atmospheres a p-type increase of the conductivity can no longer be observed anymore. These two observations can be summarized in a view that the total curve is shifted far to higher oxygen partial pressures in comparison to the single crystal. The sharp drop of σ appears at oxygen partial pressures between 10^{-15} and 10^{-10} bar, depending on temperature, and the subsequent broad plateau region extends up to 10^{-5} bar. Under oxidizing atmospheres, the conductivity decreases further instead of the expected p-type increase found for bulk materials.

This special behavior was found for a variety of films which show similar morphologies, including acceptor- (Mn) and donor-doped (La) thin films, as well as selected members of the solid solution series $Ba_{1-x}Sr_xTiO_3$ (Figures 6.8 – 6.11).

Returning to the discussion of activation energies, the CSD prepared thin films exhibit the lowest values compared to the heteroepitaxial films and the single crystal, respectively. The activation energy of the undoped $SrTiO_3$ thin film (STO5) in the n-type region $E_{A,red}$ again shows two different values according to different temperature regimes. At temperatures above 800 °C, $E_{A,red}$ amounts to 1.66 eV, whereas towards lower temperatures, the activation energy is reduced to $E_{A,red}$ = 1.19 eV.

From this and the results of Chapter 8.2 it can be concluded that an increase of the interface density (i.e. the surface-to-volume ratio as well as the grain boundary density) distinctly affects the oxygen exchange reaction and reduces the reduction energy $E_{A,red}$.

8.4 Nanocrystalline Titanates

Especially enlightening is the conductivity profile of the nanocrystalline $BaTiO_3$ ceramic depicted in Figure 6.18. This sample exhibits a mean grain size of ~ 100 nm and shows almost the same

conduction behavior as the polycrystalline thin films. In contrast to thin films, this is a bulk ceramic sample, which is not clamped to a substrate and which exhibits the same surface-to-volume ratio as the single crystal. Therefore, the special conductivity characteristics can be clearly identified as an effect caused by an extremely high grain boundary density and not by a special thin film property.

Due to the surprising similarity of the two different nanocrystalline systems, additional investigations, which have not been possible for thin films, were performed on the nanocrystalline $BaTiO_3$ ceramic in order to further illuminate the different conductivity regimes.

Assigning the conductivity characteristics of the nanocrystalline $BaTiO_3$ sample to the thermopower profile (Figure 6.19), the assumption that electrons to be the dominating charge carrier type in the n-type region is definitely confirmed. The slope of η clearly resembles the pO_2 dependence of the electron density n ($\eta \sim -\ln(1/n)$ with $n \sim (pO_2)^{-1/4}$, see Eq. (3.31)). The change of the sign of η towards highly oxidizing atmospheres associates the increasing conductivity in this regime to p-type charge carriers dominated by electron holes.

The calculation of the activation energy in the n-type region, which amounts to $E_{\Lambda,red} = 2.47$ eV, is very instructive. Although the general behavior of the conductivity profile resembles that of the polycrystalline thin films, $E_{\Lambda,red}$ is in contrast qualitatively of the same value as for the single crystal. We thus obtain a very interesting correlation of the different reduction energies to the sample morphology:

Table 8.2

Activation energy $E_{\Lambda,red}$ for the different morphologies studied in this work.

$SrTiO_3$ single crystal	**nanocrystalline $BaTiO_3$ ceramic**
2.78 eV (700 – 1000 °C)	2.47 eV (700 – 800 °C)
epitaxial $SrTiO_3$ thin film (#3461)	**polycrystalline $SrTiO_3$ thin film** (STO5)
2.17 eV (800 – 1000 °C) 1.62 eV (700 – 800 °C)	1.66 eV (800 – 1000 °C) 1.19 eV (700 – 800 °C)

Table 8.2 shows the fundamental classification of the different samples (i.e. morphologies). The first stems from the bulk samples with $E_{\Lambda,red}$ values of ~ 2.5 eV and above, whereas the second subsumes the thin film samples exhibiting values of $E_{A,red}$ of 2 eV and below. This leads to the assumption that the decrease of the activation energy $E_{A,red}$ is predominantly due to an increasing surface-to-volume ratio as obtained for thin films.

8.5 Critical Aspects

Let us now draw attention to the characteristic radical drop of σ coming from the n-type region and focus on the following plateau regime.

It was already proved in Chapter 6 that the conductivity plateau of the nanocrystalline systems cannot be assigned to a classical donor plateau by reason of its Arrhenius-type thermal activation. Also, the idea of a quenched state [12] must be abandoned, despite the apparent similarity of the conductivity profiles. The curves here represent equilibrium measurements without previous quenching and without leaving the isotherm.

The fact that the conductivity is independent of the oxygen partial pressure in the plateau, in combination with the thermal activation, points to the hypothesis of an ionic conduction mechanism. From the classical defect chemical point of view, the concentration of electronic charge carriers is always markedly affected by the pO_2, whereas the concentration of ionic charge carriers is not (as long as the extrinsic generation of oxygen vacancies under reducing conditions is not considered), and the ionic diffusion coefficient generally follows an exponential temperature dependence.

Among the ionic defects in titanates, oxygen vacancies exhibit the highest mobility and dominate the conduction behavior of p-type acceptor-doped titanates at lower temperatures. But here a direct identification of oxygen vacancies as the dominant charge carriers fails because of the high activation energies. For polycrystalline $SrTiO_3$ thin films and the nanocrystalline $BaTiO_3$ ceramic, the activation energies $E_{A,pl}$ are roughly between 2 and 2.5 eV (Eqns. (6.13) - (6.17)). In single crystals, an activation energy for oxygen vacancy diffusion of about 1 eV is found, which is considerably less (Eq. (6.12)). Therefore it is questionable whether oxygen vacancies are really the dominant charge carrier species here. A clear contradiction is revealed by the thermopower characteristics of the nanocrystalline $BaTiO_3$ sample (Figure 6.19). As indicated in the plot, the thermopower in the plateau region is indeed constant (proving a constant charge carrier concentration), but negative. As long as the qualitative picture of thermopower can be applied to diffusing ions, it has to be a negatively charged species. This excludes oxygen vacancies, which are positive.

The diffusion of strontium or barium vacancies and titanium vacancies normally does not contribute perceptibly to the total conductivity because of very low diffusion constants. For comparison, the following activation energies for cation diffusion can be found in the literature ([5]-[11], Eq. (6.12)):

$$E_{A,V_O^{\cdot\cdot}} \approx 1\,\text{eV} \tag{8.1}$$

$$E_{A,V_{Sr}''} \approx 2.8\,\text{eV} \tag{8.2}$$

$$E_{A,V_{Ba}''} \approx 2.76\,\text{eV} \tag{8.3}$$

$$E_{A,V_{Ti}''''} \approx 2.47 \ldots 3.1\,\text{eV} \tag{8.4}$$

Cation vacancies exhibit diffusion constants at least 3 orders of magnitude lower than those of oxygen vacancies.

From the sign of the thermopower signal and the activation energy, the conduction in the plateau region would surprisingly have to be attributed to cation vacancy diffusion, presumably of the A-site cation.

But the assumption of cation vacancies as dominant charge carriers in the plateau region raises some questions:

- In the case of undoped and acceptor-doped titanates, the formation of cation vacancies should be strongly suppressed due to the presence of ionized acceptors and compensating oxygen vacancies. What is therefore the origin of the cation vacancies in these samples?

- Looking at the behavior of donor doped samples, the further decline of σ at high oxygen partial pressures is puzzling. If the total conductivity is the sum of a pO_2-independent ionic contribution and an electronic part, the σ_{ionic} should resemble a minimum residual conductivity. How can the total conductivity fall beneath that level?

The 2 at.% lanthanum doped sample (ST_HTL04) has a further discrepancy to the classical point defect chemical understanding, as illustrated in Figure 8.3. This diagram also illustrates the conductivity profiles of a highly porous, 5 at.% La-doped $SrTiO_3$ ceramic with a mean grain size of about 500 nm. The similarity of the profiles is amazing, thus again underlining the similarity between polycrystalline thin films and nanocrystalline ceramics.

Under oxidizing atmospheres, the slope of the conductivity curve fits very well to the behavior of the n-type region for both samples. Under reducing conditions, the ceramic sample exhibits a slope in conductivity of nearly - $^1/_6$, indicating an extrinsic regime, while the thin film shows a slope of - $^1/_8$. Astoundingly, the extrapolation of the - $^1/_6$ and - $^1/_4$ branches to the mid - pO_2 region does not yield any indication of the existence of a classical donor plateau. Instead, the extrapolated lines intersect without any gap in between.

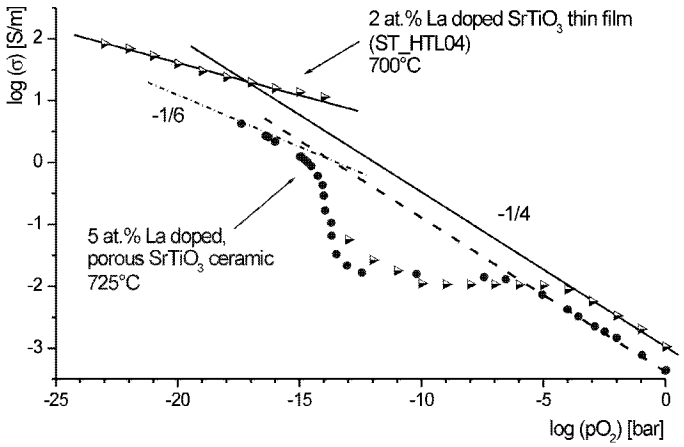

Figure 8.3

Conductivity profiles of donor-doped strontium titanate. The data for the porous ceramic sample are courtesy of W. Menesklou [13].

Because the dominant charge carrier species cannot be identified clearly, also the origin of the conductivity drop itself remains unclear.

The sudden drop implies a trapping of the electrons. The thermal activation of the height (i.e. the plateau level) and its position with respect to the oxygen partial pressure support this assumption. Because of the undoubted relationship to interfaces, especially grain boundaries, the interfacial states will have to be in the focus of future investigations.

8.6 New Directions

As a quintessence of this discussion, the classical view of point defect chemistry does not provide sufficient background for a satisfactory description of the individual conductivity characteristics. As pointed out, the possible explanations for a shift of the conductivity profiles are inconsistent (e.g. due to a change of the isoelectric point). Furthermore, an attribution of the drop to known effects fails completely.

The results unambiguously indicate that a nanocrystalline material is a strongly inhomogeneous system. Due to the immense impact of the surface and even more of the grain boundaries, a future defect chemical description has to be developed that differentiates the individual regions, i.e.

- the bulk:
  Here the question arises of the extent to which the classical description can be applied in the case where the space charge layers overlap. As mentioned in Chapter 3, the width of these layers ranges between 30 and 200 nm, which is of the same order of magnitude as the feature size.

- the grain boundary:
  In recent work on CeO_2 (what exhibits a comparable defect chemistry with respect to the oxygen ambient), Chiang proposed a lower enthalpy for oxygen vacancy formation at the grain boundary [14]. This leads to an increased electronic conduction and the nanocrystalline material becomes "in effect doped by its own interfaces" [14].

  Because of its fundamental influence on the conductivity profiles, which has emerged from this work, a charge transport mechanism along the grain boundary, competing to the movement through the bulk, has to be considered.

- the surface:
  although of secondary importance as revealed by this work, the question is still unanswered as to whether the conduction experiences an alteration in the surface region of titanates.

Therefore, the conventional, homogeneous expression for the conductivity,

$$\sigma = \sum_i q_i \cdot \mu_i \cdot [i], \tag{8.5}$$

can no longer be maintained.

A future model description has to deal with preferred current paths, spatially inhomogeneous charge carrier concentrations, as well as variable mobilities of the individual species.

The transport mechanisms may also show very peculiar dependences on the oxygen partial pressure and it can be expected that competing mechanisms will dominate in certain regions of oxygen partial pressure.

References

[1] Ch. Tragut, "Kinetik schneller Sauerstoffsensoren", PhD thesis, Universität Karlsruhe, Fortschrittberichte VDI, Reihe 8, Nr. 291, Düsseldorf, 1992.

[2] U. Schönauer, "Strontiumtitanat-Sauerstoffsensoren in Dickschichttechnologie", PhD thesis, Universität Karlsruhe, Fortschrittberichte VDI, Reihe 8, Nr. 227, Düsseldorf, 1990.

[3] C.L. Jia, IFF (IMF), Research Centre Jülich, personal communication.

[4] S.R. Gilbert, L.A. Wills, B.W. Wessels, J.L. Schindler, J.A. Thomas and C.R. Kannewurf, "Electrical transport properties of epitaxial $BaTiO_3$ thin films", *J. Appl. Phys.* **80**, 969 (1996).

[5] I. Denk, W. Münch and J. Maier, "Partial Conductivities in $SrTiO_3$: Bulk Polarization Experiments, Oxygen Concentration Cell Measurements, and Defect-Chemical Modeling", *J. Am. Ceram. Soc.* **78**, 3265 (1995).

[6] A.E. Paladino, "Oxidation Kinetics of Single-Crystal $SrTiO_3$", *J. Am. Ceram. Soc.* **48**, 476 (1965).

[7] R. Wernicke, "Defect Chemistry and Electrical Conductivity of Doped Barium Titanate Ceramics: Part IV: The Kinetics of Equilibrium Restoration in Barium Titanate", *Philips Res. Reports* **31**, 526 (1976).

[8] J. Nowotny and M. Rekas, "Defect Structure, Electrical Properties and Transport in Barium Titanate. VII. Chemical Diffusion in Nb-Doped $BaTiO_3$", *Ceramics Intern.* **20**, 265 (1994).

[9] W. Menesklou, "Kompensationsmechanismen der Überschußladung in lanthandotiertem Strontiumtitanat", PhD thesis, Universität Karlsruhe, Fortschrittberichte VDI, Reihe 5, Nr. 481, Düsseldorf, 1997.

[10] F. Poignant, "L'oxydation de céramique à base de titanate de strontium semi-conducteur et la formation de barrière de potentiel aux joints de grains", PhD thesis, Université Limoges, 1995.

[11] R. Meyer, "Modellierung transienter Vorgänge in donatordotiertem Strontiumtitanat", PhD thesis, RWTH Aachen, Fortschrittberichte VDI, Reihe 21, Nr. 328, Düsseldorf, 2002.

[12] R. Waser, "Bulk Conductivity and Defect Chemistry of Acceptor-Doped Strontium Titanate in the Quenched State", *J. Am. Ceram. Soc.* **74**, 1934 (1991).

[13] W. Menesklou, personal communication. This curve was presented at the MRS Fall Meeting, Boston, 2000. Courtesy W. Menesklou, Karlsruhe University.

[14] Y.-M. Chiang, E.B. Lavik, I. Kosacki, H.L. Tuller and J.Y. Ying, "Nonstoichiometry and Electrical Conductivity of Nanocrystalline CeO_{2-x}", *J. Electroceramics* **1**, 7 (1997).

9 Conclusions

9.1 Summary

A typical characteristic of electroceramic thin films, which have been investigated intensively for future integrated devices, is their nanocrystalline structure. Although a comprehensive understanding of the correlation between the morphology and charge carrier transport mechanisms in these systems is inevitable, the defect chemical behavior of nanocrystalline titanates is still an open field.

This work aims at the systematic und detailed investigation of the defect chemistry of titanate thin films by means of high-temperature conductivity measurements under changing oxygen atmospheres. The investigations primarily address thin films based on $SrTiO_3$, which is often used as a model perovskite system and which permits a thorough comparison to the bulk characteristics.

For the first time, this work gives a detailed picture of the conductivity behavior of nanocrystalline titanates under changing oxygen partial pressures.

The results are summarized as follows:

1. In order to investigate the conductivity behavior of thin film titanates as a function of temperature and oxygen partial pressure (pO_2), a specially designed measurement setup was built. It comprises an oxygen pump on the basis of the solid state electrolyte YSZ (stabilized zirconia), which permits reliable control of the ambient pO_2 continuously between reducing atmospheres of at least 10^{-20} bar and pure oxygen atmospheres (1 bar) at temperatures ranging from 600 °C to 1000 °C. The 4-point dc measurement technique, in combination with electrometric metering and a triaxial shielded sample holder, provided the prerequisite for a reliable determination of the conductivity of highly resistive thin films.

A measurement on a $SrTiO_3$ single crystal, in excellent agreement with the literature, yielded an indispensable and very precise reference for comparison with the following investigations on titanate thin films.

2. In order to achieve a comprehensive picture, a well-targeted variety of samples was prepared covering a wide range of morphological properties. Thin films grown by chemical solution deposition show a polycrystalline structure and generally exhibit a columnar morphology with a mean grain diameter of ~ 50 nm. This route was also chosen for doping incorporation (Mn and La) and to synthesize samples of the solid solution series $Ba_{1-x}Sr_xTiO_3$ and $BaTi_{1-y}Zr_yO_3$. Using the pulsed laser deposition method, heteroepitaxial $SrTiO_3$ thin films of varying thickness were grown (250 nm to 3 μm). This technique was also applied for the preparation of polycrystalline films with different grain sizes (~ 50 nm to 300 nm). In addition, nanocrystalline $BaTiO_3$ ceramics were prepared by pressure-assisted sintering (hot forging and hot isostatic pressing) of microemulsion-derived nanopowders. The grain sizes of such samples were between 35 and 100 nm.

3. The conductivity behavior of an undoped, polycrystalline CSD-derived $SrTiO_3$ thin film exhibits drastic changes of the well-known characteristics of the single crystal as well as completely new features of the conductivity profile. Under reducing conditions, a declining conductivity with increasing pO_2 is found, but with much higher absolute values. At mid-range oxygen partial pressures (depending on temperature between 10^{-15} and 10^{-10} bar), a drop in the conductivity suddenly occurs, which is followed by a broad plateau region. Under oxidizing conditions, the conductivity tends to decrease further.
This characteristic conductivity profile demonstrates the immense influence of the morphology of the film. The new characteristics, especially the drop and the plateau region, cannot be adequately explained by classical defect chemistry.

4. The incorporation of dopants leads to a shift of the conductivity curve, but generally retains the characteristics of the undoped $SrTiO_3$ thin film. The addition of La as a donor resulted in higher conductivity values whereas Mn as an acceptor reduces them.
The special conductivity behavior is also found for $Ba_{1-x}Sr_xTiO_3$ and $BaTi_{1-y}Zr_yO_3$ thin films. The replacement of strontium by the isovalent barium shifts the drop towards higher partial pressures. The replacement of titanium by zirconium revealed that for increasing Zr concentrations the conductivity in the n-type region decreases significantly. This can be attributed to the valence stability of Zr with respect to reduction.

5. Studies of the conductivity behavior of heteroepitaxial $SrTiO_3$ thin films confirmed the importance of the grain boundary density. In general, single crystalline films resemble the bulk characteristics. A reduction of the thickness elucidates the trend of increasing conductivity values in the n-type region and decreasing values in the p-type regime. The formation of the drop and the accompanying plateau region appears if the thickness is reduced to 250 nm.

6. The successive transition from single crystalline to polycrystalline thin films by introducing of grain boundaries also raises the absolute conductivity values at low pO_2 and results in lower conductivity at high pO_2. Again, the formation of the drop can be seen at a mean grain size of 200 – 300 nm, so that this dimension (or feature size) can be considered as a critical value where the nanocrystallinity controls the behavior of the sample.

7. The conductivity profile of a specially prepared nanocrystalline $BaTiO_3$ ceramic exhibits the same behavior as the undoped $SrTiO_3$ thin film. This is a direct proof that the characteristic drop and the plateau region directly correlate to the increasing grain boundary density.
For this sample, it was possible to determine the thermopower as a function of the oxygen partial pressure. It confirmed electrons as the dominant charge carriers in the n-type region and electron holes in the p-type regime, respectively. It also revealed a negative sign of the charge carrier species in the plateau region.

8. For the pO_2 - independent conductivity in the plateau region of nanocrystalline titanates a thermal activation energy of about 2 to 2.5 eV was determined. Together with the negative sign of η, this brings up the idea that the dominant charge carriers in this region might be cation vacancies. This idea is not consistent with the classical picture for bulk titanates.

9. A comparison of the activation energies leads to the conclusion that an increasing surface-to-volume ratio decreases the reduction energy $E_{A,red}$ in the n-type region of the conductivity curve and vice versa increases the activation energy $E_{A,ox}$ under oxidizing atmospheres. Additionally, $E_{A,red}$ exhibits two temperature regimes with different values. This temperature dependence clearly indicates competing conduction mechanisms. The attribution to a surface effect is confirmed by a comparison with the data of the nanocrystalline bulk ceramic, where $E_{A,red}$ comes close to the bulk value.

10. For the first time, the measurements show that nanocrystalline titanates with an extremely high grain boundary density exhibit exceptional conductivity characteristics that cannot be sufficiently explained on the basis of classical point defect chemistry. The results

unquestionably demonstrate the strongly heterogeneous nature of nano-sized materials. A model description has to account for this heterogeneity. The conventional postulate of spatially constant charge carrier concentrations and mobilities has to be reformulated. Furthermore, the results indicate a drastically different defect chemistry of the grain boundary compared to the bulk. This becomes dominant when the entire grain is dominated by the influence of the grain boundary.

11. Investigations on the morphological habit after extended measuring cycles at up to 1000 °C revealed the unification of inherent pores. The onset temperature of this mechanism is at about 900 °C. Surface restructuring effects become important only after prolonged annealing under extreme atmospheric conditions, either reducing or oxidizing, at 1000 °C. In addition, it was revealed that no interface reaction between the thin film and the substrate takes place during extended measurement cycles.

9.2 Outlook

In order to find a quantitative defect chemical description and account for the heterogeneous nature of nanocrystalline titanates, the behavior and contributions of the individual charge carriers with respect to their interrelationship to grain size and oxygen partial pressure have to be elucidated. This comprises mainly the identification of the individual charge carrier species, their concentration and mobility.

To accomplish this further studies by Hall measurements and the accompanying determination of thermopower are needed. Additionally, impedance spectroscopy may help to separate the contributions to the conductivity by grain boundaries and the bulk. Furthermore, the grain boundary in a nanocrystalline thin film has to be examined with respect to its morphological and structural habit as well as stoichiometric composition by means of analytical HRTEM with a high lateral resolution to precisely illuminate the defect chemical situation at the interface. Possible ionic diffusion processes have to be addressed by tracer diffusion experiments assisted by SIMS.

To get a clear picture, future studies require more precisely prepared samples. Especially if the microemulsion technique and carefully chosen processing parameters are used nanocrystalline ceramics offer the possibility of precisely tailoring the grain size down to a few tens of nanometers. This may provide a substitute for substrate-based thin films and help to obtain higher readings.

Acknowledgements

First of all, I would like to thank Prof. Dr. Rainer Waser, head of IFF-EKM at Research Centre Jülich and IWE II at Aachen University, for giving me the opportunity to work in the exciting field of electroceramics and to benefit from the resources of two research institutions.

I would like to thank Prof. Dr. Manfred Martin (IPC I/Aachen University), who kindly agreed to be the co-examiner, for his interest in my work.

I am very happy to have met Dr. Susanne Hoffmann-Eifert, who accompanied me as my tutor throughout the years. I would like to express my sincere gratitude for both her excellent scientific guidance as well as her personal encouragement.

I greatly appreciate the many discussions with Dr. Wolfgang Menesklou (IWE/Karlsruhe University) and his valuable advice concerning the oxygen pump.

To Dr. Krzysztof Szot I am indebted for his thorough surface analytical investigations and for sharing his experimental know-how with me.

Many thanks to Dr. Jürgen Schubert (ISG 1) for providing all the PLD-grown thin films.

I gratefully acknowledge the cooperation with Dr. Christian Pithan, Dr. Jürgen Dornseiffer (ICG-II), Dr. Franz-Hubert Haegel (ICG-V) and Berthold Coenen (IWV-1) for the preparation of nanocrystalline barium titanate ceramics.

Special thanks are due to Maria García, who was very kind and helpful with everything.

Daliborka Vukelić, Gisela Wasse and Rainer Gerhardt (all IWE II/Aachen University), Marcel Gerst as well as the colleagues from the mechanical and glass workshops in Jülich were always very helpful regarding technical support.

Thanks to Janet Carter-Sigglow for carefully checking the language of the manuscript.

I would also like to thank all colleagues from the group in Jülich and in Aachen for a pleasant working atmosphere.

Finally, sincere thanks to my parents, to whom I dedicate this thesis, for their support at all times.

Forschungszentrum Jülich
in der Helmholtz-Gemeinschaft

Jül-4070
Juli 2003
ISSN 0944-2952